POLITECNICO
MILANO 1863

SCUOLA DI INGEGNERIA INDUSTRIALE
E DELL'INFORMAZIONE

Statistical analysis of blisters in electrochemically intercalated HOPG by innovative combined AFM-Raman investigation

TESI DI LAUREA MAGISTRALE IN
ENGINEERING PHYSICS - INGEGNERIA FISICA

Author: **Elia Mazzoletti**

Student ID: 997209
Advisor: Prof. Valeria Russo
Co-advisors: Prof. Gianlorenzo Bussetti
Academic Year: 2023/2024

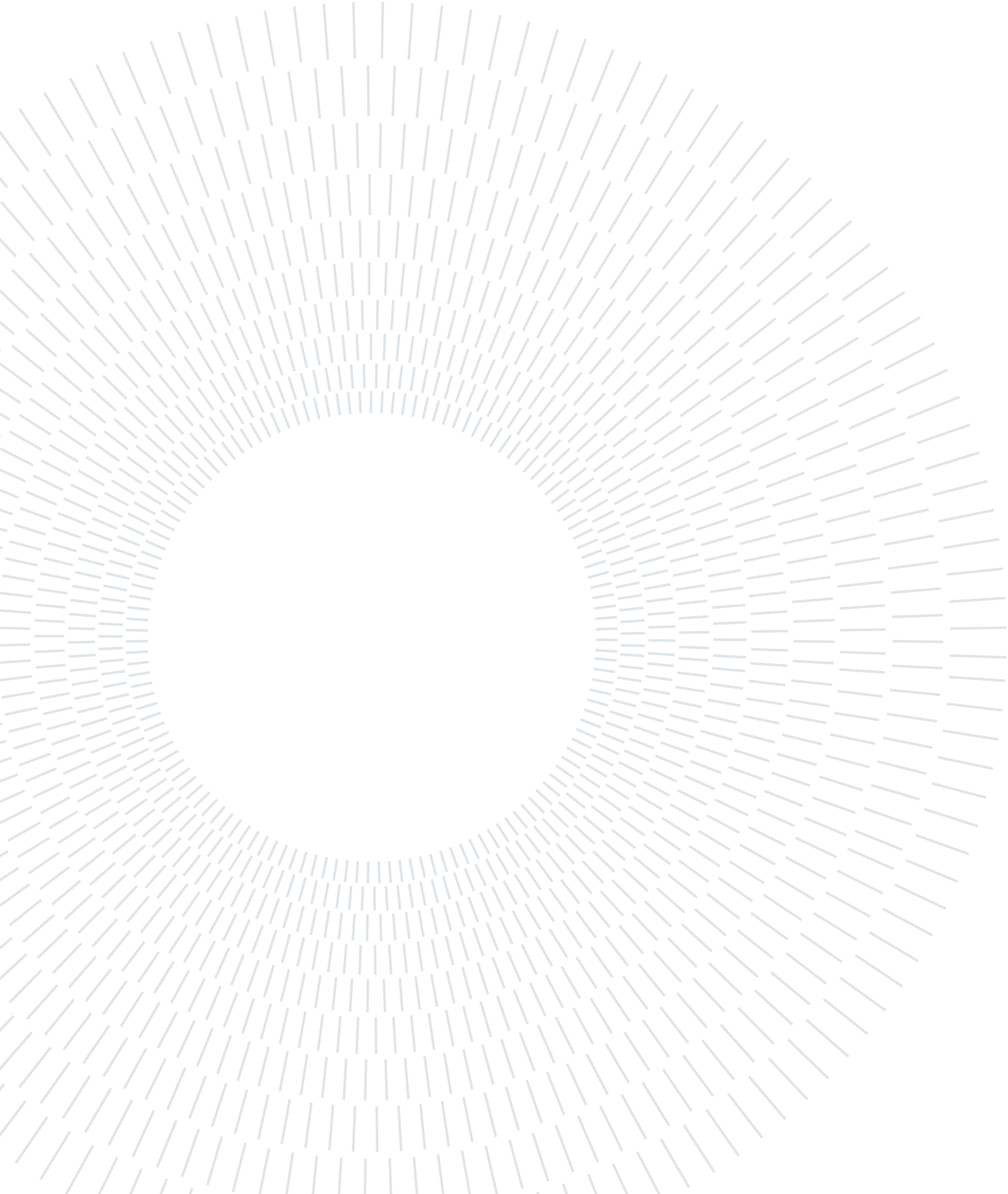

Abstract

Graphite is one of the most employed materials in modern technology. Its mechanical, thermal and electronic properties, combined with its chemical stability in different environments, offer possibilities of application in many fields, such as refractory materials, moderator in nuclear reactors and electrode in chemical applications: for example as anode in Li-ion batteries. Graphite structure consists in monoatomic planes of carbon atoms stacked on top of each other. The in-plane bonds are very strong, while the interplanar interactions are weak Van der Walls bonds. Graphite is therefore a highly anisotropic material. Its most employed and studied commercial form is Highly Oriented Pyrolitic Graphite (HOPG), which, thanks to its production methods, presents high purity and oriented crystal grains. Even though policrystalline, HOPG is therefore a macroscopically laminar material. Its ordered crystal structure leads to enhanced electronic and mechanical properties, which also present high anisotropy because of the difference of the carbon bonds strength in the in-plane and off-plane directions. HOPG is an inexpensive and practical sample for surface experimental studies such as scanning probe microscopy techniques like Atomic Force Microscopy (AFM), and spectroscopic techniques, in particular Raman spectroscopy. Thanks again to their laminar structure, HOPG samples can be re-used many times after surface treatments, because a new freshly prepared and pristine surface can be easily produced through simple mechanical exfoliation of the samples. Graphite is the first discovered and most studied laminar crystal, making it a case study for other similarly structured natural and artificial crystals. Finally, HOPG is the starting material for top-down production of graphene, a material made of monoatomic carbon sheets, which can be obtained through mechanical or in-liquid chemical exfoliation of HOPG.

HOPG intercalation is a fundamental electrochemical (EC) process that consist in ion insertion between the graphite planes. This process is essential in the production of batteries, since by this mechanism a good density of ions can be introduced in the graphite electrode. Intercalation processes may also facilitate the production of high quality graphene sheets by chemical exfoliation, since the ion insertion results in reduced interplanar interactions, and thus helps the detachment of the sheets. Studies on intercalated HOPG have tried to highlight the mechanisms and features of this complex process, which are nowdays still under debate. One of the most interesting consequences of intercalation with some ions species, like sulfuric acid, is the formation of micrometric swelled structures on the HOPG surface called blisters. These swellings seem to be caused by the formation of gasses inside HOPG during the EC process, which remain trapped under a "skin" comprised by graphite sheets of few atomic planes. Because of the internal gas pressure, the skin is elastically strained and the blister appears at the AFM view as a "bubble" over the atomically planar HOPG surface, which is referred to as basal plane. Blisters structure, stratigraphy, and formation mechanisms are however still not completely clear.

In this work I conducted a combined Atomic Force Microscopy (AFM) and local Raman spectroscopy statistical analysis on blisters of HOPG, electrochemically intercalated with a 1M sulfuric acid (H_2SO_4) solution. This analysis was possible thanks to an innovative experimental setup, which allows to combine the two techniques by the precise alignment of the AFM tip and the Raman laser beam. The system is capable of local Raman spectra acquisition with spatial resolution in the order of the Rayleigh limit ($< 1\mu m$). All the measurements were conducted in air since blisters are stable structures. The experimental system, in perspective, permits also in-situ and in-operando analysis. This study revealed a complex interplay of different phenomena that contribute to blisters morphological and spectral features. The strain of the inflated graphite skin, which can be estimated from the AFM images, modifies the C-C bond length and results in a change of position of the graphite Raman peaks on blisters. The intensity and lineshape of the Raman peaks seems also influenced by many other phenomena, for example: intercalation, swelling effects, and the contribution of the underlying HOPG basal plane under the blister skin. A detailed analysis was conducted to understand and decouple this effects. This thesis work highlights the potential of the combined analysis in the study of nanostructured surface systems, as well as it current limitations. The combined AFM Raman technique is a versatile setup that can be used for many applications in surface physics. This work should be considered as an important case study, exemplar for further developments of this original experimental technique.

Keywords: HOPG; intercalation; blisters; AFM-Raman correlation.

Abstract in lingua italiana

La grafite è uno dei materiali più utilizzati nella tecnologia moderna. Le sue proprietà meccaniche, termiche ed elettroniche, combinate con la sua stabilità chimica in diversi ambienti, offrono possibilità di applicazione in molti campi: come materiale refrattario, moderatore nei reattori nucleari ed elettrodo in applicazioni chimiche, ad esempio come anodo nelle batterie agli ioni di litio. La struttura della grafite è costituita da piani monoatomici di carbonio impilati. I legami nel piano sono molto forti, mentre le interazioni interplanari sono deboli legami di Van der Walls; la grafite è quindi un materiale molto anisotropo. La sua forma commerciale più utilizzata e studiata è la Grafite Pirolitica Altamente Orientata (HOPG), che grazie ai suoi metodi di produzione presenta elevata purezza e grani cristallini orientati. Nonostante sia policristallina, l'HOPG è quindi un materiale macroscopicamente laminare. La struttura ordinata della HOPG si traduce in migliori proprietà elettroniche e meccaniche, che presentano anch'esse un'elevata anisotropia a causa della differenza di forza dei legami carbonio nella direzione parallela e perpendicolare ai piani atomici. L'HOPG è un campione economico e pratico per studi sperimentali di superficie come tecniche di microscopia a scansione di sonda, ad esempio microscopia a forza atomica (AFM), e tecniche spettroscopiche, in particolare la spettroscopia Raman. Sempre grazie alla loro struttura laminare, i campioni di HOPG possono essere riutilizzati molte volte dopo i trattamenti superficiali, poichè una nuova superficie incontaminata può essere facilmente prodotta attraverso la semplice esfoliazione meccanica dei campioni. La grafite è il primo cristallo laminare scoperto ed il più studiato, e questo la rende un caso studio per altri cristalli naturali e/o artificiali con struttura simile. L'HOPG è infine anche il materiale di partenza per la produzione top-down di grafene, un materiale che consiste in strati monoatomici di carbonio ed è ottenuto mediante l'esfoliazione meccanica o chimica in liquido della HOPG.

L'intercalazione della HOPG è un importante processo elettrochimico (EC), che consiste nell'inserimento di ioni tra i piani della grafite. Questo processo è essenziale nella produzione di batterie, poiché attraverso l'intercalazione si può introdurre una buona concentrazione di ioni nell'elettrodo di grafite. I processi di intercalazione potrebbero anche facilitare la produzione di fogli di grafene di alta qualità mediante esfoliazione chimica, poiché l'inserimento di ioni determina una riduzione delle interazioni interplanari, semplificando il distacco dei fogli. Diversi studi sulla HOPG intercalata hanno cercato di descrivere i meccanismi le caratteristiche di questo complesso processo, aspetti ancora oggi oggetto di discussione. Una delle conseguenze più interessanti dell'intercalazione con alcune specie chimiche, come l'acido solforico, è la formazione di strutture rigonfie di dimensioni micrometriche sulla superficie dell'HOPG, chiamate blisters. Questi rigonfiamenti sembrano essere causati dalla formazione di specie chimiche gassose all'interno dell'HOPG durante il processo elettrochimico, che rimangono intrappolate sotto una "pelle"costituita da fogli di grafite dello spessore di pochi piani atomici. A causa della pressione interna dei gas, la pelle è tesa ed il blister appare all'AFM come una "bolla" sulla superficie della HOPG, che è atomicamente planare e viene chiamata piano basale. La struttura, la stratigrafia ed i meccanismi di formazione dei blister non sono tuttavia ancora del tutto chiari.

In questa tesi ho condotto un'analisi statistica combinata di microscopia a forza atomica (AFM) e spettroscopia Raman locale sui blister della HOPG, intercalata elettrochimicamente con una soluzione 1M di acido solforico (H_2SO_4). Questa analisi è stata possibile grazie ad un innovativo apparato sperimentale, che consente di combinare le due tecniche tramite il preciso allineamento della punta AFM con il laser Raman. Il sistema è in grado di acquisire spettri Raman locali, con risoluzione spaziale nell'ordine del limite di diffrazione ($< 1\mu m$). Tutte le misure sono state condotte in aria, poiché i blister sono strutture stabili. Il sistema sperimentale consente, in prospettiva, anche analisi in-situ e in-operando. Questo studio ha rivelato la presenza di una complessa sovrapposizione di fenomeni, che contribuiscono alle caratteristiche morfologiche e spettrali dei blister. La deformazione elastica della pelle dei blister, che può essere quantificata dalle immagini AFM, modifica la lunghezza dei legami C-C e si traduce in una variazione della posizione dei picchi Raman della grafite. L'intensità e la forma di linea dei picchi sembrano influenzati anche da altri fenomeni, ad esempio: l'intercalazione, gli effetti del rigonfiamento, ed il contributo del piano basale della HOPG sotto la pelle del blister. Un'analisi dettagliata dei risultati è stata condotta per comprendere e disaccoppiare questi effetti. Questo lavoro di tesi evidenzia il potenziale dell'analisi combinata nello studio di sistemi superficiali nanostrutturati, nonché i suoi attuali limiti. La tecnica combinata AFM-Raman è una configurazione versatile, che può essere utilizzata per molte applicazioni nella fisica delle superfici. Questo lavoro deve essere considerato come un importante caso studio, di esempio per ulteriori sviluppi di questa originale tecnica sperimentale.

Parole chiave: HOPG; intercalazione, blister, correlazione AFM-Raman.

Contents

1 | Introduction

Graphite is one of the most employed materials in modern technology: its mechanical, thermal, and electronic properties combined with its chemical stability in many environments offer the possibility of applications in variety of fields, such as refractory materials, moderator in nuclear reactors, carbon brusher in electrical motors etc. In particular, good electrical and thermal conductivity, corrosion resistance, low thermal expansion, low elasticity and high purity make it an ideal material as electrode for electrochemical applications such as in Li-ion batteries [1, 2]. Graphite is the first discovered and most studied laminar crystal, making it a case study for other stratified materials, like MoS_2 for example.

Since the Nobel Prize in physics to A. Geim and K. Novoselov (2010) [3], graphite has also focused additional interest as the starting material from the top-down production of graphene. In view of industrial implementation, a quantity and quality enhancement of obtainable graphene is needed, togheter with a reduction of the production costs. One possible strategy to facilitate graphene production is ion intercalation, a process which consists in the interposition of ions inside the stratified structure of graphite. Intercalation results in an expansion of the graphitic structure of a factor of 3. Consequently, the layer-layer interaction is reduced, and a gentle sonication can dissolve part of the graphite crystals and produce graphene sheets. Despite good results, graphene sheet sizes vary of about 2 orders of magnitude. In addition structural damages are frequently reported [4]. Intercalation is also the process which permits to obtain a good Li-ion density inside the graphite electrode, and is therefore fundamental in energy storage applications [2]. Many experimental studies on graphite intercalation have been performed in the last 40 years [5–8]. The detailed physical-chemical description of intercalation is however still under debate, as well as its effects on graphite structure and morphology.

Graphite is one of the allotropic forms of carbon, which consist in a stacking of planes of linked exagons of bonded carbon atoms (graphite layers). These planes are displaced from one another: graphite can present ABA hexagonal stacking or rombohedral ABC stacking. The rombohedral stacking is however unstable and therefore less common in nature. In both configurations the interplanar distance is 0.335 nm, while the C-C bond length is 1.42 [9]. Both stacking configurations and their lattice parameters are reported in **Figure 1.5**:

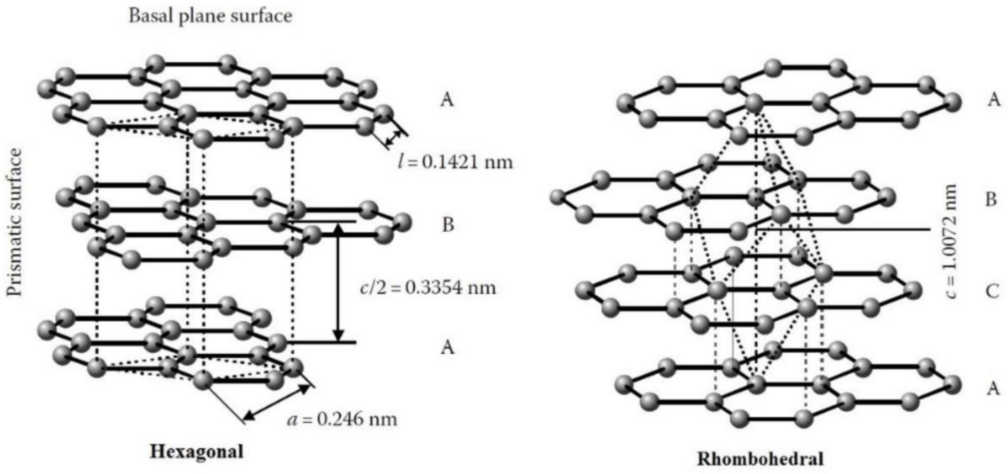

Figure 1.1: ABA hexagonal stacking (a = 0.246 nm, c/2 = 0.335 nm) and ABC rombohedral stacking (c = 1,007 nm) [9].

Carbon atoms in graphite have sp^2 hybridization. A strong σ-bond is formed by the sp^2 orbitals of one carbon and its three planar neighbours that constitute the exagonal structure. These bonds are responsible for all the main thermal and morphological characteristics of graphite in the basal plane. Along the z-direction, the $2p_z$ orbitals form weak Van der Walls π bonds, by overlapping with other $2p_z$ orbitals which belong to a neighbour graphite layer. The difference in strength between σ and π is responsible for the mechanical anisotropy between the planar and the z direction of the graphite crystal. **Figure 1.2** shows the Brillouin zone of graphite reciprocal lattice. Although the interplanar interaction is small, it has profound effect on the four π-bands at the Brillouin zone edges, causing a band overlap which is responsible for the semimetallic properties of graphite [5, 10, 11].

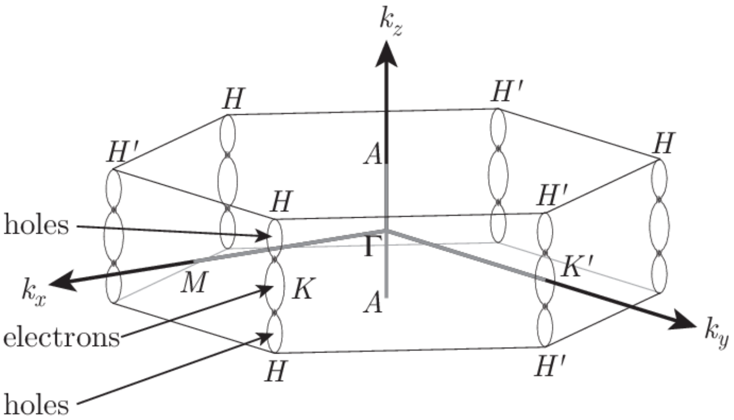

Figure 1.2: Graphite Brillouin zone, showing high symmetry points and a schematic representation of the graphite electron and hole Fermi surfaces along the HK axes [5].

Figure 1.3 shows the electronic bands of graphene and graphite. Graphene consists in a monoatomic sheet of carbon atoms, we can thus consider graphite as an ∼ infinite pile of graphene layers. Graphene has conical bands at the K point and is a zero-gap semiconductor. Graphite, as described before, presents instead a slight band overlap at the K point generated by the interplanar interaction, and is therefore a semimetal [10–12]. Intermediate electron bands are characteristic of few-layer graphene systems. As will be explained in the next Chapter, this difference in the electronic bands has an effect on the Raman spectral features.

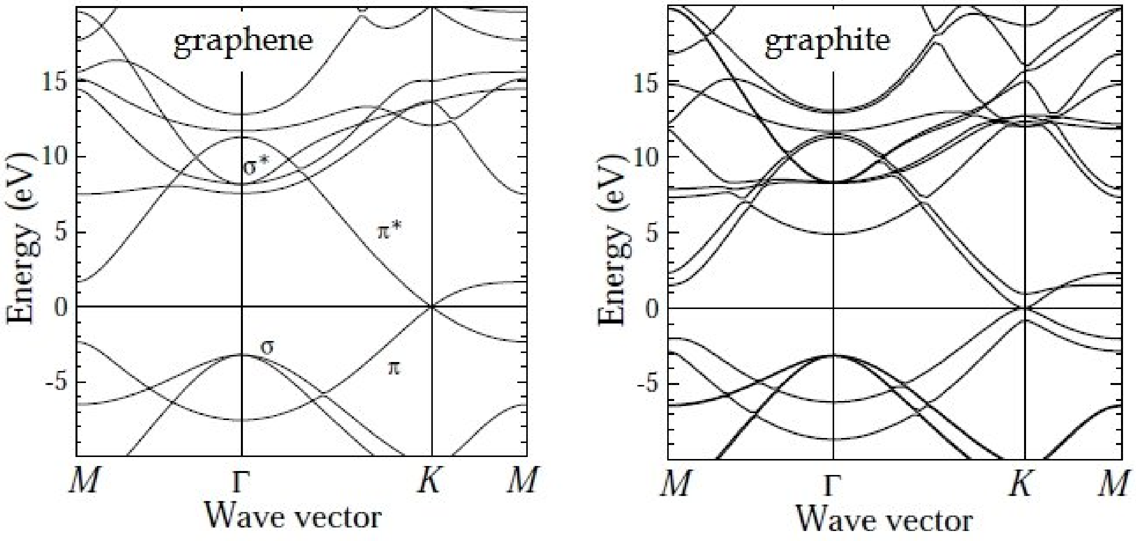

Figure 1.3: Electronic bands of graphene and graphite [10].

Anisotropy is exploited in the form of an artificial graphite crystal, such as Highly Oriented Pyrolytic graphite (HOPG), which shows significantly increased electronic and mechanical properties. HOPG origins from pyrolytic graphite, a material produced from thermal decomposition of carbonaceous gasses in petroleum coke, usually methane. HOPG is formed when pyrolytic carbon is heated again at high temperatures and under high pressures, which permits to align the crystallographic directions. The obtained samples are still polycrystalline, but made of oriented graphite flakes of different sizes (with ABA stacking). The crystallographic direction of the z (out of plane) axis changes slightly in different grains, and the mosaic spread parameter (i.e. the angular parameter) quantifies the reciprocal misorientation of the flakes: the lower the mosaic spread, the higher the quality of the HOPG. In this respect, HOPG quality is categorized with a grade terminology: the highest quality is termed ZYA (spread 0.4 ± 0.1°). Lower quality grades are ZYB (0.8 ± 0.2°), ZYD (1.2 ± 0.2°) and ZYH (3.5 ± 1.5°) [4].

The layered structure of HOPG, regardless of the crystal grade, results in easy delamination along the z axis. One of the easiest way is mechanical exfoliation by adhesive tape, which permits to easily prepare freshly exfoliated and atomically flat samples. A single sample can therefore be manipulated, studied and then re-exfoliated many times. Due to the low interaction of the out of plane π orbitals with the environment, HOPG surface is quite inert and stable in air for several hours.

These properties makes HOPG an ideal, user friendly and inexpensive sample for investigation by high resolution microscopies, such as scanning tunneling microscopy (STM) and atomic force microscopy (AFM). For the same reasons and thanks to the high degree of crystallinity, HOPG is an ideal sample for spectroscopy techniques, in particular Raman spectroscopy.

In view of industrial applications in a broad range of fields, such as those mentioned before, many experimental and theoretical studies have been focused on the investigation of physical-chemical properties of HOPG intercalation processes [4, 5, 8, 13]. However some aspects are still debated, such as the role of the basal plane and the characterization of surface defects which form after intercalation. The easiest way to obtain intercalation, which is also the basic principle of devices such as ion transfer batteries, is electrochemical intercalation. By applying an electrochemical potential to an HOPG electrode immersed in an electrolyte, some ions are able to enter inside the stratified structure of graphite. The main advantage of the electrochemical method is the control of the starting time and the kinetics for the ions to intercalate. Traditional electrolytes are sulfuric acid (H_2SO_4), which was used in this thesis work, as well as percloric and nitric acids.

The electrochemical principles of acid intercalation were studied extensively in the past [4, 5]. Acid ions penetrate at precise electrochemical (EC) potentials into the gaps of the graphite layers, and enlarge the interlayer distance. Charges are accepted into the carbon host lattice, according to equations 1.1 and 1.2 which describe a chatodic and anodic process respectively:

$$[C_x] + [M^+] + e^- = C_x^- + M^+ \tag{1.1}$$

$$[C_x] + [A^-] = C_x^+ + A^- + e^- \tag{1.2}$$

Where M^+ is a cation and A^- an anion. C_x represents a stoichiometric amount of graphite carbon atoms involved in the charge-transger with the electrolyte solution. The product of intercalation is called graphite intercalation compound (GIC), which affects the uppermost layers of the graphite crystal. GIC formation results in a degradation of the electrode surface This degradation causes a loss of efficiency in the batteries. The study of intercalation and surface degradation processes is therefore fundamental to increase the performance of energy storage devices. The GIC structure was tentatively described by a model that suggest the creation of a statistically regular array of occupied/unoccupied layers [5, 7]. The distance between different occupied layers represents different stages of GIC formation, as shown in **Figure 1.4**. In GIC stage n, for example, two layers containing intercalated ions will be separated by (n-1) uncontaminated layers. Stage 1 corresponds therefore to intercalation interlayer spacings between all planes.

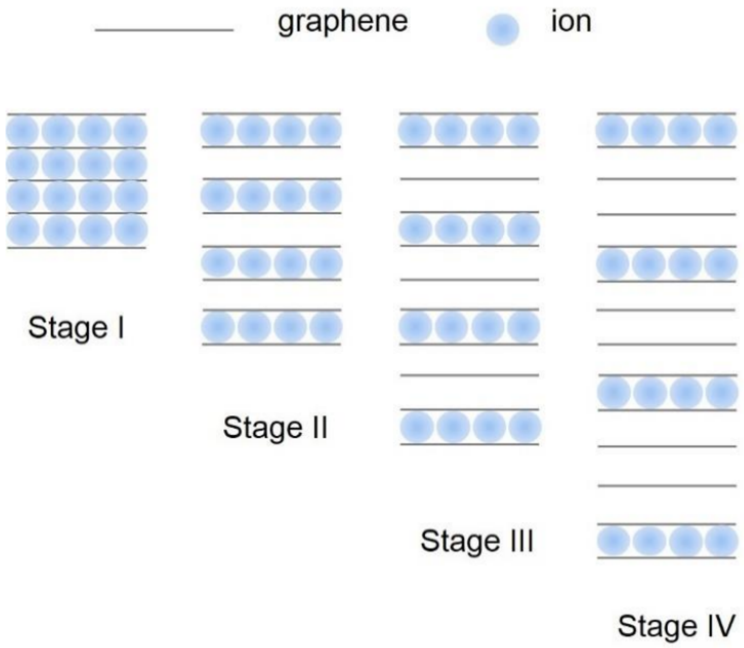

Figure 1.4: Schematic representation of intercalation stages in four different GIC configurations. Grey lines are graphite layers, and balls represent the intercalated ions.

GIC formation is a complex fenomena, where many other effects occur on the graphite basal plane than simple ordered insertion of ions between the layers. One of the most interesting aspects related to intercalation with some acid species, for example sulfuric acid, is the growth of swelled regions in the HOPG basal plane, similar to bubbles, called blisters. Blisters where discovered with AFM techniques, and their structure and formation mechanism remain not completely clear.

A first interpretative model which succeeded in summarizing the experimental results on blisters was introduced by Murray and coworkers [14]. **Figure 1.5** shows the different steps of the model. Two basic ideas characterize the Murray model: 1) ions intercalate inside HOPG trough crystal defects (such as steps, grain borders, holes, kinks, adatoms, valleys) of the basal plane. 2) The inter-layer spacing allows the intercalation of solvated anions. Under these assumptions, solvated anions oxidize carbon as soon as high EC potentials are applied to the graphite electrode, forming electrochemical graphite oxide (EGO). HOPG oxidation produces specific gasses (CO, CO_2, O_2) that start to swell the graphite surface, resulting in blister formation under a "skin" of some graphite layers. The blister size is contained by the graphite skin strain, which stabilizes the surface morphology [14].

Murray model seems confirmed by recent micromechanical studies, which show that con-

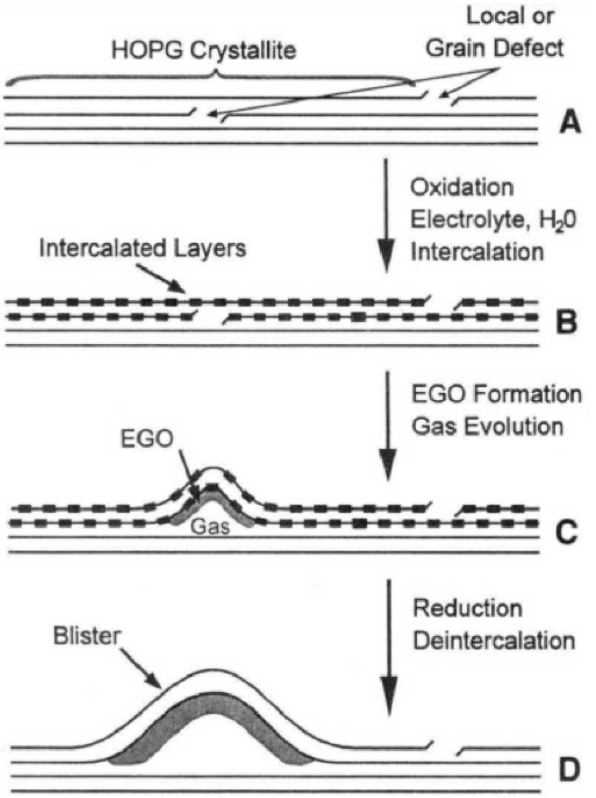

Figure 1.5: Model of blister formation and growth: A) cross section of HOPG basal plane before intercalation. Lines display HOPG (graphene) layers. Local defects are also depicted. B) oxidation takes place when HOPG is positively biased. C) gas starts to form and results in blister growth under some layers of the basal plane. D) final and stable blister structure [14].

siderable pressures (1-10 MPa) are present inside blisters, consistent with the hypotesis of gas formation as the cause of the swellings [15]. In-operando measures also showed that blisters forms during the de-intercalation of ions, a process which happens as the potential of the HOPG electrode is brought back to low potential after intercalation (anodic sweep, explained in detail in section 3.2) [8].

To deeply understand how HOPG properties change in presence of GIC, spectroscopy studies, in particular Raman spectroscopy, have also been conducted [8, 13]. New features appear in the Raman spectrum as a consequence of intercalation. Alongside the characteristic peaks of the pristine sample, the G and 2D peak, 2 more peaks evolve during the process. The formation of defects, due to the acid solution action, causes the appearence of the D peak, which can be considered a measure of the structural disorder in carbon bonds that influence the vibrational properties of the sample. The other peak, referred in literature as G_i, evolves during the EC process and is related to the presence of GIC and its effect on the interplanar distances of HOPG [8]. Although these observations have been argued for a long time, the correlation between the peaks in the Raman spectrum and the HOPG surface morphology is still unclear.

The possibility of this correlation is the core of this thesis work. I conducted a statistical analysis on intercalated HOPG blisters with the use of an innovative AFM-Raman combined apparatus. This system permits to precisely allign the Raman laser beam to the AFM tip in reflected light configuration. This setup permits to study opaque samples (like HOPG) and obtain local Raman spectra of selected regions of the sample. One impressive feature is the possibility of AFM correlation with Raman maps. Raman mapping technique consists in the acquisition of many spectra in grid. By extracting features of interest of the spectra (i.e. the intensity or position of a peak) it is possible to obtain spectral "images" of the surface, which give information that can be correlated with the AFM morphology and obtain intuitive visualizations of the spectral modifications in different regions.

Intercalated HOPG seems an ideal case study for this technique since it is a nanostructured and complex system. Blisters are micrometric (most blisters have diameters $< 1\ \mu m$) structural modifications of the basal plane and result, as it will be demonstrated in this thesis work, in a distinctive change in the Raman spectra compared to the intercalated basal plane. This study goes beyond non-local Raman studies on intercalation: with this combined microscopic approach, more information is obtained, and a clear correlation between topographic and spectral information can be drawn.

Blisters present a complex interplay of phenomena which influence the Raman spectra. To understand the phenomenology it is therefore essential a thorough study of the experimental and theoretical background on Raman spectroscopy of graphite, mono and few-layers graphene, and related systems.

I therefore decided to dedicate Chapter 2 to a review of Raman spectroscopy fundamentals and to explain the effects on the graphite Raman spectrum of different phenomena such as strain in graphene layers, the number of graphene layers, and HOPG intercalation. This background will be essential to understand the discussion of the results.

Chapter 3 is devoted to the description of the other experimental techniques fundamental for the combined approach employed in this work: AFM and electrochemistry. In this chapter I will also present the combined AFM-Raman experimental setup used for the statistical analysis on blisters.

Chapter 4 syntetically shows the experimental procedure and the main results of the measurements. It is also a guide for graphs and maps interpretation, important for the subsequent discussion.

Chapter 5 consists in detailed statistical analysis of all the acquired results. The main scope of this discussion is to try to decouple as much as possible the observed spectral features, to explain the cause of each effect and to correlate them with the morphological AFM analysis. This chapter will clearly show the potential of the combined investigation, as well as its current limitations.

In the final chapter, a summary of the results and possible research perspectives for the future are presented.

Additionally, 2 appendix are added at the end of this work. Appendix A focuses on the preliminary analysis devoted to the identification of the best experimental procedures and parameters. Appendix B is instead a summary of all acquired blisters spectra.

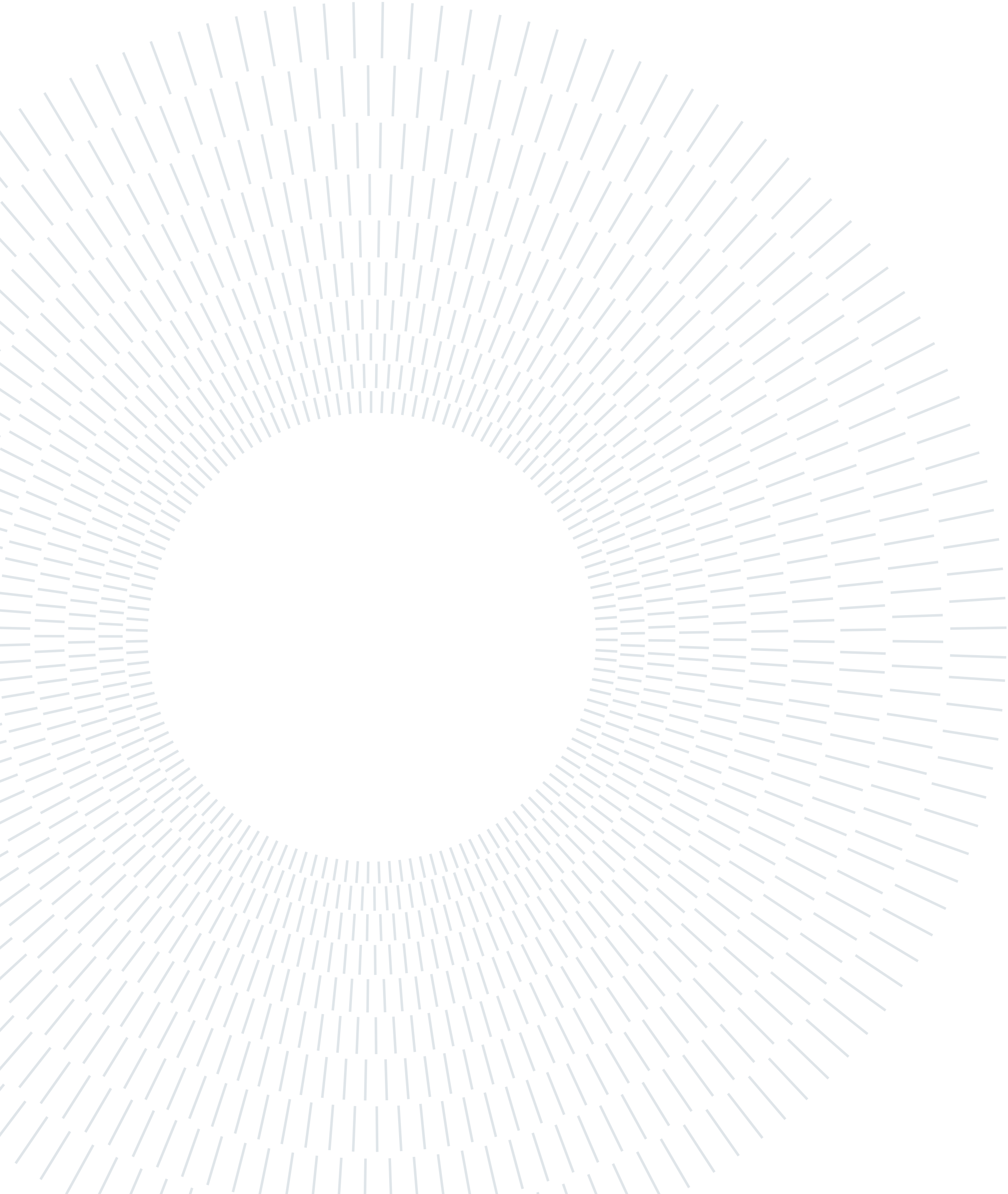

2 Raman spectroscopy fundamentals and literature

As explained in the introduction, electrochemically formed blisters are complex systems. As a consequence their Raman analysis is complicated by the interplay among several effects. In order to clarify the discussion of the experimental results, a detailed review of Raman spectroscopy of graphite and graphene is reported in this chapter. Effects observed in the literature on intercalated HOPG, and in model systems like few-layers graphene flakes, uniaxially strained graphene sheets, and mono and bi-layer graphene bubbles are the basis for the interpretation of blisters spectra. The relevance of the experimental and theoretical results reported in this chapter will become clear as the discussion unfolds.

2.1. Principles of Raman spectroscopy

Raman spectroscopy is a branch of vibrational spectroscopy based on inelastic light scattering. The effect was theoretically predicted by Adolf Smekal in 1923 [16], and experimentally observed in organic liquids by Raman and Krishnan in 1928, using a mercurium vapour lamp with $\lambda = 485nm$ [17]. Raman spectroscopy had very limited application for many years because of the very low efficiency of the inelastic scattering process and the high costs of the apparatus. Significant development and enhancement to Raman spectroscopy structures allowed to overcome those limitations, and the technique is nowdays an important non-destructive approach to study materials chemistry. Laser sources are the most commonly used. The diffused light is collected and analyzed by a spectrometer consisting in a monochromator, which splits the diffused beam, and a detector [18].

When monochromatic light is scattered by a material the majority of the radiation undergoes Rayleigh elastic scattering, where the system is excited to a virtual state, and then re-emits radiation with the same energy of the incident light. A small fraction of the emitted light, however, is observed to have a slightly different wavelength from the incident one. This is the Raman effect and is due to the interaction of the light electromagnetic (EM) field with the matter, which results in a perturbation of the matter charge distribution and can lead to the exchange of energy and momentum between the two systems, leaving matter in a modified state. In the case of a molecule, the interaction can bring the system to a different (ro-)vibrational state. In the case of a crystal lattice, the energy transfer creates/absorbs a quantum of vibration in the lattice known as a phonon. Raman scattering in crystals can also lead to the excitation of paramagnetic ions, surface plasmons and spin waves [18, 19].

The energy conservation for the system can be written in the following way, which highlights the shift in frequency between the incident and scattered photon:

$$\hbar\omega_{scatter} = \hbar\omega_{inc} \pm \hbar\omega_{vib} \tag{2.1}$$

Where $\hbar\omega_{scatter}$ refers to the energy of the scattered photon, $\hbar\omega_{inc}$ is the energy of the incident photon and $\hbar\omega_{vib}$ correspond to the energy transfer between the light and the system vibrational modes.

The emitted photons can have lower energy (bigger wavelength) than the incident radiation, which correspond to an excitation of the lattice modes of the system with the creation of a phonon, and the resulting emission peaks are called Stokes lines of the Raman spectrum. The interaction with the crystal can however result also in the absorption of a phonon and the emission of photons at higher energy (shorter wavelength) than the incident photon. These interactions correspond to the Anti-Stokes lines of the spectra (**Figure 2.1**). Anti-Stokes interactions are less probable because the population of the vibrational energy levels is governed by thermal Bose-Einstein statistics.

In molecules or crystals, the charge distribution has an equilibrium state to which it tends. An externally applied field can modify or perturb the charge distribution but only in accordance with the molecule or crystal's ability to form dipoles which may be anisotropic. This anisotropic property of molecules and crystals is called polarizability or dielectric susceptibility, respectively. The classical approach theorises that the existence of Raman effect is associated with a modulation of the polarizability (for molecular vibrations) or of the dielectric susceptibility (for crystal lattice vibrations).

Because of the small wave vector of the incident and scattered photons, first-order Raman spectroscopy is limited to the observation of lattice modes close to the Brillouin zone centre (q = 0 phonons). Only few q = 0 vibrational modes are Raman active, because of selection rules that can be determined by analyisis based on group theory. It often happens that Raman-active modes are inactive in the infrared (IR) and vice versa, Raman spectroscopy therefore provides complementary information to IR spectroscopy. [18, 19].

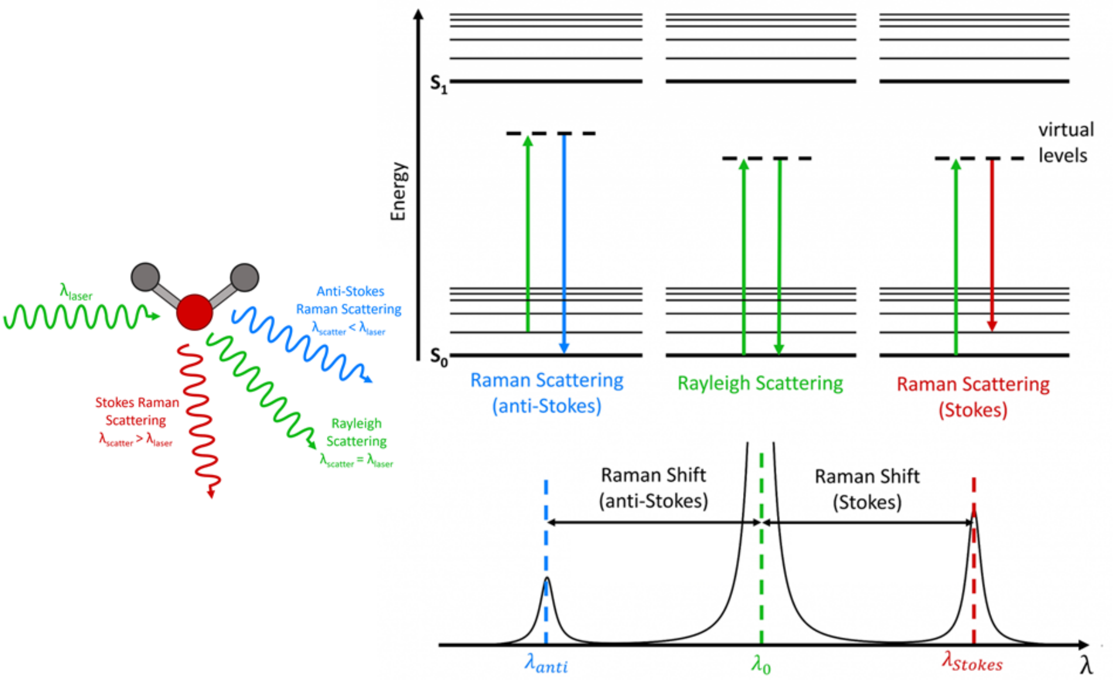

Figure 2.1: Schematic representation of the Raman effect depicting Stokes and Anti-Stokes processes

Information on the phonon dispersion relations for other points in the Brillouin zone can however be obtained from second-order spectra, where contributions are made by pairs of phonons with wave vectors q and q', as illustrated in **Figure 2.2**. Second-order Raman peaks are generally broad, because many phonon pairs with different energies contribute to the line, and the resulting band emphasizes those regions in the Brillouin zone having high densities of states [5, 18].

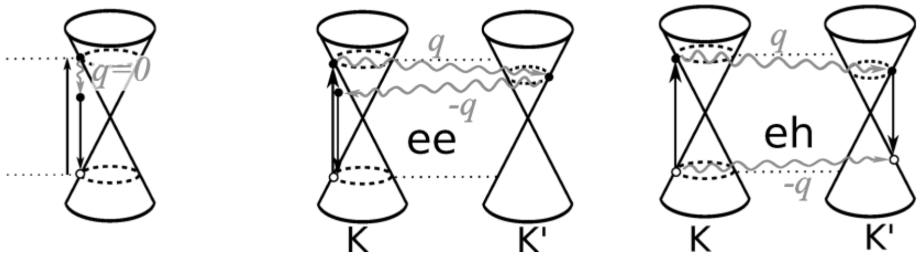

Figure 2.2: Schematics of the 1st (left) and 2nd order (right) Raman scattering processes for materials presenting conical bands at the K point of the BZ (such as graphene). ee processes correspond to two consecutive electron-phonon interactions, while eh processes consist in a electron-phonon interaction followed by a hole-phonon interaction.

2.2. Raman spectra of graphene and graphite

The Raman spectra of all carbon systems show only a few prominent features, with a couple of very intense bands in the $1000 - 2000\ cm^{-1}$ and a few 2nd-order modulations. However their shape, intensity and positions allows to obtain as much information as that obtained by a combination of other lengthy and destructive approaches. Raman spectra of carbon films are dominated by sp^2 sites, because visible excitations always resonates with π electrons [20, 21]. The first order features of graphite are the G peak at around $1580cm^{-1}$, which corresponds to the lattice E_{2g}^2 vibrational mode at the Γ-point of the phonon dispersion relation [12] (**Figure 2.3**), and the D peak at around $1360cm^{-1}$, associated with vibrational mode A_{1g} . The interpretation of the D peak is not straightforward. In some papers it is identified as a mechanism of interband double resonance (DR) close to the K-point of the phonon dispersion relation. At the K-point there is a minimum of the direct bandgap of the electrons, this means that electron optical transitions happens too. Raman resonance has two consequences: the intensity of the peak is higher with respect to a normal peak, and the energy shift is dependent on the excitation wavelength. The D peak is however silent in defect-free HOPG and can be interpreted as a sign of structural disorder. Another feature that appears with defected carbon structure is the D' peak at around $1620cm^{-1}$ which is instead generated by intraband DR process at the K-point [20, 21].

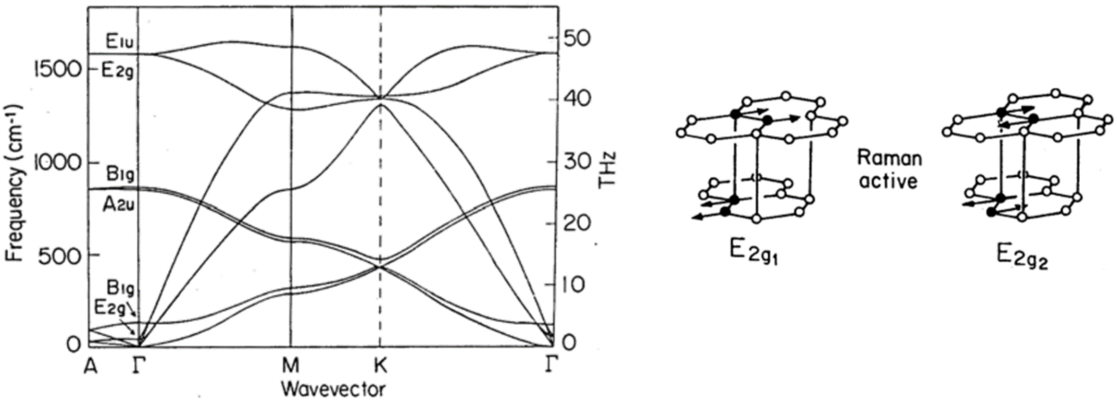

Figure 2.3: HOPG phonon dispersion relation and Raman-active in-plane vibrational modes E_{2g_1}, and E_{2g_2}, which involve $q = 0$ phonons at the Γ-point [12].

As described in the introduction, graphene, and graphite present different electronic bands (see Figure 1.3). Because of DR, the electronic structure has an influence on the Raman spectrum, which thus presents different features in mono, bi and few-layers graphene, until it approaches the bulk HOPG situation (∞ layers). **Figure 2.4** compares the Raman spectra of monolayer graphene and bulk graphite measured at $514.5nm$ excitation. The two most intense features are the G peak at $\sim 1580cm^{-1}$ and a band at $\sim 2700cm^{-1}$, historically named G'. This band was however identified as the second order of the D peak, always present even in the absence of the D peak itself [20, 21]. It was therefore named 2D band in latter literature, a choice I will follow in this thesis work. The D and 2D band Raman shifts, being DR peaks, are dependent on the laser excitation, with a rigid shift of about 100 cm^{-1}/eV [22][1]. The spectra show a marked change in the intensity and shape of the 2D peak of graphene compared to bulk graphite. The 2D peak in bulk graphite consists of two components $2D_1$ and $2D_2$ roughly 1/4 and 1/2 the height of the G peak, respectively. Graphene has instead a single, sharp 2D peak, roughly four times more intense than the G peak [20].

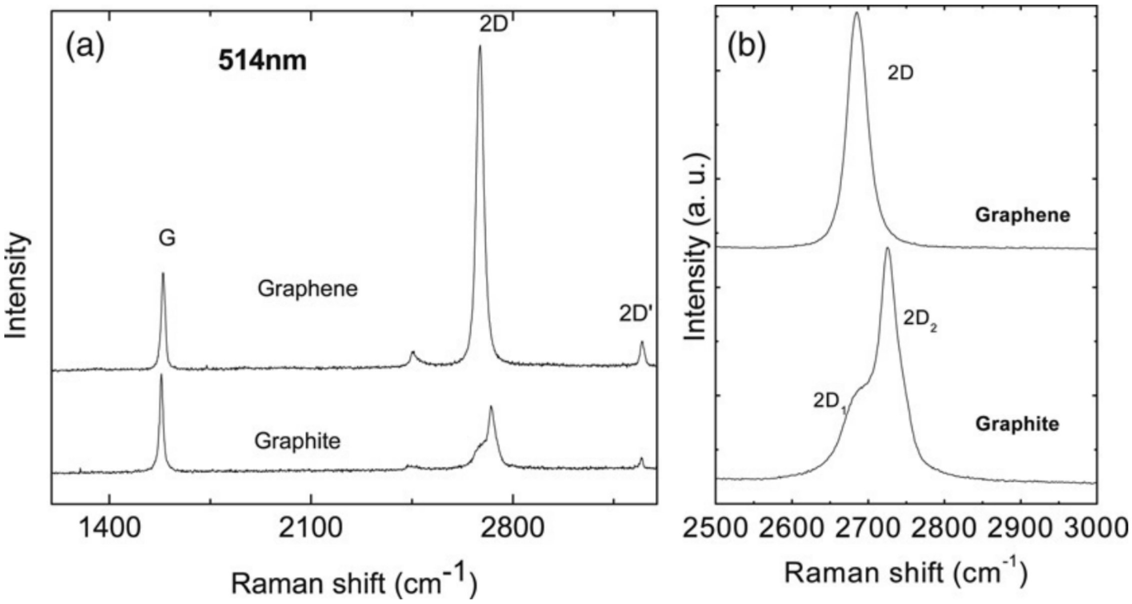

Figure 2.4: a) Raman spectrum of graphene and HOPG for 514 nm excitation b) detail of the 2D peak showing a single $2D$ component for graphene and the two $2D_1$ and $2D_2$ components for HOPG [20].

---

[1] I verified this result with Raman measures on pristine HOPG at different excitation wavelengths, see Appendix A.

2.2.1. 2D lineshape in few-layers graphene

Figure 2.5 plots the evolution of the 2D band as a function of the number of layers for 514.5 nm and 633 nm excitations. Bi-layer graphene has a much broader and upshifted 2D band with respect to graphene. This band is also quite different from bulk graphite. It has four components, $2D_{1B}$, $2D_{1A}$, $2D_{2A}$, $2D_{2B}$, two of which, $2D_{1A}$ and $2D_{2A}$, have higher relative intensities than the other two. Figure 2.5 a) show that a further increase of the number of layers leads to a significant decrease of the relative intensity of the lower frequency $2D_1$ peaks. For more than five layers the Raman spectrum becomes hardly distinguishable from that of bulk graphite. Thus Raman spectroscopy can clearly identify a single layer, from bi-layer from few (less than five) layers [20, 21].

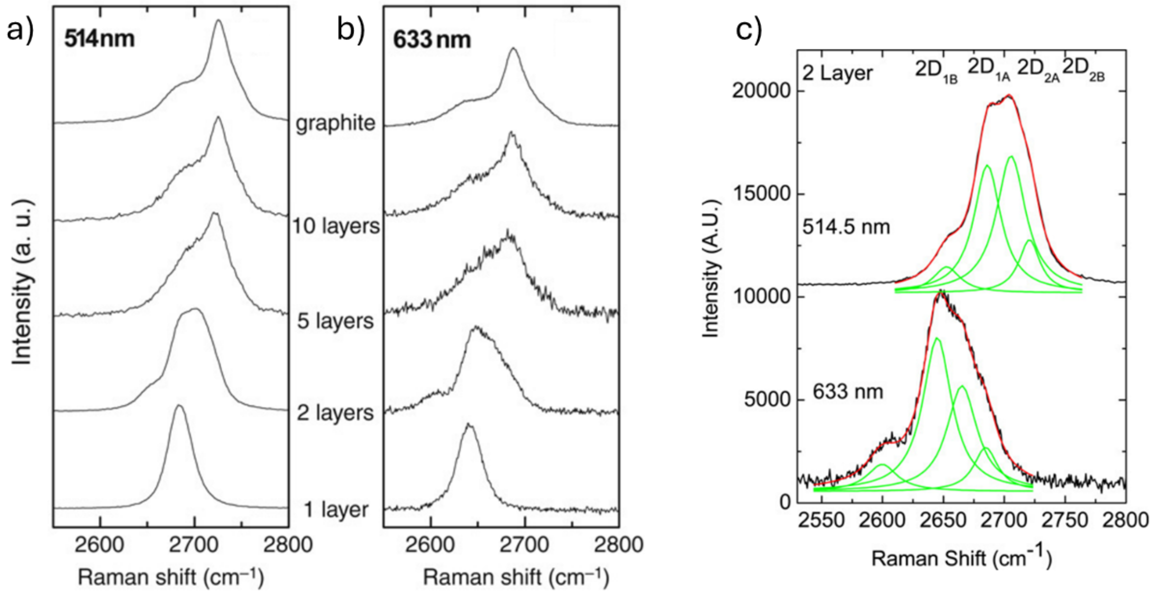

Figure 2.5: 2D peak shape as a function of the number of layers at a) 514 nm and b) 633 nm. c) Fitting of the bi-layer graphene 2D peak at 514 and 633 nm, showing in both cases the 4 components due to the splitting of the phonon dispersion relation at the K-point [20].

2.2.2. G peak enhancement in graphene flakes deposited on SiO_2

It would be logical to assume that the intensity of the Raman signal, measured as the intensity of the G peak, presents a monotonical increase with the number of graphene layers. The situation is however more complex since the intensity of the G peak in mono and few-layers graphene is highly dependent on the substrate material. Few-layers graphene flakes on a SiO_2 substrate show a marked enhancement of the G peak, with an absolute intensity up to more than 5 times that of HOPG and a maximum at around 10 layers, while monolayer graphene (on this substrate) and graphite present similar intensities [23, 24]. This effect is shown in **Figure 2.6**. The mechanism of this enhancement is attributed to reflection and interference effects at the interfaces with the substrate, and the authors suggest it as a possible method to quantify the number of layers. Yoon et al. propose to combine both G absolute intensity and 2D lineshape information to accurately evaluate graphene flakes thicknesses [24]. Further studies should be performed to clarify the mechanism in other systems and interfaces.

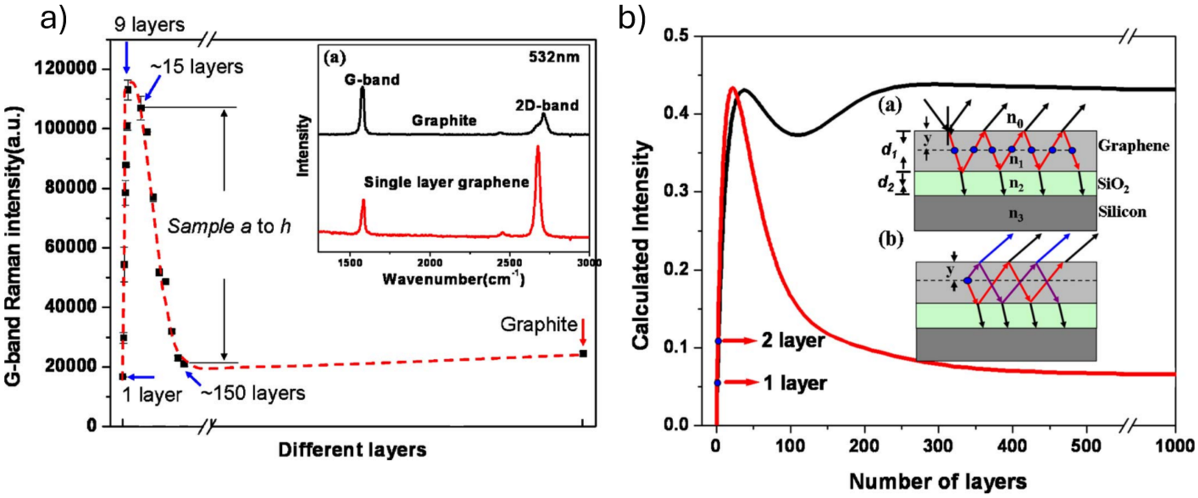

Figure 2.6: a) experimental enhancement of the G band in few-layers graphene flakes of different thicknesses deposited on SiO_2 b) theoretical curve calculated based on an interference mechanism model, which happens at the interface with SiO_2 [23].

2.2.3. Raman spectra of intercalated HOPG

For intercalated HOPG, the high symmetry of the graphite lattice is an approximate symmetry for the larger real space unit cell due to the presence of the intercalation compounds. This approximate symmetry gives rise to zone-folding phenomena through which certain non-zone-centre q-vectors for graphite are mapped into the zone centre for the intercalation compound, thereby turning on new Raman-active modes [12]. The most distinctive feature of H_2SO_4 ion intercalation is the appearance of a new G component at around $1610cm^{-1}$, called G_i peak (intercalation G), strictly related to the chemical action of the intercalated acid, as shown in **Figure2.7** [8, 25]. For stage 1 intercalation the original G peak becomes silent [12]. The intensity of the G_i peak is a qualitative mark of the intercalation in particular region. Intercalation also damages the HOPG structure, marked by the appearance of the D peak at $1350cm^{-1}$ [6, 8, 13, 25, 26]. The D' peak at $1620cm^{-1}$ can also be present due to alterations in the graphitic structure, this can lead to difficulties in the interpretation of the signal since this feature present a Raman shift very close to the intercalation peak G_i. Even if it is not directly correlated to the D peak intensity, the D' feature follows a similar evolution [13], therefore if the D peak has low relative intensity we can assume that the 1610 cm^{-1} feature is mainly due to the intercalated acid effect on the interplanar HOPG distance.

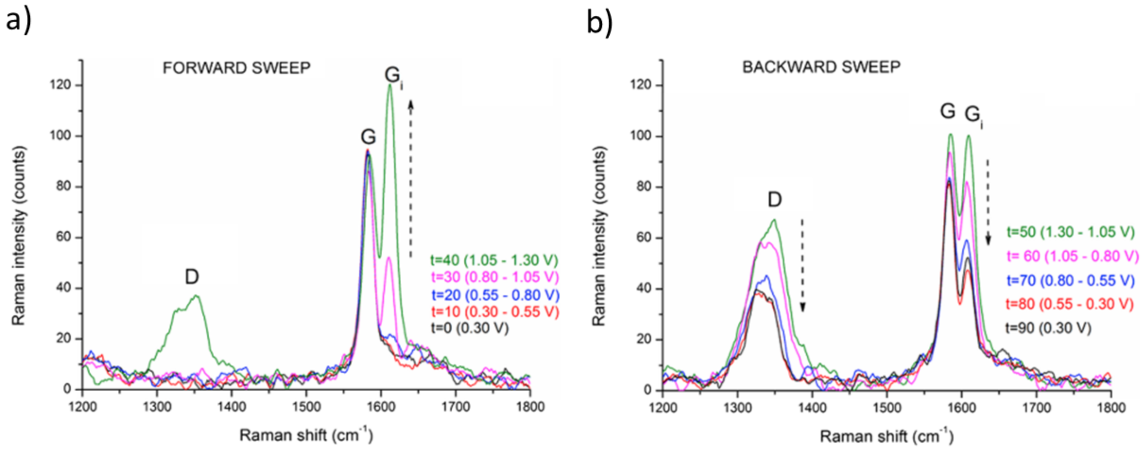

Figure 2.7: Raman spectra ($\lambda = 632.8nm$) of an HOPG sample during a CV (0.3-1.2 V, 25 mV/s): a) forward potential sweep and b) backward potential sweep. Raman spectra collected at different potential values during the EC cycle in 1 M H_2SO_4 are plotted with a common intensity scale [8].

2.2.4. Strained mono and bi-layer graphene

Strain in mono or few-layer graphene sheets can be efficiently studied by Raman spectroscopy since it modifies the crystal phonon frequency, depending on the anharmonicity of the interatomic potentials of the atoms. Several experimental and theoretical works studied uniaxial strain in graphene, showing that this leads to softening of the phonon vibrational modes for tensile strain and a subsequent downshift of the G peak (at lower position, the emitted photon is more energetic). For high enough %strain it is reported that the G peak splits into two components, called (G^-) and (G^+) as shown in **Figure 2.8**. This split is caused by degeneracy removal of the vibrational modes, since strain is anisotropic [27–29]. Mohiuddin at al. report a rigid shift of the G^- component, correspondent to the vibration modes parallel to strain direction of $-31.7cm^{-1}/\%$, while the G^+, correspondent to the perpendicular direction, shifts of $-10.8cm^{-1}$. The 2D band also presents a shift of $-64cm^{-1}/\%$ [27].

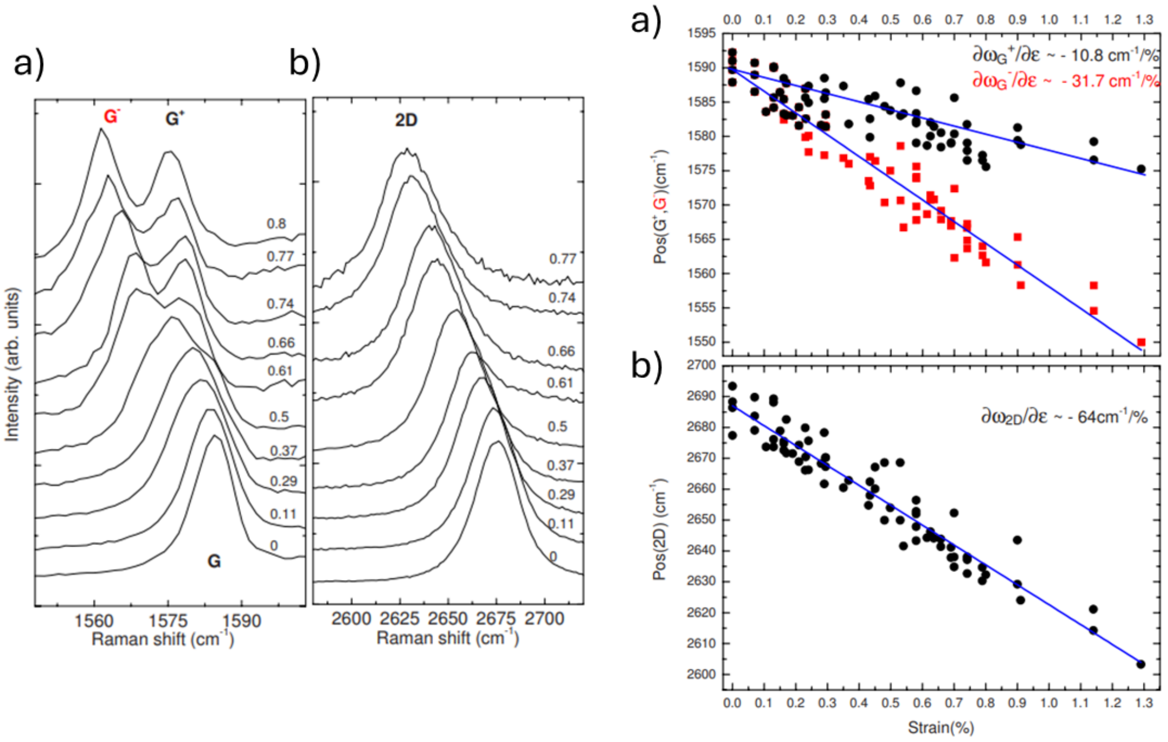

Figure 2.8: Lineshapes and shifts in function of % strain of a) G peak b) 2D peak in uniaxially strained monolayer graphene [27].

Fewer works investigated biaxial strain [30–32]. Zabel et al. for example studied the effect on a bi-layer graphene membrane deposited on Si/SiO_2 and inflated with $N_{2(g)}$ up to 2 bar. The artificial bubbles have diameters of 5-10 μm and heights of hundreds of nanometers, comparable to blister dimensions. In biaxial strain no split is observed since isotropy is not broken. A rigid shift of the G and 2D bands is instead observed. The maximum strain measured was 1.2 %. The 2D peak shape does not change at these pressure values. The authors claim also that the AB stacking configuration of graphene is not altered, because the % strain is too low [31].

3 | Experimental Techniques

This chapter describes the main features of Atomic Force Microscopy and Electrochemistry, which coupled with Raman spectroscopy are the experimental techniques central for this thesis work. The combined AFM - Raman experimental setup used for the analysis setup is also described in the latter part of the chapter.

3.1. Atomic force microscopy

Atomic force microscopy (AFM) was developed in 1986 by Binnig, Quate and Gerber [33]. Its working principle relies on the interaction forces that arise between the sample and a sharp tip, normally made of silicon, which is mounted on the end of a soft cantilever spring. During the scanning, the interaction perturbs the spring and its deflection is measured with an optical system. This consists in a laser beam which impinges on the cantilever and is reflected onto a 4-quadrants photodiode that measures the vertical deflection (DFL) and lateral friction (LF) of the spring as currents, as shown in **Figure 3.1**. This signal activates a feedback loop and piezoelectric actuators change the sample (or the tip) height so that the system can correctly follow the morphology of the sample. Since the interaction forces can be electrostatic, frictional, capillar and magnetic, AFM is a suitable technique for a wide range of materials [34, 35]. The AFM lateral resolution is closely related to the tip radius, which is in the order of the tens on nanometers, but atomic vertical resolution is achievable. For HOPG samples, for example, it is possible to identify terraces corresponding to single atomic planes (0,3 nm). In principle AFM can work in any kind of environment (vacuum, air and liquid). The first application of AFM in an EC cell was performed by Kouzeki et al. in 1996 [36].

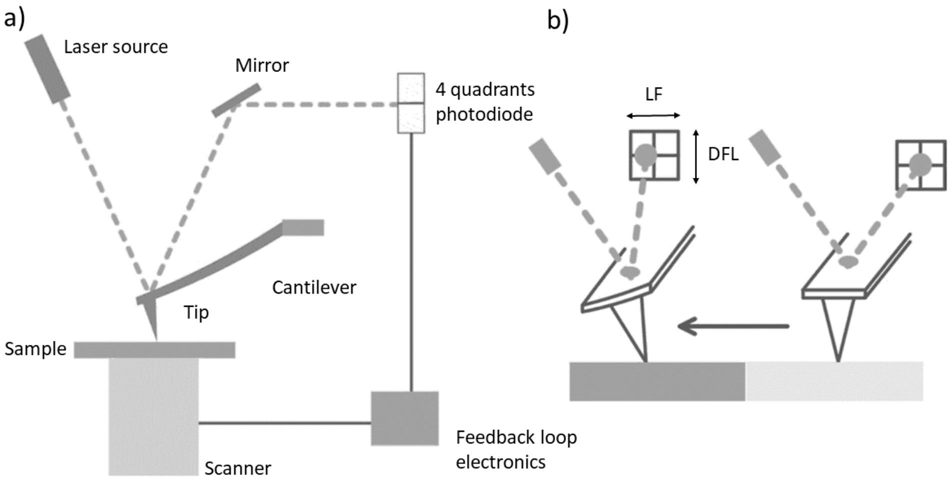

Figure 3.1: a) schematic representation of the AFM setup b) representation of the DFL and LF signals measured with the optical system that are used as signal for the feedback loop system [37].

3.1.1. Fundamentals of AFM

The tip-surface interaction can be qualitatively modelled by the Lennard-Jones potential [38, 39]:

$$U_{LJ} = \varepsilon \left[\left(\frac{r_0}{r} \right)^{12} - 2 \left(\frac{r_0}{r} \right)^{6} \right] \tag{3.1}$$

Where ε is the depth of the potential well and r_0 the equilibrium distance, where the potential reaches a minimum. The LJ potential is a sum of two exponential terms: the attractive one describes the long-range Van der Waals interactions which follow a $1/r^6$ law, while the repulsive one is due to Pauli repulsion that only arise below 1-2 $\AA$ (atomic radius), and is modelled by a $1/r^{12}$ dependence [38–40]. A full description of the tip-sample interaction should also take into account specific short range adhesion/contact forces, which can be modelled using different theoretical models such as the Bradley theory, the Derjaguin-Mfiller-Toporov (DMT) theory [41] or the Johnson-Kendall-Roberts (JKR) theory [42]. For in-liquid measurements capillarity attractive forces exercised by the liquid meniscus created between tip and sample are also present.

AFM imaging acquisition can be divided into static and dynamic modes. In the static (contact) mode the AFM tip works in the repulsive region of the LJ potential. The interaction force is kept constant by the piezoelectric actuators. In the dynamic (non-contact or tapping/intermitted conctact) modes, conversely, the cantilever is kept in oscillation, and the tip can explore both attractive and repulsive region of the potential, as shown in **Figure 3.2**. The non-contact mode is to be preferred for fragile samples, to avoid the possibility of damaging the surface, at the expense of a reduced lateral resolution [34, 35]. Non-contact mode can also reveal qualitative information about the chemical heterogenity of the surface: when the tip-sample interaction change a phase shift can occur: in phase-contrast imaging the phase lag is monitored during the scanning. Several contributions have investigated the potential of phase-imaging to dectect variations in material properties such as hardness, adhesion, elasticity and viscoelasticity [43, 44]. Dynamic acquisition can further be divided in two methods: amplitude-modulation (AM) and frequency-modulation (FM). In AM-AFM, the scanner actuator is driven at defined potential amplitude V_i and frequency f_i close to the resonance frequency f_0 of the cantilever. When the tip approaches the sample (in the repulsive region) elastic and inelastic interaction change both V and f with respect to the driving signals V_i and f_i, and these changes are used as feedback signals. In FM-AFM the feedback signal is instead represented by changes of the eigenfrequency f_0, which is effected by attractive tip-sample interactions during the scanning.

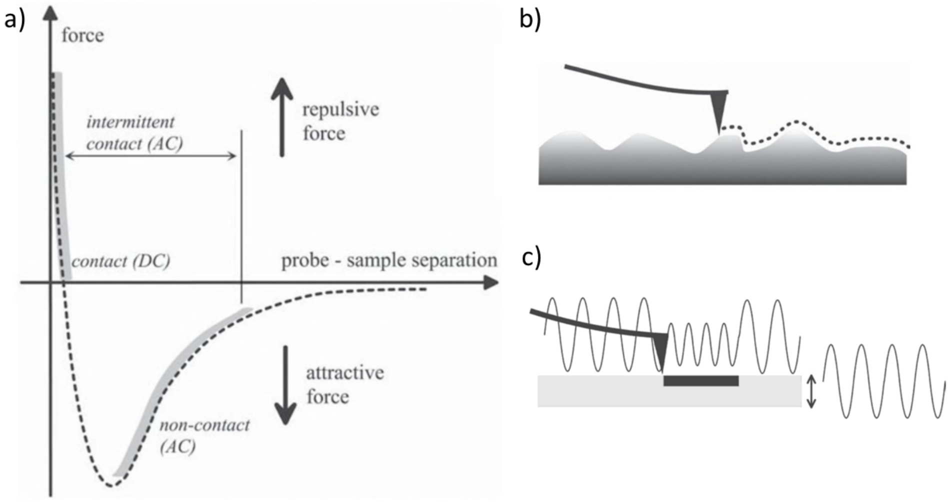

Figure 3.2: a) LJ potential and contact, non contact and intermitted contact mode regions b) pictorial depiction of the contact scanning mode: tip-sample force is kept fixed and the tip directly follows the topography c) AM-AFM dynamic mode: the interaction between the oscillating tip and the sample changes the osc. amplitude during scanning [37].

3.1.2. AFM on Pristine HOPG

While at the naked eye Pristine HOPG seems rough and "bumpy", it shows a very flat surface on AFM scales, where it is possible to appreciate monoatomic terraces. **Figure 3.3** is a 30x30 μm scan of a freshly exfoliated sample. From the section it is possible to appreciate steps of around 0.3 nm, which is the interplanar distance for graphite.

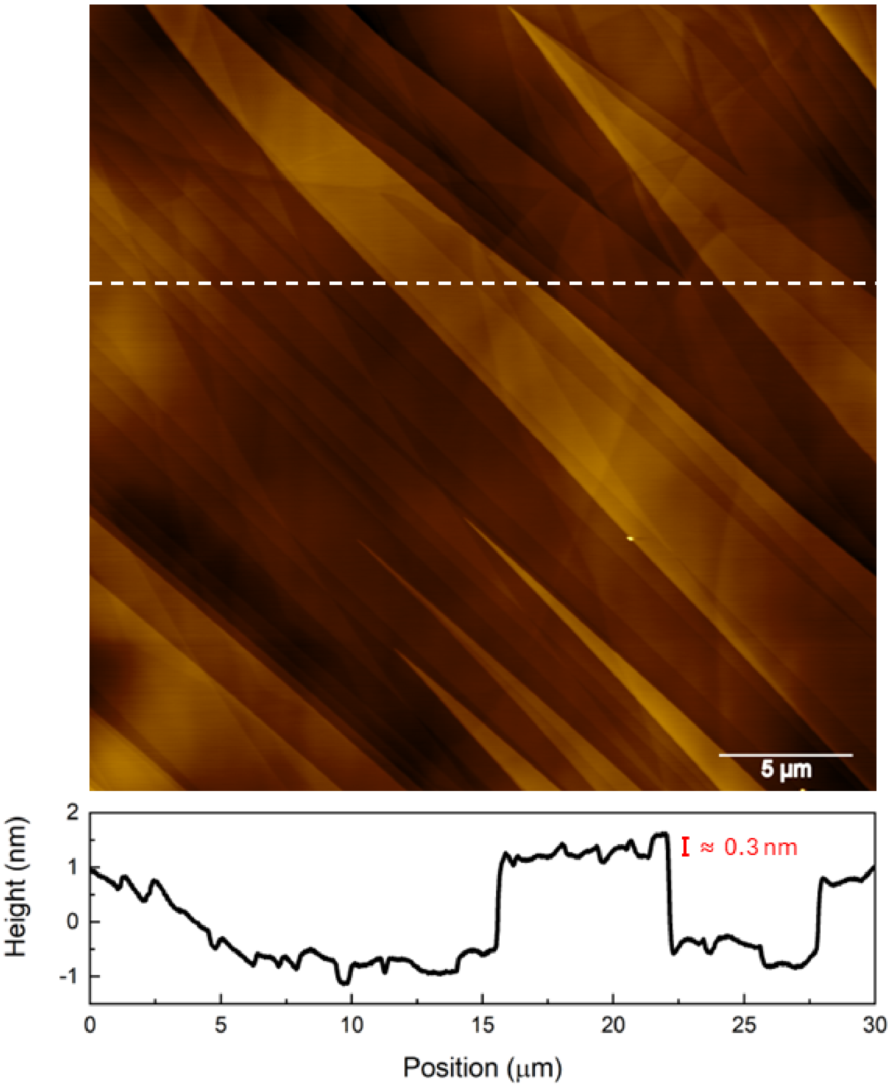

Figure 3.3: 30x30 μm AFM image of pristine HOPG, monoatomic terraces are clearly distinguishable. Image courtesy of Marco Menegazzo.

3.2. Electrochemistry

Electrochemical (EC) techniques are fundamental tools for oxidation and reduction process studies. They are commonly used to study kynetics and thermodynamics of electrons and ion transfer processes such as intercalation [45, 46]. Electrochemistry techniques are divided into static (e.g. potentiometry) and dynamic, where the EC potential (Faradic current) can be controlled, for example coulometry [47]. When the controlled EC potential is tuned in a certain energy range, the technique is known as voltammetry. Here the resulting current I_{EC} is measured as a function of the applied EC potential V_{EC}. A traditional electrochemical setup for voltammetry is the three-electrode cell shown in **Figure 3.4**:

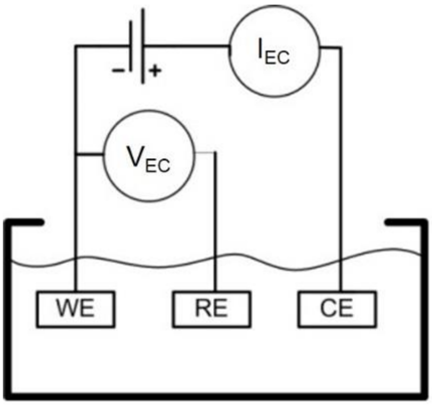

Figure 3.4: Schematic diagram of an electrochemical cell with three electrodes: working electrode (WE), reference electrode (RE) and counter electrode (CE) [6]

The setup consist in a working electrode (WE) a reference electrode (RE) and a counter electrode (CE). Surface oxidation (reduction) takes place at the WE, while reduction (oxidation) occurs at the CE. To balance the total charge of the system the RE has a constant potential inside the electrochemical bath and ensures good reference for the WE. The preferred RE is the standard hydrogen electrode (SHE), which can be realized by a contact between molecular hydrogen and its ions at the interface of a platinum (Pt) wire [48].

The main reaction in this setup is the electron tranfer between the neutral species (H_2) and the H^+ ions:

$$2H^+_{aq} + 2e^- \rightarrow H_{2(g)} \tag{3.2}$$

The EC potential can be calculated from the Nernst equation:

$$E = \frac{RT}{F} ln \frac{a_{H^+}}{\sqrt{p_{H_2}/p_0}} \tag{3.3}$$

Where a_{H^+} is the activity (effective concentration) of the hydrogen and p_{H_2} the gas pressure referred to atmospheric pressure p_0. At 25°C, E = 4,43 V [49], but to be a term of comparison to all other electrode reactions, it is set conventionally to 0 at all temperatures. A typical SHE design is shown in **Figure 3.5**:

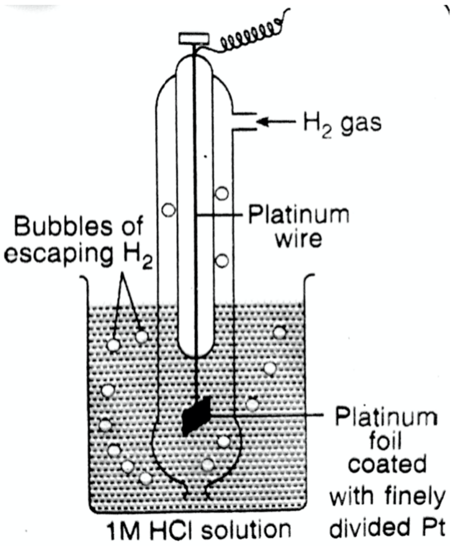

Figure 3.5: Scheme of the standard hydrogen electrode (SHE)

Unfortunately SHE as well as other traditional RE have a limited range of applicability. A Pt wire immersed in an EC cell filled with different electrolytes can however mantain a steady (within few mV) electrode potential with a shift of + 0.740 V vs SHE in diluited H_2SO_4 solutions [50]. Thermodynamic equilibrium cannot exist since there is no common component (anion or cation) in the two adjacent phases.

Pt wire is usually callled quasi-RE (Q-Ref) and shows many advantages: it is very easy to use, it shows low impedance, it does not recquire a salt bridge, it does not contaminate the electrolyte solution, it is stable in many acids and does not disperse undesired ions in the EC solution.

In voltammetry, an EC potential is applied to the WE with respect to the RE to alter the equilibrium conditions, In the presence of electroactive species and ion diffusion (mass transport) from the bulk solution to the WE and CE starts. When ions are close to the electrodes surface, they exchange electrons (redox process) and a faradic current (I_{EC}) is measured between WE and CE:

$$I_{EC} = nAFj \tag{3.4}$$

Where F is the Faraday constant, n the number of electrons per molecule involved in the electrochemical process and A is the WE area [51]. Due to a diffusion process the flux j is related to both the ion concentration Φ $[mol/cm^3]$ and the diffusivity D $[cm^2/s^6]$ by the first Fick's law [52]:

$$J = -\nabla(D\Phi) \tag{3.5}$$

The features observed in a voltammogram are thus related to the type of the ions in the solution, the EC cell temperature, the number of exchanged electrons, the electrodes geometry, the timescale of the measurement, as well as capacitive effects at the electrode/liquid interface, mass transport and surface phenomena that can be involved in the EC process.

3.2.1. Cyclic voltammetry

In cyclic voltammetry (CV) the EC potential applied to the WE is linearly swept starting from an initial value (V_{EC}^i). After reaching a switching potential (V_{EC}^f) the sweep is reversed returning to the initial V_{EC}^i. A typic CV voltammogram is shown in **Figure 3.6**.

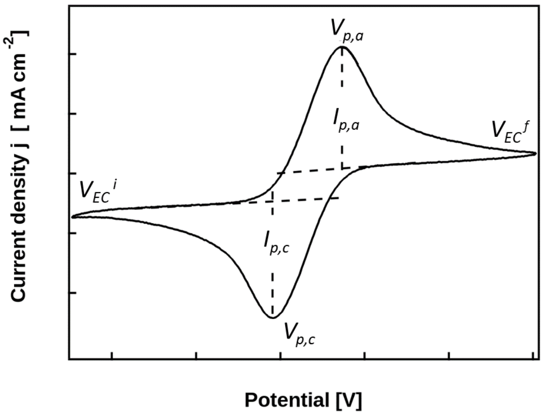

Figure 3.6: Cyclic voltammogram simulated for reversible charge transfer: $V_{p,c}$ chatodic peak potential; $V_{p,a}$ anodic peak potential; $I_{p,c}$ chatodic peak current, $I_{p,a}$ anodic peak current; V_{EC}^i initial potential; V_{EC}^f switching potential.

According to IUPAC convention, the positive potentials are plotted in the positive abscissa direction, therefore the anodic(due to oxidation) currents are positive, while the cathodic ones (due to reduction) are negative. The presence of current peaks indicates that an electroactive couple is present in the electrolyte solution. The main CV parameter is the scan rate ($v_{scanrate} = \Delta V_{EC}/s$). Typical scan rates range from 1 to 1000 mV/s [48]. The scan rate influences the reversibility of the process, which is also influenced by mass transport. If $v_{scanrate}$ is too fast with respect to ion diffusion the WE is polarized and an overportential is required for the oxidation (or reduction) process.

In the case of a reversible process, the intensity of the faradic current I_p is a root-square function of the scan rate, and the $I_{p,a}/I_{p,c}$ ratio is equal to 1. The energy separation ($\Delta V_p = V_{p,a} - V_{p,c}$) is relatively small and corresponds to a value of $\sim 59/n$ mV at 298 K, regardless of the scan rate [45, 53]. If ΔV_p changes as a function of the scan rate, the redox process is quasi-reversible or irreversible (**Figure 3.7**).

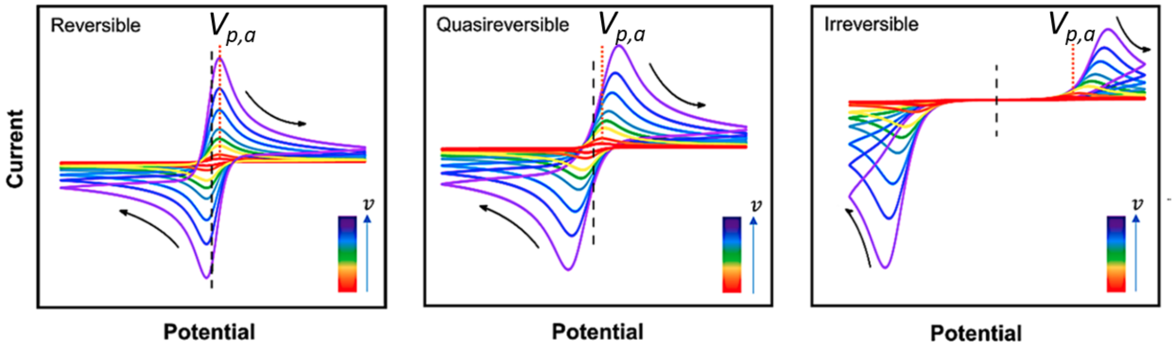

Figure 3.7: CV at different scan rates simulating reversible process ($\Delta V_p \sim 59/n$ mV); quasi-reversible ($\Delta V_p < 200/n$ mV); irreversible ($\Delta V_p > 200/n$ mV) [53].

During the redox reaction, the total charge exchanged can be evaluated from the acquired voltammograms. Traditionally, a linear background is subtracted from the anodic or chatodic peak, and the subtended area is calculated. The latter is proportional to the exchanged charge, as described in the following equation:

$$A_{a(c)} = \int_{V_{EC}^{i}}^{V_{EC}^{f}} i(V)\, dV = v_{scanrate} \int_{V_{EC}^{i}}^{V_{EC}^{f}} i(t)\, dt = v_{scanrate} Q_{a(c)} \tag{3.6}$$

The anodic curve gives rise to oxidation charge (Q_a) while the cathodic feature to the reductive Q_c. The Q_a/Q_c ratio is $= 1$ for reversible EC processes and > 1 for quasi-reversible and irreversible processes [54].

3.3. In-situ AFM-Raman apparatus

3.3.1. Confocal Raman spectrometer

Figure 3.8: Confotec NR500 Raman spectrometer

The Confotec NR500 confocal Raman spectrometer (**Figure 3.8**) can work both on an optical stage or in combination with AFM. It can be divided in 4 parts: the laser sources and the optical path, the Raman optical unit, the microscope and at the end the spectrograph with the spectrometer. The system has 4 laser sources:

1. 632.817 nm red He-Ne laser, power 23 mW
2. 532 nm green solid state laser, power 50 mW
3. 473 nm blue solid state laser, power 40 mW
4. 405 nm purple solid state laser, power 40 mW

Each laser has an independent optical path and is controlled by a shutter. The impinging power can be regulated with a ND filter. The acquisition can take place on the optical stage equipped with 3 objectives with different magnification (20X, 40X, 100X), or on the AFM stage through an optical path chosen with a mirror system. The same objective recollects the reflected laser beam and guides it to the spectrometer. In this path is present an edge filter which introduces a cutoff frequency, removing the intense Rayleigh component, which could damage the CCD camera. This edge filter is low pass filter, therefore Anti-Stokes lines are eliminated and cannot be analyzed. The laser beam passes through a polarizer and us focused with an objective. The beam dispersion is controlled by a pinhole. The choice of the pinhole dimension is a compromise between resolution and intensity. The light then enters the spectrograph where it is diffracted. The system is equipped with 4 gratings: 1800/500, 600/600, 150/600, 75/echelle [1]. After diffraction, the light reaches the CCD sensor. The latter is a Andor EM CCD with 1600 pixels as lateral dimension. The sensor is kept at -60°C.

3.3.2. Spatial resolution in confocal microscopy

The maximum spatial resolution of the Raman analysis is determined by the optical diffraction limit. In optics, the Airy disk is the description of the best focused spot of light that a perfect lens with circular aperture can make. The diameter of the Airy disk depends on the light wavelength by the following expression:

$$d = \frac{1.22\lambda}{NA} \tag{3.7}$$

Where λ is the radiation wavelength and NA is the objective numerical aperture. The Rayleigh criterion establishes a reference to characterize the spatial resolution of an optical device: the minimum resolvable distance between two points [55]. The criterion is satisfied when the central maximum of the Airy disk of one point falls below the first minimum of the second point, as shown in **Figure 3.9**. The lateral resolution is then determined by the following formula:

$$R_l = \frac{0.61\lambda}{NA} \tag{3.8}$$

From a technical point of view the size of the confocal pinhole PH (μm) is related to R_l by the following equation:

$$PH = 2R_lM \tag{3.9}$$

Where M is the optical system magnification.

---

[1] The first number represents the line density (1/mm) while the second is the blaze wavelength, which is the wavelength where the grating is most efficient. "Echelle" means the spectral range and dispersion depends on the incoming light.

Another important parameter is the Axial resolution. The resolution in the Z direction depends on the medium refractive index n and is given by the following expression [55]:

$$R_{axial} = \frac{0.88\lambda}{n - \sqrt{n^2 - (NA)^2}} \tag{3.10}$$

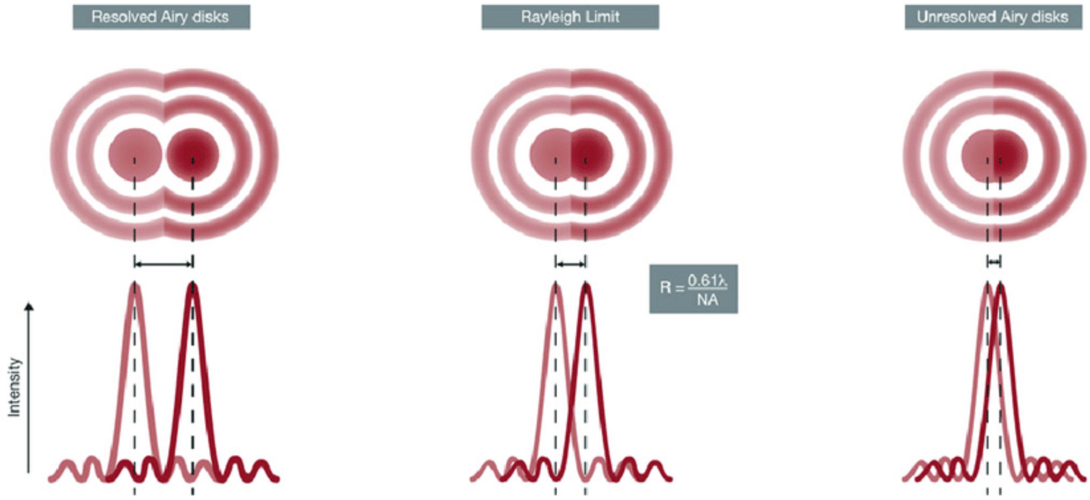

Figure 3.9: Rayleigh criterion for lateral resolution

Considering the Confotec NR500 Raman spectrometer laser sources and the refractive index of HOPG (n = 2.7) the diffraction limits of Rayleigh criterion are summarized in **Table 3.1**. The lateral limit is the order of 0.5 μm, which is the pixel spacing chosen for all the statistical analysis in this thesis work, conducted with the green laser ($R_l^{532} = 0.33$). The axial resolution is in the order of 5 μm, therefore we can assume that the focus of the laser beam remains $\sim$ constant during the Raman measure, since the HOPG roughness is in the order of the 100s of nm for the selected Raman map sizes ($\leq$ 10x10 μm).

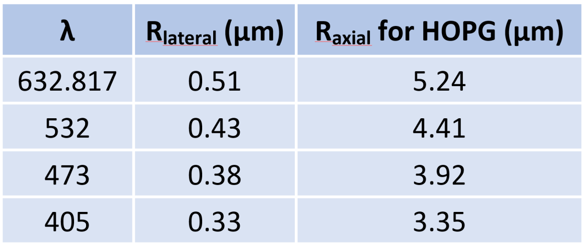

λ	$R_{lateral}$ (µm)	R_{axial} for HOPG (µm)
632.817	0.51	5.24
532	0.43	4.41
473	0.38	3.92
405	0.33	3.35

Table 3.1: Rayleigh criterion of minimum lateral and axial resolution for the spectrometer laser sources

3.3.3. Combined AFM-Raman technique

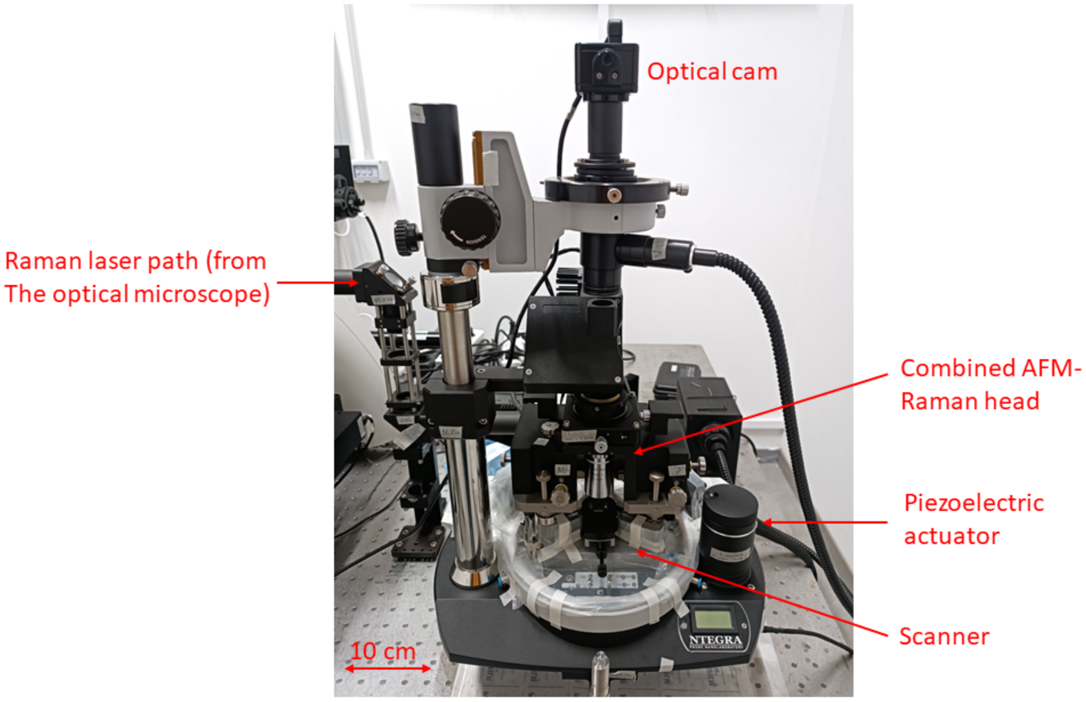

Figure 3.10: NT-MDT AFM microscope

The NT-MDT microscope (**Figure 3.10**) is a sample-scan AFM: the tip is fixed and the sample is positioned over a scanner that moves during acquisition. This configuration allows for a wide range, with a maximum image size of 100x100 μm. The tradeoff is a decrease in image quality when then sample is very heavy, for example when it is immersed in the electrochemical cell. This configuration is useful for the combined Raman measurement, since it is possible to obtain Raman maps without moving the laser beam during the scanning. The AFM+Raman in air head is equipped with a 100X objective (NA = 0.75) while the AFM+Raman in liquid head presents a 60X objective (NA = 1). The instrumentation includes also a lamp and a CCD camera, useful to observe the sample and for laser allignement.

To perform the combined AFM-Raman measurements a peculiar tip geometry is used, as sketched in **Figure 3.11**. The tip edge is inclined and it is therefore possibile to focus the laser beam adjacent to the tip apex [13].

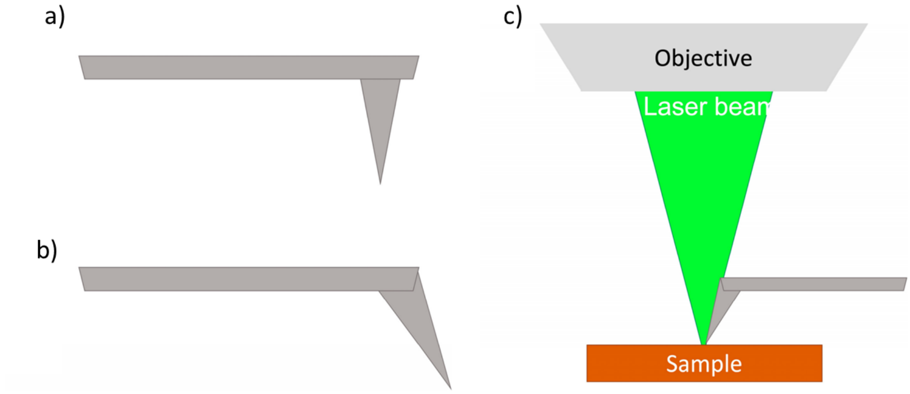

Figure 3.11: Sketch of a) the usual tip geometry, b) the special tip geometry optimized to acquire the Raman-AFM combined measurement c) axial coupling between the Raman system and the AFM setup, which highlights the special tip [13].

The special geometry of the tip can be observed with the optical microscope, which is used to perform a first manual alignment of the laser, as show in Figure 3.12. The terminal part of the tip is made of silicon and can be used for Raman calibration, while the cantilever is coated with Au (yellow area). The AFM infrared laser is visible as a purple shadow on the cantilever, thus the alignment can be optically verified. The Raman laser spot (green) can be moved through a piezoelectric activated mirror system and thus aligned on the tip apex . The tip is easy to find since the scattered light produces a shadow on the tip as it can be seen in **Figure 3.12**. This mirror system can also be used to scan, there are therefore two Raman map acquisition modes: mirror-driven (the laser moves) and scanner-driven (the sample moves).

After optical alignment a fine tuning alignment is made by a quick mirror-driven scansion of a region where we expect the tip. The apex is found as a hotspot in the silicon peak region of the Raman map, and then the laser is aligned 2-3 μm below the tip (to avoid any Si contribution in the Raman spectrum), with a precision of around 1 μm,in the order of the diffraction limit of the laser, as shown in **Figure 3.13**. The subsequent Raman maps are instead acquired in scanner-driven mode so that tip and laser remain aligned.

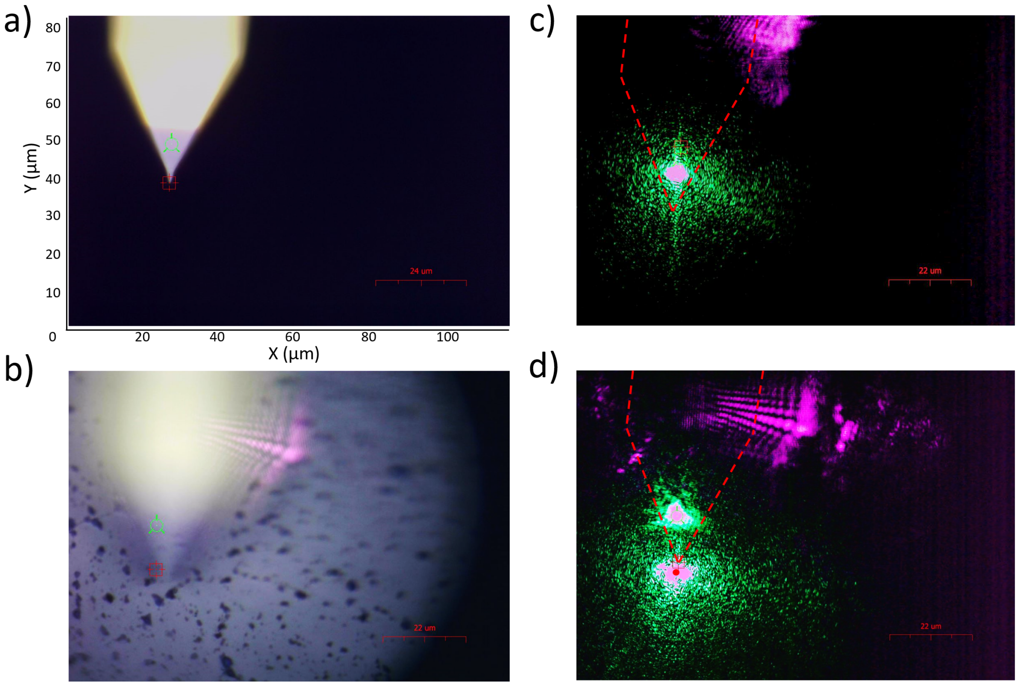

Figure 3.12: Optical microscope images of a) focus on the tip far from the sample b) focus on an intercalated HOPG sample c) laser spot on the silicon part of the tip (used for calibration) d) laser spot on HOPG alligned on the tip apex.

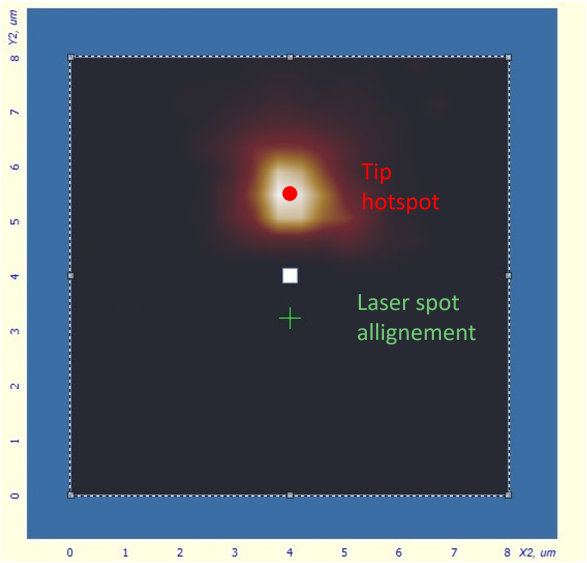

Figure 3.13: 8x8 μm mirror-driven Raman map of the Si peak at 520.7 cm^{-1}, showing a sharp hotspot in intensity in the central region (red dot). Fine alignment of the laser is then possible by moving the laser spot (green cross). Fairly large distances of $2/3$ μm where chosen for precaution.

3.3.4. Electrochemical setup

The electrochemical cells used for the measurement are made of Teflon. The cells have circular geometry and can be positioned on the AFM scanner with a magnetic plate. **Figure 3.14** shows the setup. The sample is connected to a copper working electrode on the non exposed surface, while the counter electrode (CE, made of a Pt wire) is bent to turn around the cell (not visible in Figure 2b) to have an isotropic configuration. The RE is a Pt quasi-reference (PtQRef) elecrode.

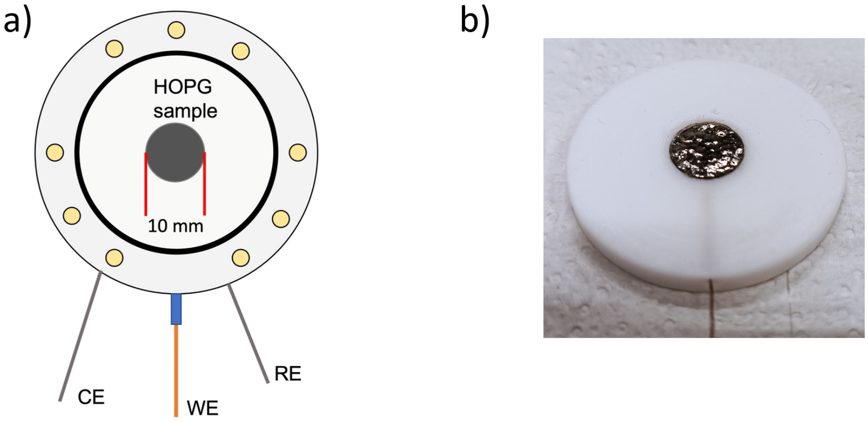

Figure 3.14: a) scheme of EC cells employed to perform the CVs on the HOPG samples b) pristine HOPG sample connected to the W.E. [15].

The system is equipped with a potentiostat which can be used to perform in-situ and in-operando electrochemistry. For the statistical AFM+Raman in air analysis I however employed an external potentiostat, which allows a better control of the process and prevents the unnecessary exposure of the AFM system to the acid solution.

3.4. Sample preparation and acquisition parameters

Preliminary analysis were conducted to identify the best electrochemical, Raman and AFM procedures and parameters to characterize the intercalated HOPG samples, a detailed review of these studies is presented in Appendix A.

Optical-stage Raman spectroscopy and AFM analysis where carried out on freshly exfoliated ZYH mosaic spread (3.5° ± 1.5°) HOPG samples subjected to 1, 2 and 4 CV cycles in 1M H_2SO4 solution purified by Argon bubbling for several hours. 2CVs samples were identified as the best choice for the statistical analysis.

All CVs followed the same standard parameters choice, determined in previous literature [4, 6, 8, 13, 56]: $V^i_{EC} = 0.2$V, $V^f_{EC} = 1.3$V, $v_{scanrate} = 25mV/s$ (STD cycle). Typical maximum current densities J for HOPG samples where in the order 5-15 $\mu A/mm^2$ for all preparations. The CVs show the characteristic intercalation figures in the forward sweep 1-1.3 V region, as well as oxigen evolution starting at approximately 0.9 V. Deintercalation figures around 1.1 V reverse sweep region are also present, in agreement with literature [6, 7, 15].**Figure 3.15** shows an example of 2CVs cicles.

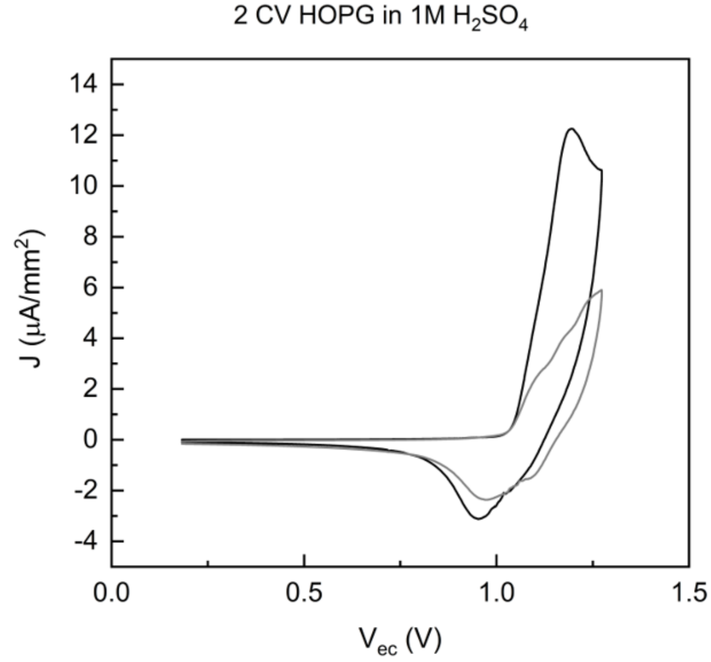

Figure 3.15: J-V voltammogram, 2CV STD cycles on HOPG in 1M H_2SO_4.

Sample washing with ultra-pure H_2O after intercalation was carried out as it was found that there is no alteration of the Raman spectrum, while some precipitates that are deposited from the acid solution are removed, leaving a cleaner sample at both optical and AFM view. Comparative analysis between 633, 532 and 473 nm laser sources identified the 532 nm green laser as the best choice (See Appendix A).

All measures where conducted with 600/600 grating and central pixel at 590 nm, which for 532 nm excitation permits a spectral range of 630-2940 cm^{-1}. Above a critical power the G_i peak shows a irreversible decrease and the sample is therefore altered in a permanent way. 2.5 mW (ND filter at AFM = 0.6) was the highest employed power, chosen to optimize the Raman maps acquisition time and avoid sample damage (See Appendix A).

4 | Results

This chapter describes the statistical analysis which I conducted on HOPG blisters with the combined AFM+Raman in air technique. Previous literature works showed that blisters are stable for several days and precipitates that appear after drying the sample do not alter the Raman spectrum [4, 8, 15, 56]. I however re-exfoliated and EC prepared (see Section 3.4) the samples every two days to ensure a meaningful statistical distribution and avoid possible aging effects. The Raman spectra were acquired through Raman mapping of selected regions. The alignment with the AFM scans was checked by the analysis of spectral features correlated with the morphology, and spectra representative of the swelled region and of the surrounding HOPG basal plane were extracted for each blister (see Appendix B). A total of 25 blister was analyzed with combined AFM-Raman measures.

4.1. Experimental procedure

AFM was performed in non-contact mode. I first acquired 40x40 μm exploratory scansions. Blisters with diameter > 2 μm were chosen for the combined analysis, to be largely above the laser diffraction limit and obtain "pure" blister spectra. These blisters have a density of around 3-4/40x40 scan for 2CVs intercalated HOPG samples. I then made detail 15x15 and 10x10 μm scans on selected individual blisters, followed by Raman maps of 10x10, 8x8 and 6x6 μm of the same regions ($px_{size} = 0.5$ μm, $t_{acq} = 7.5$ s, $n_{acq} = 2$). The experimental procedure can be summarized as:

1. HOPG mechanical exfoliation and EC cell preparation
2. Electrochemical process in 1M H_2SO_4
3. Washing with ultra pure H_2O and drying (1 day) of the sample
4. Exploratory AFM scan
5. Detail AFM scan on individual blisters
6. Raman map on the same region

4.2. AFM of intercalated HOPG

Figure 4.1 is exploratory a 40x40 μm scansion that shows the general morphology of intercalated HOPG in air. The HOPG basal plane is still clearly visible and diagonal steps of few nanometers of height are appreciable. The surface presents diffuse blistering and some residual precipitates not eliminated by the sample wash, with heights of a few hundred nanometers.

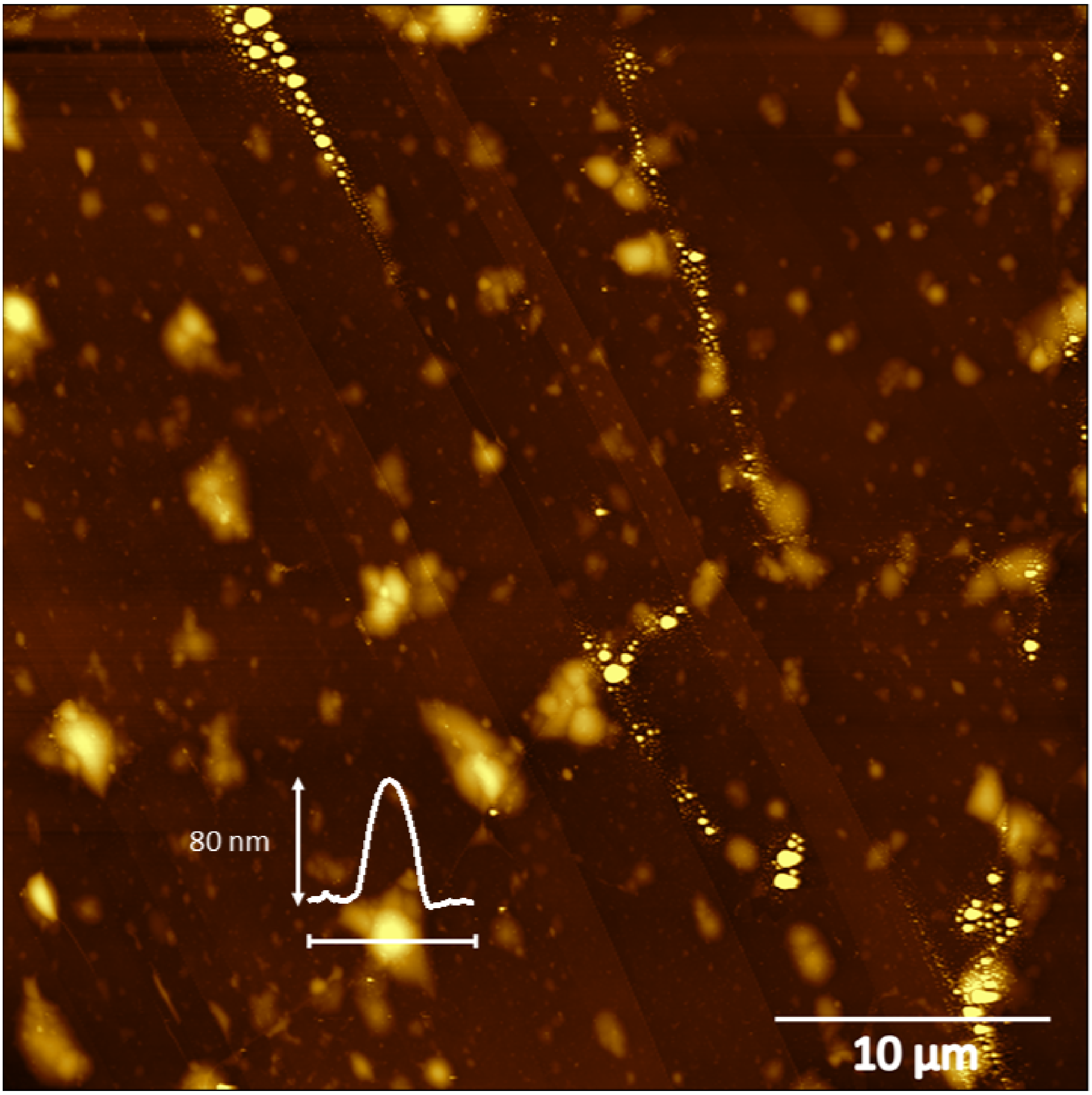

Figure 4.1: 40x40 μm AFM image of HOPG post 2CV. The profile highlights a blister of ~ 1.5 μm radius and 80 nm height. It is possible to appreciate the HOPG basal plane as well as several precipitates.

From these exploratory scans I selected the most suitable blisters to analyze. The detail 15x15 or 10x10 μm AFM image was used to extract the main morphological features of the blister: average radius (as a mean of maximum and minimum radius) and height. **Figure 4.2** shows a detail 10x10 μm AFM scansion on a selected blister and the sections used to extract the parameters: average radius $R = 1.6\ \mu m$, average height from the basal plane $h = 125$ nm.

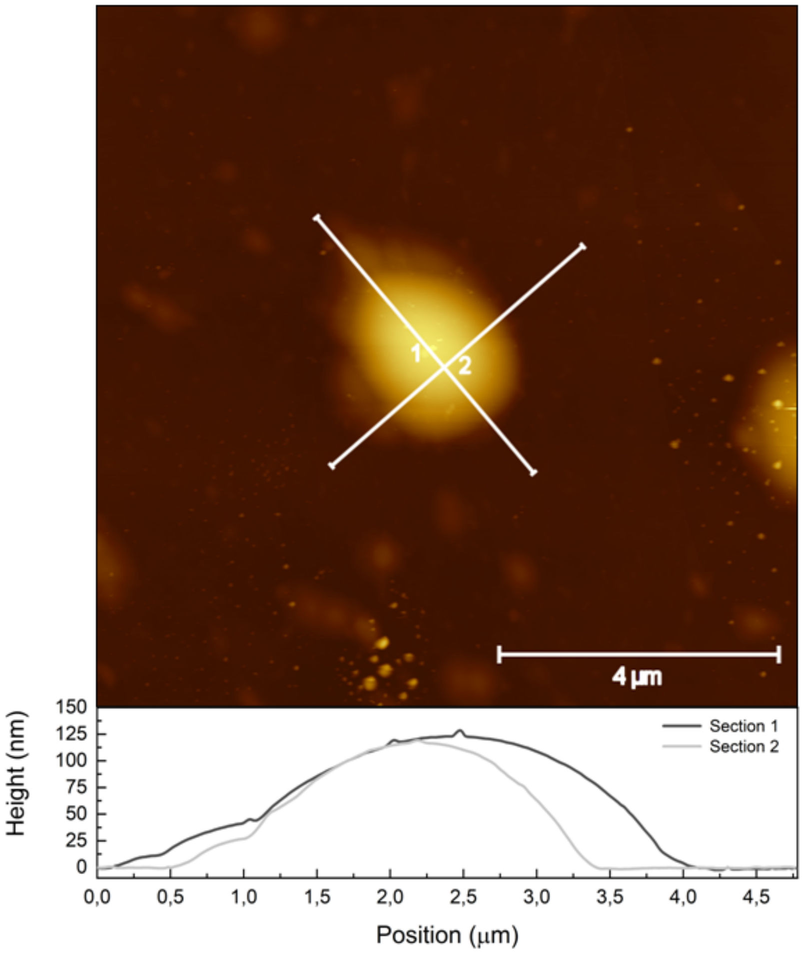

Figure 4.2: 10x10 μm AFM of a blister and extracted profiles.

A summary of all the extracted morphological features is reported in the next chapter (see Table 5.3). The mean blister radius and height from the analyzed distribution are $R_m = 1.6\ \mu m$, $h_m = 80 nm$.

4.3. Raman maps

Raman maps on the selected blisters were performed after laser alignment. Raman mapping is a technique which consist in the acquisition of many individual spectra on a grid of points. For all the measurements point-spacing was fixed at 0.53 μm, while the total map size (and therefore the number of points) was varied. The most evident feature present in all the measures is a sharp enhancement of the G peak on swelled structures. **Figure 4.3** plots the absolute intensity spectra of a blister (black line) and of the intercalated HOPG basal plane (red line). On the blister the G peak is around 3.5 times more intense than in the surrounding HOPG.

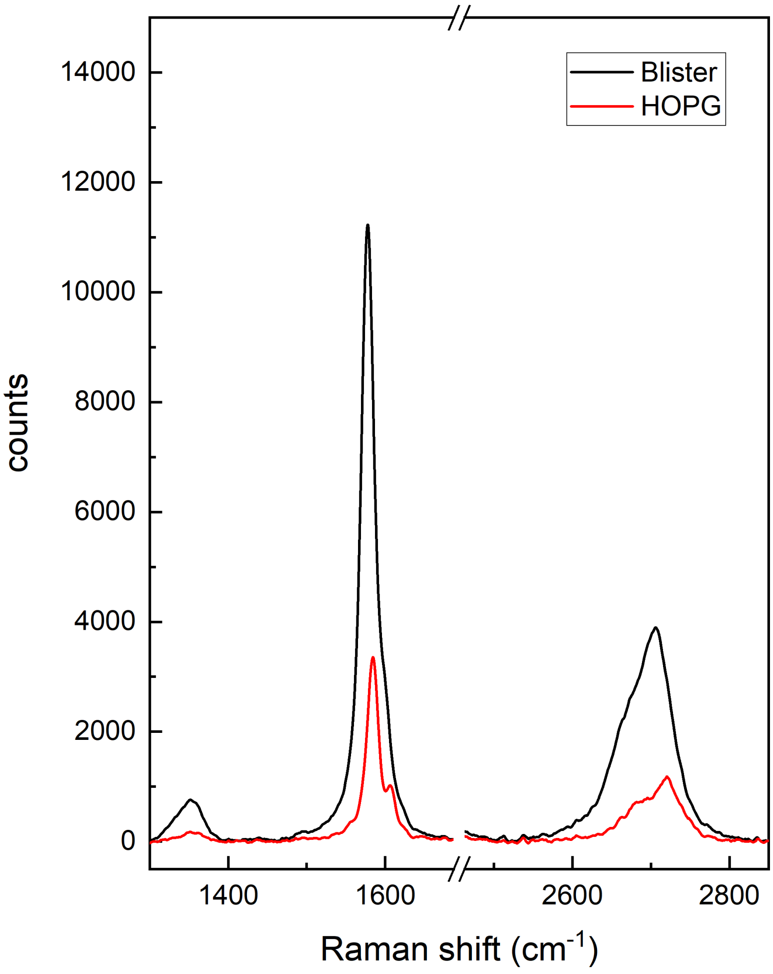

Figure 4.3: a) absolute intensity spectrum of a blister (black) and of the surrounding intercalated HOPG basal plane (red).

4.3.1. Intensity maps and alignment with AFM

This enhancement can be visualized with a Raman map of the whole analyzed region, obtained by extracting the maximum intensity value in a spectral range around the expected 1582 cm^{-1} position for the G peak of each spectra (each point of the map). The result is a *Raman intensity map*, as the one shown in **Figure 4.4**:

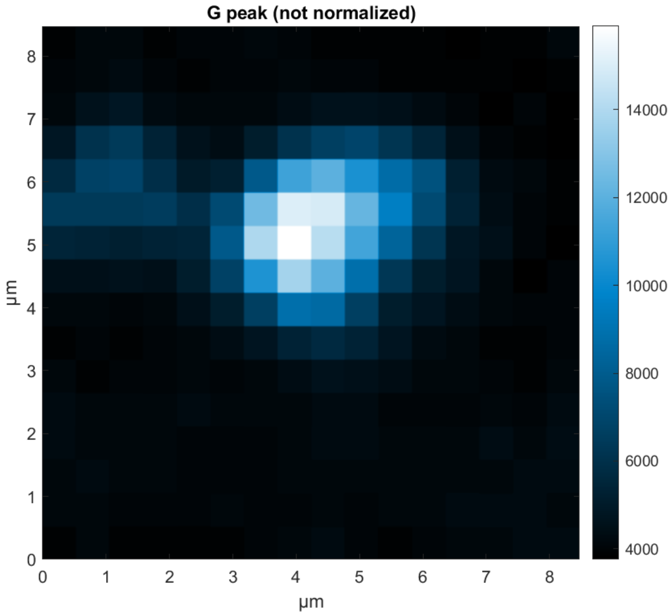

Figure 4.4: Raman intensity map of the G peak.

$I_G^{blister}/I_G^{HOPG}$ intensity ratios vary between 1.8 and 4.9 (mean enhancement 3.5). This spectral feature was used to check the correlation of the Raman maps with the AFM morphology. **Figure 4.5** shows the superposition of G intensity maps with a 40x40 exploratory scan. It is evident from this figure that the spectral feature is directly correlated with the AFM morphology and in particular with swelled structures. **Figure 4.6** shows the alignment of a 8x8 μm Raman map (in transparency) on a detail 10x10 μm AFM scan of a blister. The alignment was also independently verified with D peak maps on disordered carbon structures recognized on some of the AFM images. Mis-alignments were in the order the Rayleigh diffraction limit ($< 1\ \mu m$) in all measurements. After checking the alignment, points representative of the blister spectrum were chosen, as exemplified by the yellow square in Figure 4.6. Three random points in flat AFM areas were also selected to obtain a mean representative spectrum of the HOPG basal plane.

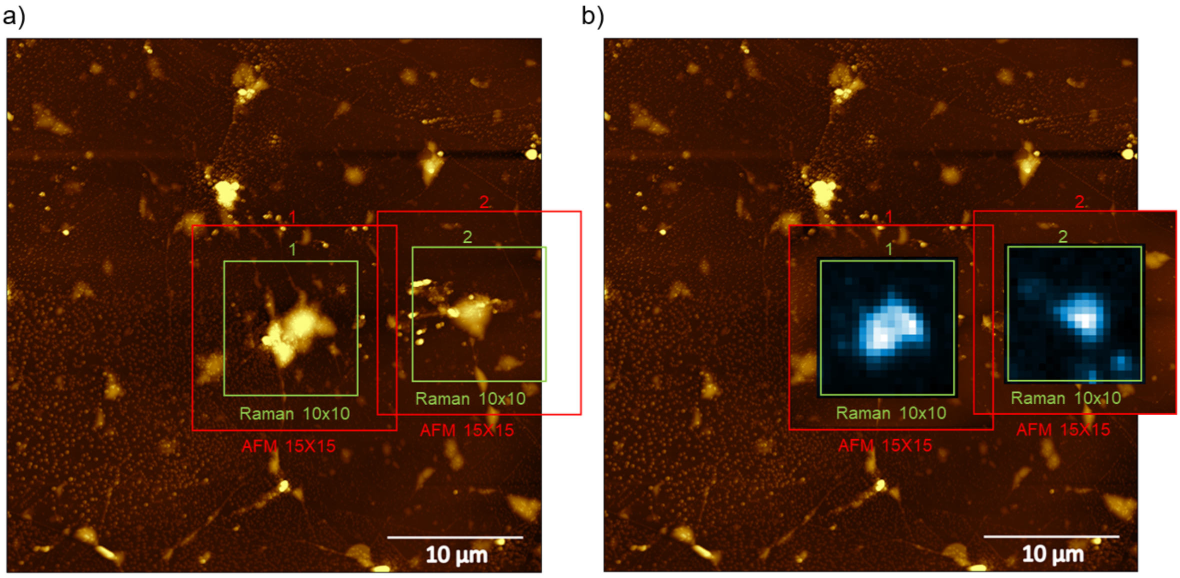

Figure 4.5: a) 40x40 μm explorative scan with the selected regions for the combined measures b) 10x10 μm Raman maps of the G peak absolute intensity (20x20 px, 532 nm, 7.5s x 2acq., 2.5mW).

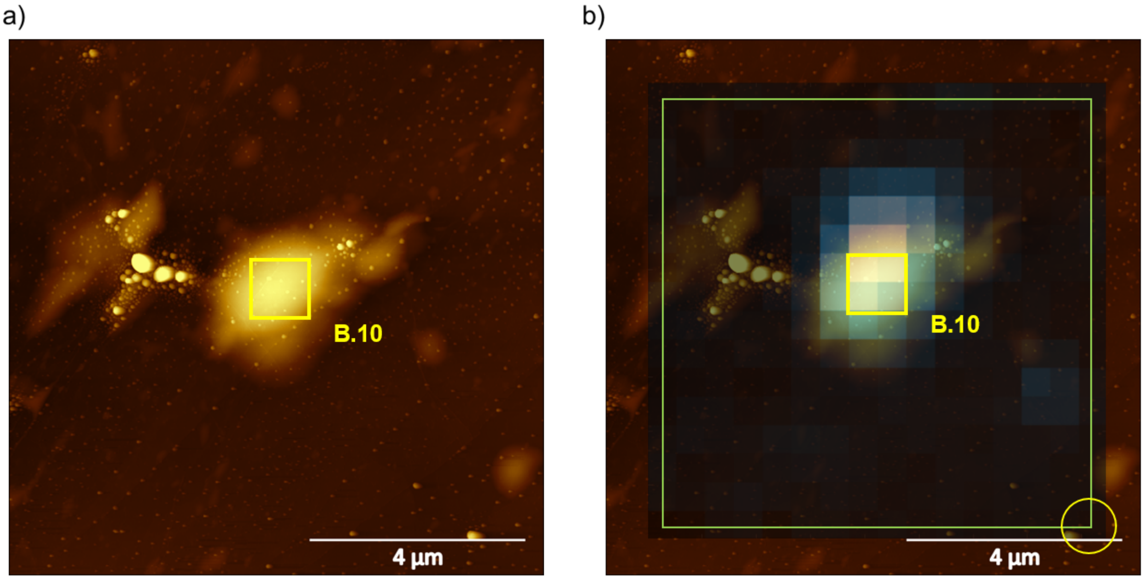

Figure 4.6: a) detail 10x10 μm AFM scan of a selected blister and b) 8x8 μm Raman map of the same region, with in transparency the AFM morphology. The yellow circle represent the Rayleigh diffraction limit. The yellow square refers to the points chosen as representative of the blister spectra.

From the raw data it is possible to extract other maps on selected spectral ranges. All the data was normalized to the G peak absolute intensity of each point. **Figure 4.7** shows the extracted maps of the G peak absolute intensity (blue, $\sim 1582 cm^{-1}$); the G_i intercalation peak (green, $\sim 1610\ cm^{-1}$), the D peak (yellow, $\sim 1350 cm^{-1}$); the 2D band components $2D_1$ and $2D_2$ (red, $\sim 2686\ cm^{-1}$ and $\sim 2720\ cm^{-1}$) and their ratio $2D_1/2D_2$. All these maps show the peaks relative intensity compared to the G peak (normalized spectra). As appreciable in Figure 4.7, the G peak enhancement and the change in the 2D peak components ratio are the two distinctive intensity features of the blister, while the G_i and D peaks are rather uniform on the whole map.

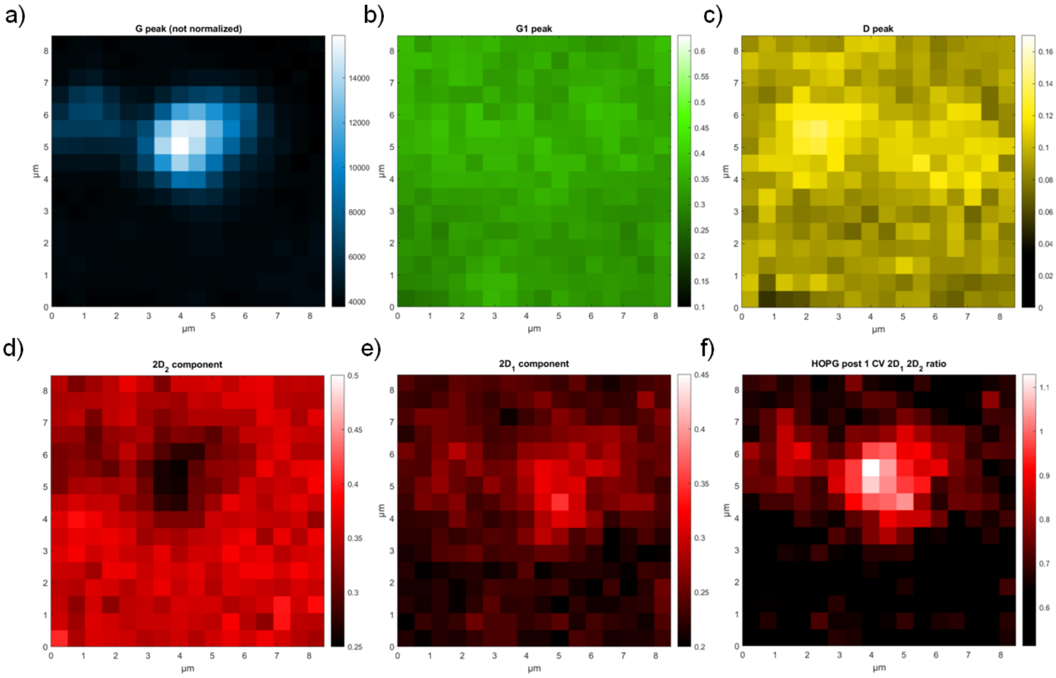

Figure 4.7: Blister maps of a) G absolute intensity b) G_i relative intensity c) D peak relative intensity d,e) $2D_1$, $2D_2$ relative intensity and f) $2D_1/2D_2$ ratio.

4.3.2. Raman shift maps

Another interesting feature which was observed in blister spectra and not in the HOPG basal plane regions is the G peak downshift (at lower cm^{-1} compared to both pristine HOPG and intercalated HOPG basal plane). The position of the peak can also be extracted from the data obtaining *Raman shift maps*, which help to intutively visualize the feature. **Figure 4.8** shows the Raman shift map of the G peak, i.e. the position of the maximum intensity spectral point, of the blister (same blister of Figure 4.6 and Figure 4.7).

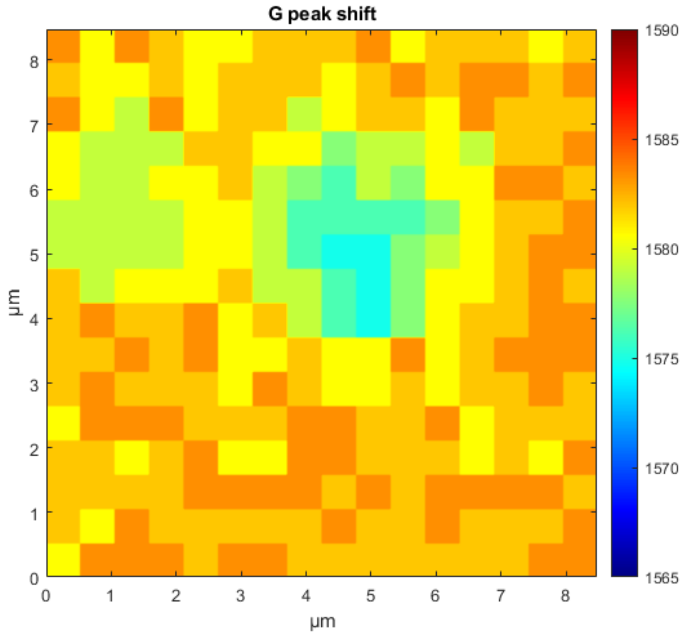

Figure 4.8: G peak Raman shift map, the scale is cm^{-1}. The G peak presents a downshift on the blister at about 1575 cm^{-1}.

The majority of the analyzed blisters have spectra comparable to the reported example, with a G downshift from 2 up to 17 cm^{-1} (see Table 5.3 in the next chapter). This effect seems to extend also in the first $\sim 1\mu m$ of the HOPG basal plane surrounding blisters.

4.4. Blister spectra

As mentioned before, from all this data I selected points representative of the blister spectrum (see Figure 4.6), as well as 3 random points, representative of the intercalated HOPG basal plane. All spectra were normalized with a Lorentzian fit of the G peak with, G_i component if present (see Section 5.2). **Figure 4.9** shows both not-normalized and normalized spectra for the same blister of previous figures. It is possible to appreciate the G peak enhancement on the blister ($I_G^{blister}/I_G^{HOPG} = 4.29$), and a slight downshift of the $G^{blister}$ (at 1576 cm^{-1}). The blister spectrum shows also a more consistent D peak and a downshifted and broader 2D peak, with a higher relative intensity of the $2D_1$ shoulder compared to intercalated HOPG. The peak however still presents clearly the 2 components with a "graphitic" shape in most spectra (see appendix B).

The D peak is present in the majority of blisters, slightly enhanced in relative intensity compared to the HOPG basal plane (mean $I_D^{blister} = 0,06$ mean $I_D^{HOPG} = 0,03$).

These values are relatively low (only one blister presented an unusually high D peak of rel. intensity 0,19).The intercalation peak G_i is present in all of the maps and its relative intensity is not correlated to the presence of blisters (mean $I_{G_i}^{blister} = 0,33$; mean $I_{G_i}^{HOPG} = 0,27$). In some of the measures the G_i peak is not clearly resolved but appears as a shoulder of the G peak for both HOPG and blisters.

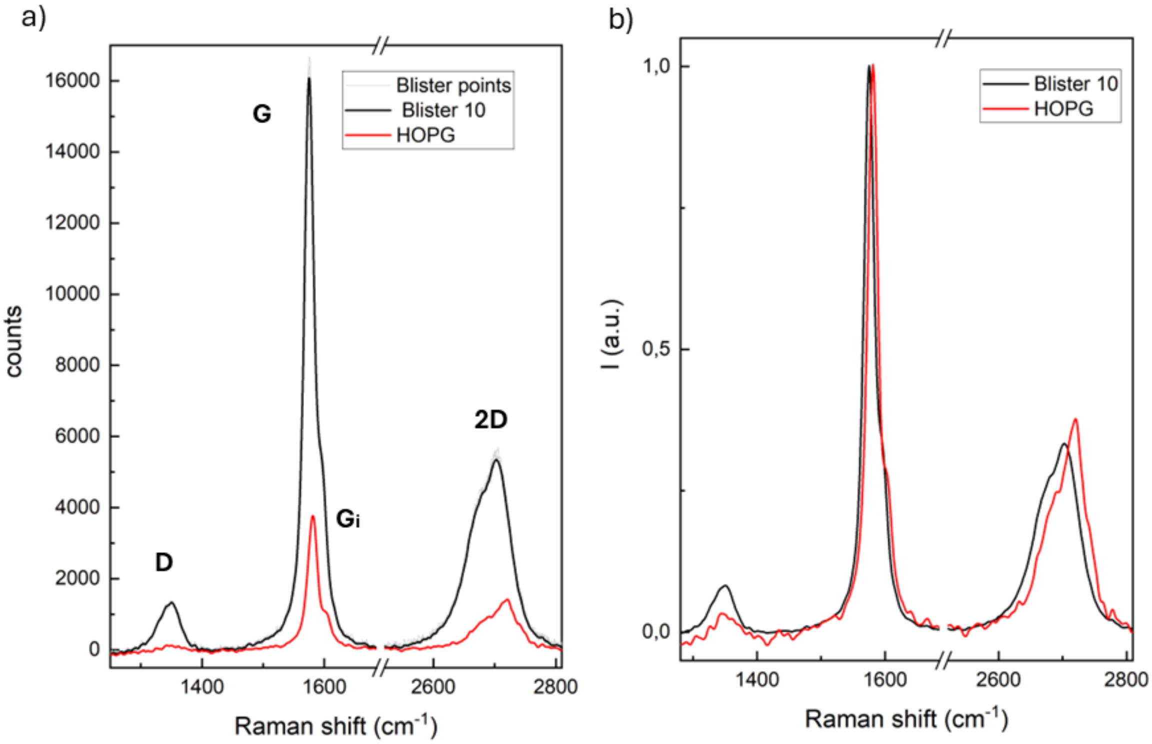

Figure 4.9: a) not normalized and b) normalized spectrum of a blister and of the surrounding intercalated HOPG basal plane.

4.4.1. Anomalous double G peak blisters

Three blisters with particularly high h/R morphology (see Table 5.3 in the next chapter) presented a G peak made of 2 components: one at $\sim 1582\ cm^{-1}$ and one at 1565-1570 cm^{-1}. These blisters present also a significantly modified 2D peak lineshape, with a broad single component at $\sim 2675\ cm^{-1}$ and a shoulder at 2720 cm^{-1}, around the expected $2D_2$ Raman shift for HOPG. One example of these particular blisters is shown in **Figure 4.10** (AFM and Raman maps) and **Figure 4.11** (Raman spectrum compared with basal plane). These features where at first quite puzzling as it was not clear what caused the G splitting in these anomalous blisters. A detailed discussion of these interesting results is found in subsection 5.4.3 of the next Chapter.

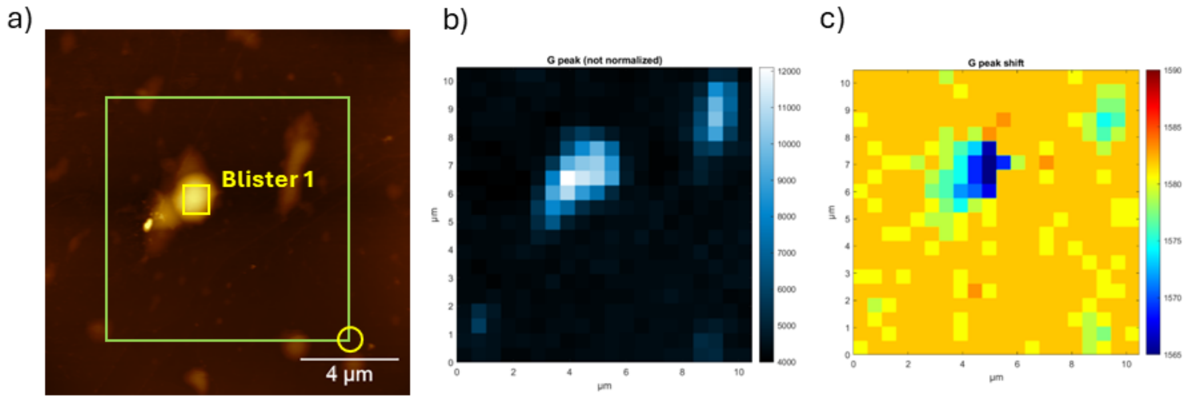

Figure 4.10: a) 15x15 μm AFM image of a blister ($h = 118nm$, $R_{mean} = 1.43\mu m$) b) 10x10 μm G intensity map c) G peak position map.

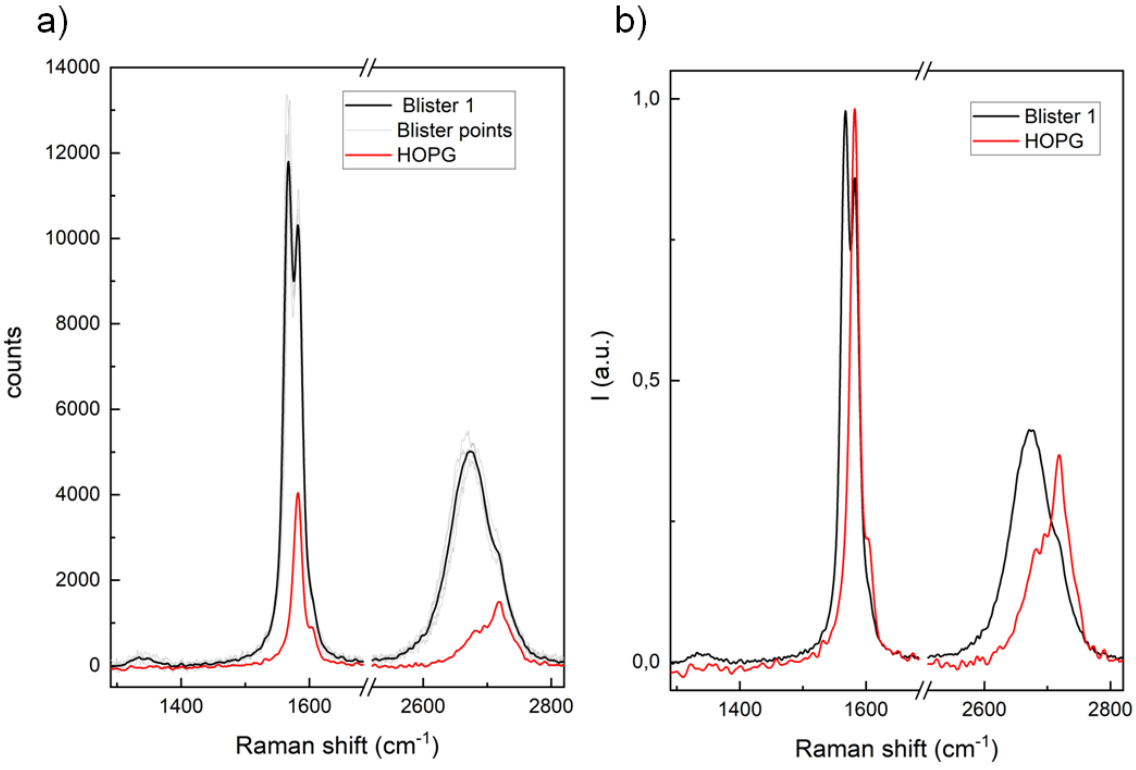

Figure 4.11: a) not normalized and b) normalized Raman spectrum of the anomalous blister of Figure 4.10 and of the intercalated HOPG basal plane. The G peak is double in this blister: one component at 1582 and one at 1565 cm^{-1}.

5 | Data analysis and discussion

In this chapter I will present the main results of the statistical analysis on HOPG blisters. The system is complex and different phenomena are coupled togheter: Raman spectra reveal a lot of information which must be carefully analyzed to avoid misinterpretations. The main causes that modify the HOPG spectrum are:

1. Intercalation effects on the interplanar distance (G_i peak)
2. Intercalation effects on the carbon bond order (HOPG damaging, D peak)
3. Strain effects and elastic deformation of the blister skin, due to the internal pressure.
4. Thin-skin effects on blisters, due to the change in the electronic bands as we approach the single layer configuration.

The first two effects are characteristic of the whole HOPG basal plane, while the others are strictly linked to the swelled regions. These effects were independently studied in literature, either in controlled systems (e.g. strain in mono/bilayer graphene artificially inflated bubbles) or without a microscopic local approach (e.g. average Raman intercalation studies on HOPG). A detailed review of these results is present in Chapter 2. The main scope of this thesis work is to try to decouple and evaluate as much as possible the effects in order to understand and quantify the causes of the spectral modifications on blisters compared to the intercalated basal plane, and to correlate these effects with the AFM morphological information. The following discussion will show the impressive potential of the combined technique in the study of a complex nanostructured system, as well as its current limitions.

5.1. Raman spectra

A total of 25 blisters were analyzed with combined measurements. Two of them were excluded from the discussion because of their complexity, leaving a statistic of 23 blisters. As shown in the previous Chapter, blisters present in most cases comparable spectra, with a 2D band where is still possible to identify two components $2D_1$ and $2D_2$, as for intercalated HOPG. Three "anomalous" blisters showed however a G peak made of 2 components and a significantly different 2D band lineshape, with a component around $\sim 2670cm^{-1}$ and a shoulder of about half the height at $(\sim 2720cm^-1)$.

These blisters required special fitting and analysis. I will refer in all the discussion as "normal blister" for the first type (20 analyzed b.) and "anomalous blisters" for the latter double G peak type (highlighted in violet in all Tables). **Figure 5.1** shows examples of a) a normal and b) an anomalous blister spectra (black lines). The intercalated HOPG spectra are also reported (red lines) as well as the single points spectra used to obtain the average representative of the blister (light grey lines).

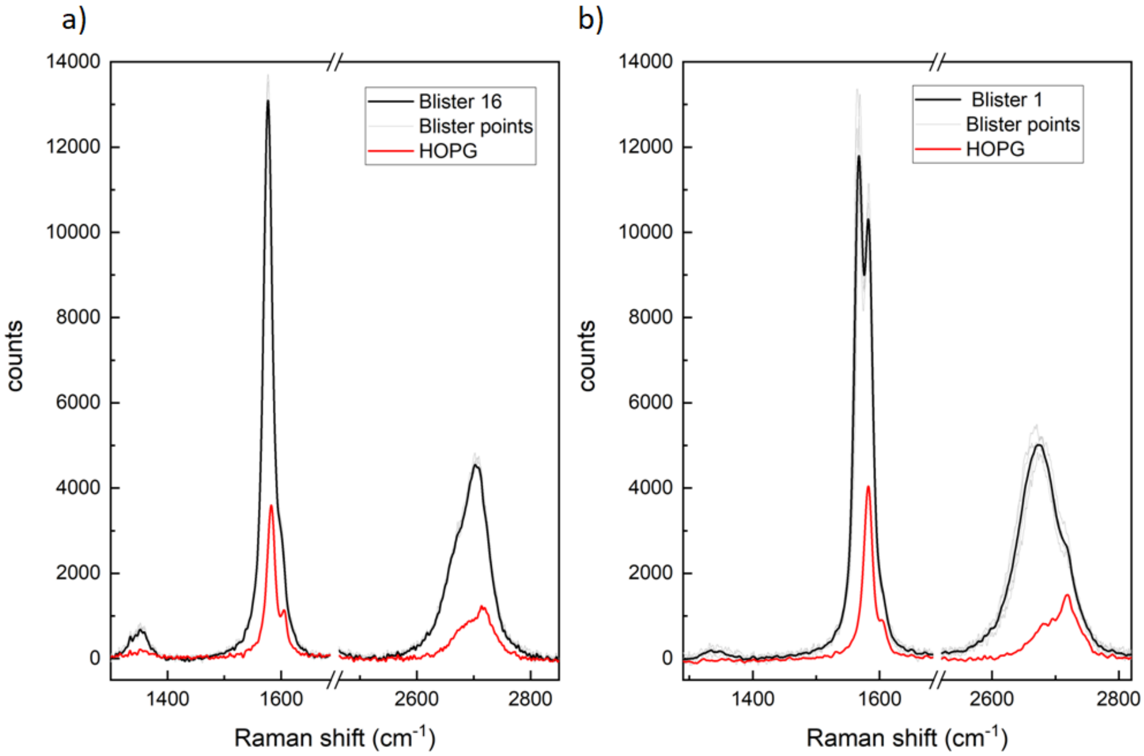

Figure 5.1: a) normal blister with a single G component and a "graphitic" 2D peak b) anomalous blister with G peak made of 2 components and different 2D lineshape. HOPG surrounding the blister is also plotted.

5.2. Peaks fitting

To normalize the spectra and obtain intensity and position values of the G peak for blisters and intercalated HOPG basal plane, I performed a Lorentzian fit of the G peak. A constant background was removed from all spectra before fitting. For blisters with significant G_i peak, I employed a 2 components fit. For anomalous blisters I also used a 2 components Lorentzian fit, one for the downshifted component ($1565 - 1570cm^{-1}$) and one for the unshifted one, which in all 3 blisters is around the $1582cm^{-1}$ position of HOPG.

Figure 5.3 shows the G fitting procedures of a normal and an anomalous blister (same b. of Figure 5.1): a) is a normal b. fitting with G and G_i components, while b) is an anomalous b. fit, with two components at 1565 and 1582 cm^{-1}.

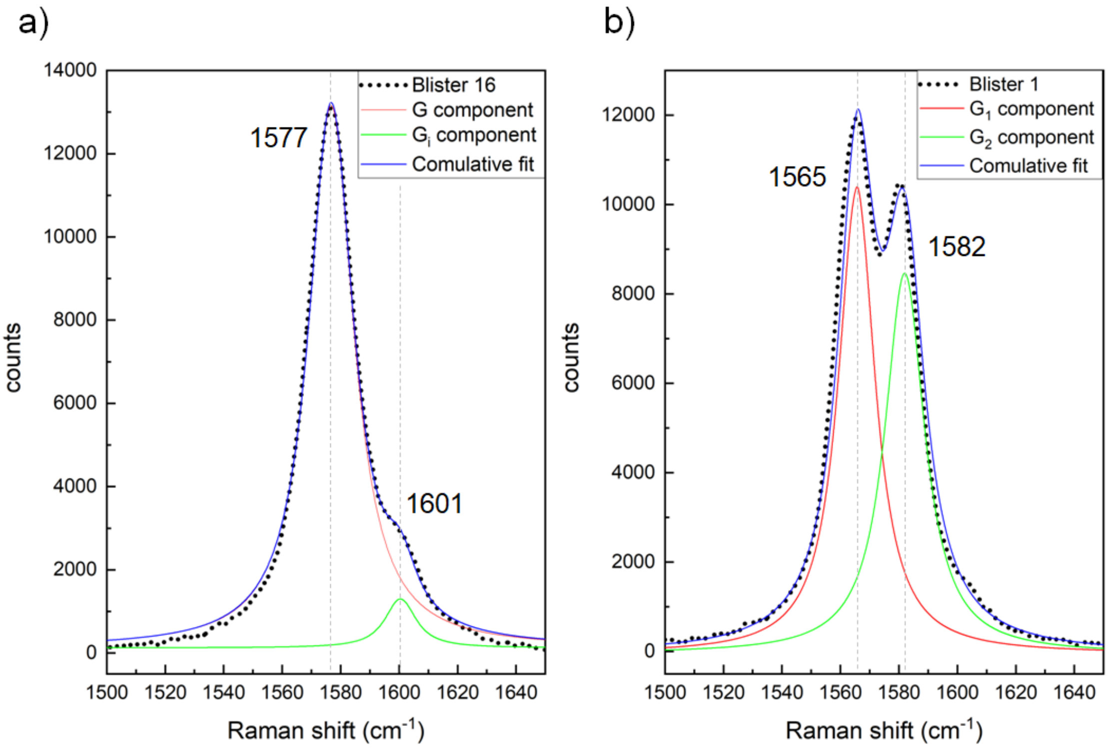

Figure 5.2: a) normal blister fitting with G and G_i components b) anomalous blister fitting with 2 components for the G peak.

For the 2D band fit I instead employed Voigt functions, which are a combination of Lorentzian and Gaussian functions. This approach permits a more faithful reproduction of the band lineshape compared to a simple Lorentzian fit, which was also considered. All single G peak blister 2D bands were fitted fitted with 2 components, $2D_1$ AND $2D_2$, as for intercalated HOPG. Double G peak blisters (heavily shifted) presented difficulties, since it was not clear how to interpret the broad 2D band. For this first statistical analysis a single component Voigt fit was performed to obtain indicative values of shift and intensity. A more refined approach, which involves the subtraction of the underlying HOPG basal plane spectrum, is presented in section 5.4.3.

Examples of 2D fitting for a normal and an anomalous blister (same of the previous figures) are reported in **Figure 5.3**. The 2D peak presents in most blister an enhanced $2D_1$ component with respect to both pristine and intercalated HOPG, as well as a downshift of 3-20 cm^{-1} for both components from the calculated mean intercalated HOPG basal plane position values ($2D_1^{HOPG} = 2684 \pm 3\ cm^{-1}$, $2D_2^{HOPG} = 2719 \pm 1,5\ cm^{-1}$).

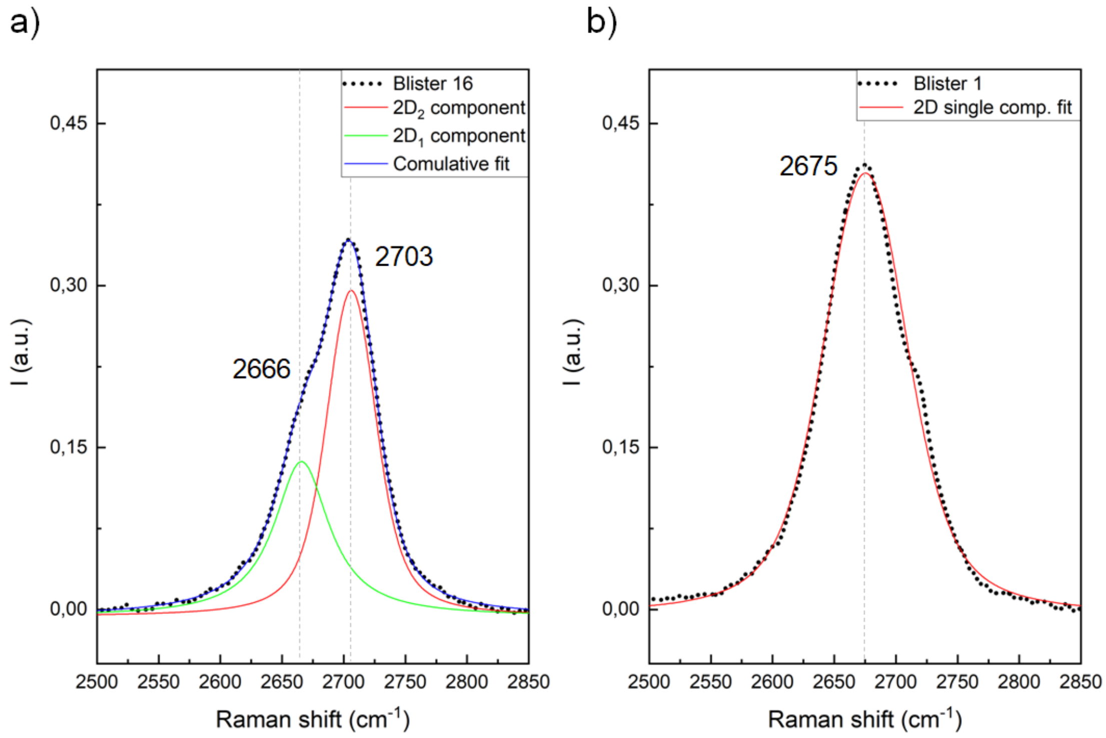

Figure 5.3: a) two component Voigt fit for a normal blister and b) single component fit of the 2D band for anomalous double G blister. Fitting parameters for these as well as all other blisters are presented in the next section.

5.3. Statistics

The most relevant data extracted from Raman measures and fits are reported in the next tables. Two blisters (11 and 23) were excluded from the statistical analysis because of their morphological and spectral complexity, leaving 23 analyzed blisters (20 normal single G b., 3 anomalous double G b.). The D peak was not fitted for simplicity, as I did not conduct a detailed analysis on its features. The D and G_i relative intensity values reported in the table are indicative and extracted directly from the normalized plots as the maximum intensity value in the region.

5.3.1. G, D and G$_i$ peaks statistics

Table 5.1 shows the results of the G peak Lorentzian fit. In the table are reported the G shift and intensity value for the blister and the comparison with the HOPG basal plane intensity of the same Raman map. The double G peak blisters are highlighted in violet: the G peak reported in this case is the downshifted one, since as it will be explained and justified in the discussion, the evidence suggest that the $\sim 1582cm^{-1}$ component is a contribution of the HOPG under the blister skin. The $I_G^{blister}/I_G^{HOPG}$ ratio, representative of the peak enhancement, is an interesting parameter and is also reported. The last columns show indicative relative intensity values of the D and G$_i$ peaks of both blisters and the HOPG b.p. of each map for completeness.

5.3.2. 2D band statistics

Table 5.2 shows instead the results of the 2D band Voigt fit of all blisters and the mean results for pristine and intercalated HOPG. From these fits values of Position (cm^{-1}) Intensity (I), subtended area (A) and full width at half maximum (FWHF) were extracted for the $2D_1$ and $2D_2$ components. Intercalated HOPG shows an upshifted position of the $2D_1$ component (2684 cm^{-1}) with respect to pristine HOPG value (2677 cm^{-1}), the $2D_1$ component in intercalated HOPG is also enhanced in both intensity and subtended area. Anomalous double G peak blister presented a heavily shifted and broad 2D band and were fitted with a single component, as exposed before. The columns for these particular blisters, highlighted in violet, are therefore merged.

Map n°	G position (cm^{-1})	I_G (counts)	$I_{G\ HOPG}$ (counts)	$I_{G\ blister}$/ $I_{G\ HOPG}$	I G_i blister (a.u.)	I G_i HOPG (a.u.)	I D Blister (a.u.)	I D_{HOPG} (a.u.)
1	1565	12167	4022	3.03	Not resolved	0.20	0.05	0
2	1578	14738	3832	3.85	G shoulder	0.25	0.02	0
3	1580	13680	3956	3.46	0.42	0.26	0.01	0
4	1580	10921	3938	2.77	0.33	0.23	0	0
5	1579	10921	3938	2.77	0.37	0.25	0	0
6	1580	10977	5780	1.90	0.43	0.32	0	0
7	1565	12738	3603	3.53	G shoulder	0.22	0.05	0
8	1579	8588	4679	1.84	0.33	0.29	0.07	0
9	1577	9817	4072	2.41	0.30	0.27	0.05	0.05
10	1576	16036	3740	4.29	G shoulder	0.28	0.08	0.03
11	Excluded because it is difficult to select representative Raman points							
12	1579	7482	3265	2.29	0.25	0.26	0.06	0.05
13	1577	10597	3031	3.50	G shoulder	G shoulder	0.12	0.05
14	1570	7206	3316	2.17	G shoulder	0.30	0.05	0.05
15	1574	14077	3293	4.27	0.42	0.35	0.09	0.03
16	1577	13243	3633	3.64	0.16	0.3	0.05	0.05
17	1577	12971	3449	3.76	0.29	0.23	0.08	0.03
18	1576	13594	3450	3.94	0.32	0.25	0.06	0.04
19	1575	12109	3248	3.73	Not resolved	G shoulder	0.05	0.02
20	1577	10554	3213	3.28	G shoulder	0.35	0.08	0.07
21	1572	14273	3269	4.37	Not resolved	0.3	0.05	0.04
22	1576	11332	3396	3.34	Not resolved	0.32	0.06	0.05
23	Excluded because of complex blister over blister AFM morphology							
24	1574	15822	3237	4.89	G shoulder	0.38	0.19	0.08
25	1577	7719	2886	2.67	0.36	G shoulder	0.06	0.06

Table 5.1: Selected relevant parameters of G, D and G_i peaks for all measurements. Anomalous blisters with double G peak are highlighted in violet, in this case G is the downshifted one.

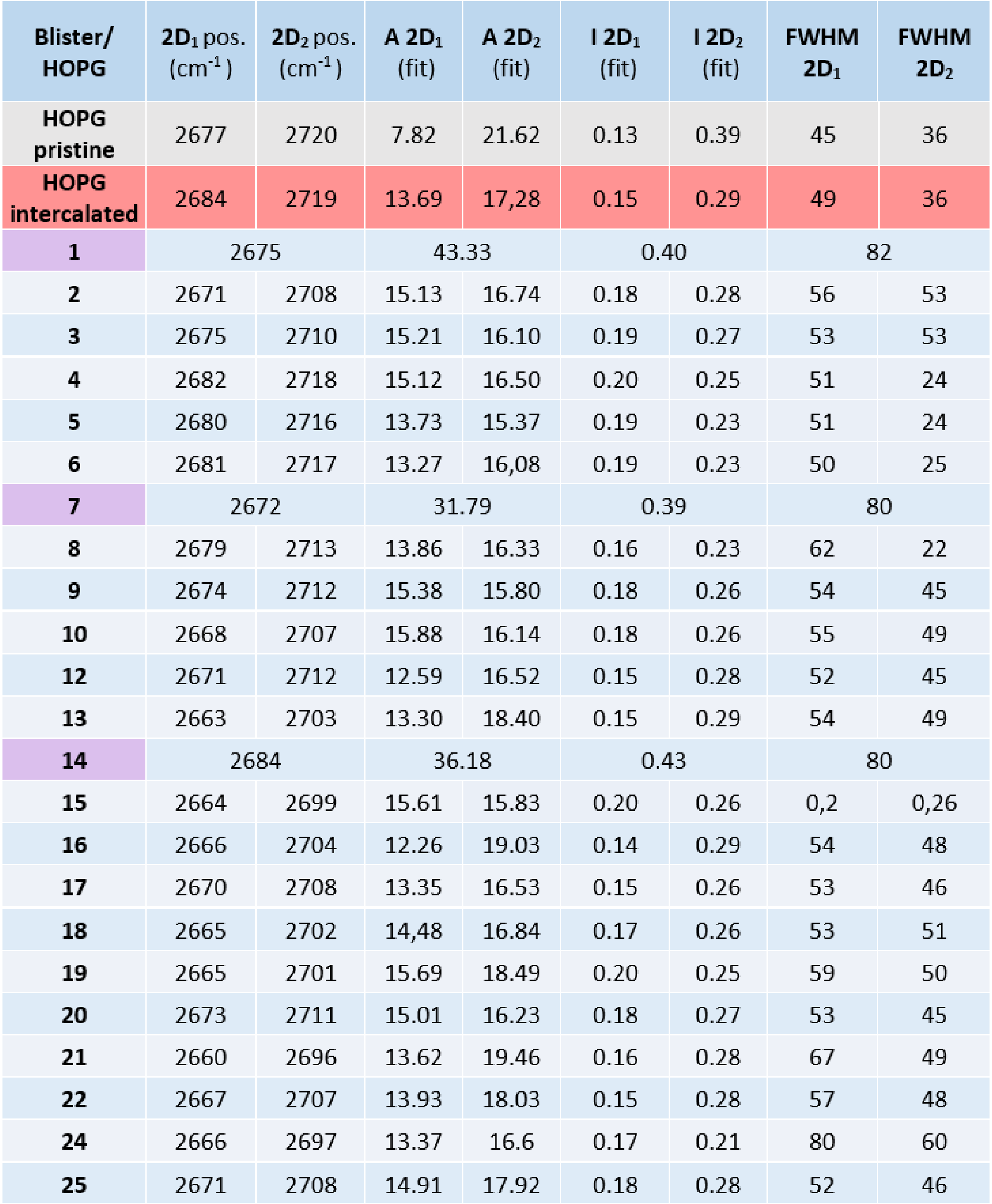

Blister/ HOPG	2D$_1$ pos. (cm^{-1})	2D$_2$ pos. (cm^{-1})	A 2D$_1$ (fit)	A 2D$_2$ (fit)	I 2D$_1$ (fit)	I 2D$_2$ (fit)	FWHM 2D$_1$	FWHM 2D$_2$
HOPG pristine	2677	2720	7.82	21.62	0.13	0.39	45	36
HOPG intercalated	2684	2719	13.69	17,28	0.15	0.29	49	36
1	2675		43.33		0.40		82	
2	2671	2708	15.13	16.74	0.18	0.28	56	53
3	2675	2710	15.21	16.10	0.19	0.27	53	53
4	2682	2718	15.12	16.50	0.20	0.25	51	24
5	2680	2716	13.73	15.37	0.19	0.23	51	24
6	2681	2717	13.27	16,08	0.19	0.23	50	25
7	2672		31.79		0.39		80	
8	2679	2713	13.86	16.33	0.16	0.23	62	22
9	2674	2712	15.38	15.80	0.18	0.26	54	45
10	2668	2707	15.88	16.14	0.18	0.26	55	49
12	2671	2712	12.59	16.52	0.15	0.28	52	45
13	2663	2703	13.30	18.40	0.15	0.29	54	49
14	2684		36.18		0.43		80	
15	2664	2699	15.61	15.83	0.20	0.26	0,2	0,26
16	2666	2704	12.26	19.03	0.14	0.29	54	48
17	2670	2708	13.35	16.53	0.15	0.26	53	46
18	2665	2702	14,48	16.84	0.17	0.26	53	51
19	2665	2701	15.69	18.49	0.20	0.25	59	50
20	2673	2711	15.01	16.23	0.18	0.27	53	45
21	2660	2696	13.62	19.46	0.16	0.28	67	49
22	2667	2707	13.93	18.03	0.15	0.28	57	48
24	2666	2697	13.37	16.6	0.17	0.21	80	60
25	2671	2708	14.91	17.92	0.18	0.28	52	46

Table 5.2: Table of selected relevant parameters of 2D band Voigt fit for all measurements and for intercalated and pristine HOPG (mean values). Anomalous blisters, fitted with a single component, are highlighted in violet.

5.4. Strain effect

Previous micromechanical studies showed that blistering is an elastical deformation of the HOPG basal plane. According to the Murray model, Blisters consist of a "skin" of few-layers graphene sheets which, because of the pressure of gasses that form inside HOPG during intercalation, detach from the basal plane and become swelled regions (see Section 1). If the skin is cutted with the AFM tip, blisters deflate and the HOPG returns to the original basal plane shape [15]. Considerable pressures (1-10 MPa) where estimated to form inside the skin, consistently with blistering being caused by gasses formed under the HOPG basal plane during the EC processes [7, 15, 56].

The hypotesis of this thesis is that the downshift of the G peak is caused by biaxial strain on the C-C bonds, which is a consequence of the gas internal pressure that bends the skin, as observed in literature for mono and bi-layers graphene bubbles (see Section 2.2.4). The downshift is observed also for the the 2D peak position (with a ratio of about 2,5/1 compared to G downshift).

The average blisters radius R_m was extracted from the AFM images as mean of the maximum and minimum radius (see Section 4.2). From the AFM scans also the maximum height h of the blisters from the HOPG basal plane was extracted. From this data the mean estimation of the % variation on the C-C bond of each the blisters was calculated with a spherical cap approximation of the blister morphology. **Figure 5.4** shows the spherical cap model used and a depiction of biaxial strain on the exagonal structure of a monoatomic layer. R and h are the known parameters, the % strain is connected the ratio beteween the unstrained length l and the strained arc l'.

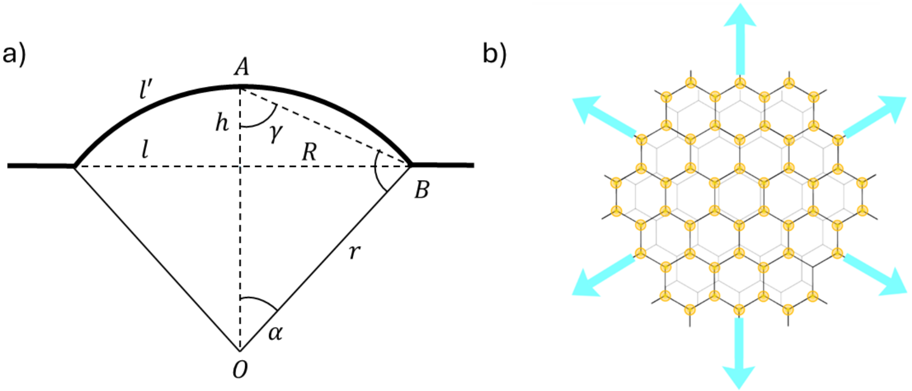

Figure 5.4: a) spherical cap approximation of the blister morphology b) representation of biaxial strain on the C-C bond of graphene [57].

From the morphological parameters R and h, extracted from the AFM scan, the % strain is calculated by the following equations. The angle γ can be obtained as:

$$\gamma = arctan\left(\frac{R}{h}\right) \tag{5.1}$$

Since the AOB triangle is isosceles the angle α is:

$$\alpha = 180 - 2\gamma \tag{5.2}$$

Therefore the length l' of the circle arc is:

$$l' = \frac{2\pi r\alpha}{2\pi} = \frac{2\alpha R}{sin(\alpha)} \tag{5.3}$$

The % strain is obtained as the normalized difference between the unstrained length $l = 2R$ and the strained arc l', which is directly linked to the C-C bond elongation:

$$\%strain = \frac{l' - l}{l} * 100 \tag{5.4}$$

5.4.1. AFM morphology and Raman shift correlation

HOPG blisters have lateral dimensions in the order of the micrometer and heights of tens up to 150 nm, they are therefore actually quite flat structures. However, from the geometric parameters of the analyzed statistic, the calculated strain effect on the C-C bond is between 0.02 and 0.5%, enough to show a distinctive change in the position of the Raman peaks. Since these values are below 1.2% strain studied by Zabel et al. I assumed that the AB stacking of the graphene planes is not altered [31] (see section 2.2.4). **Table 5.3** shows the extracted blister average radius R (μm) and height h (nm), the calculated % strain together with G and 2D positions (cm^{-1}) It is evident from the table that there is a tendency for the blisters with higher % strain to present a bigger downshift of the G and 2D peaks position.

Blister/HOPG	**h** (nm)	**R** (µm)	**% Strain**	**G** pos. (cm^{-1})	**2D$_1$** pos. (cm^{-1})	**2D$_2$** pos. (cm^{-1})
HOPG pristine	0	0	0	1582	2677	2720
HOPG b.p. intercalated	0	0	0	1582	2684	2719
1	118	1.43	0.46	1565	2675	
2	40	1.03	0.10	1578	2671	2708
3	90	1.85	0.16	1579	2675	2710
4	76	1.95	0.10	1580	2682	2718
5	45	2.23	0.03	1579	2680	2716
6	42	1.35	0.06	1580	2681	2717
7	115	1.63	0.33	1565	2672	
8	68	1.93	0.08	1579	2679	2713
9	70	1.60	0.13	1577	2674	2712
10	102	1.70	0.24	1576	2668	2707
12	67	1.30	0.18	1579	2671	2712
13	115	2.00	0.22	1577	2663	2703
14	98	1.50	0.28	1570	2684	
15	95	1.38	0.32	1574	2664	2699
16	85	1.13	0.38	1577	2666	2704
17	65	1.45	0.13	1577	2670	2708
18	65	1.50	0.13	1576	2665	2702
19	100	2.00	0.17	1575	2665	2701
20	85	1.60	0.19	1577	2673	2711
21	80	1.25	0.27	1572	2660	2696
22	105	2.20	0.15	1576	2667	2707
24	120	1.65	0.35	1574	2666	2697
25	70	1.45	0.16	1577	2671	2708

Table 5.3: Morphological parameters extracted from the AFM analysis and correlated % strain estimation; position of the G and 2D band extracted from the fitting procedure.

The dispersion of the G and 2D components Raman shift reported in Table 5.3 is plotted in **Figure 5.5**. There is a correlation between the G and 2D peak components positions: blisters with downshifted G peak present also a 2D band at lower Raman shifts values. The double G blisters, fitted with a single component, seem to follow the tendency line for the $2D_2$ component. I however excluded anomalous blisters from the linear regression since as explained the fitting procedure is not comparable. The results of the linear regression are: slope $= 2,5 \pm 0,3$; $R^2 = 0,82$. The $2D_2$ component follows a very similar correlation with the G downshift: $= 2,4 \pm 0,3$; $R^2 = 0,75$. This correlation between the two peaks seems to confirm that the two shifts are manifestations of the same effect: the strain of the blister skin.

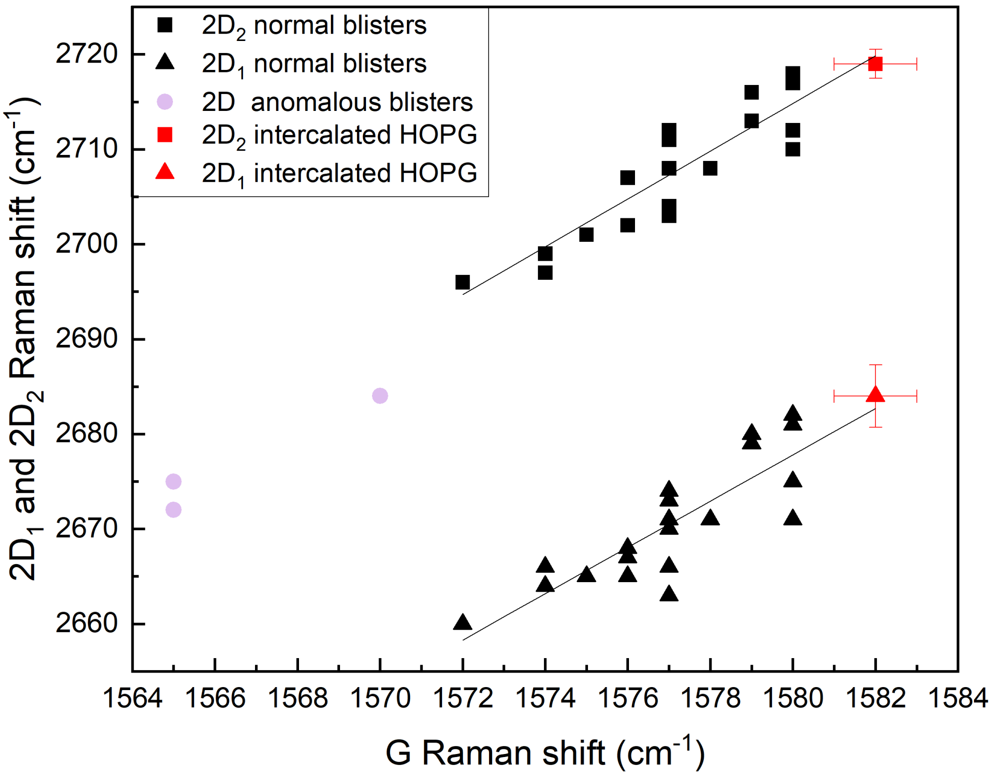

Figure 5.5: 2D components position distribution as a function of the G position in blisters and HOPG. For double G blisters, reported in violet the G position is the most downshifted one. Tendency line slope $= 2.5$; $R^2 = 0,82$ for $2D_1$ and $= 2,4$; $R^2 = 0,75$ for $2D_2$.

If strain is the main cause of the peaks downshift, there should be a correlation with the AFM morphology: the most downshifted blister should present a higher % strain. **Figure 5.6** shows the dispersion of the G peak position with the % strain estimation that followed the AFM morphological analysis.

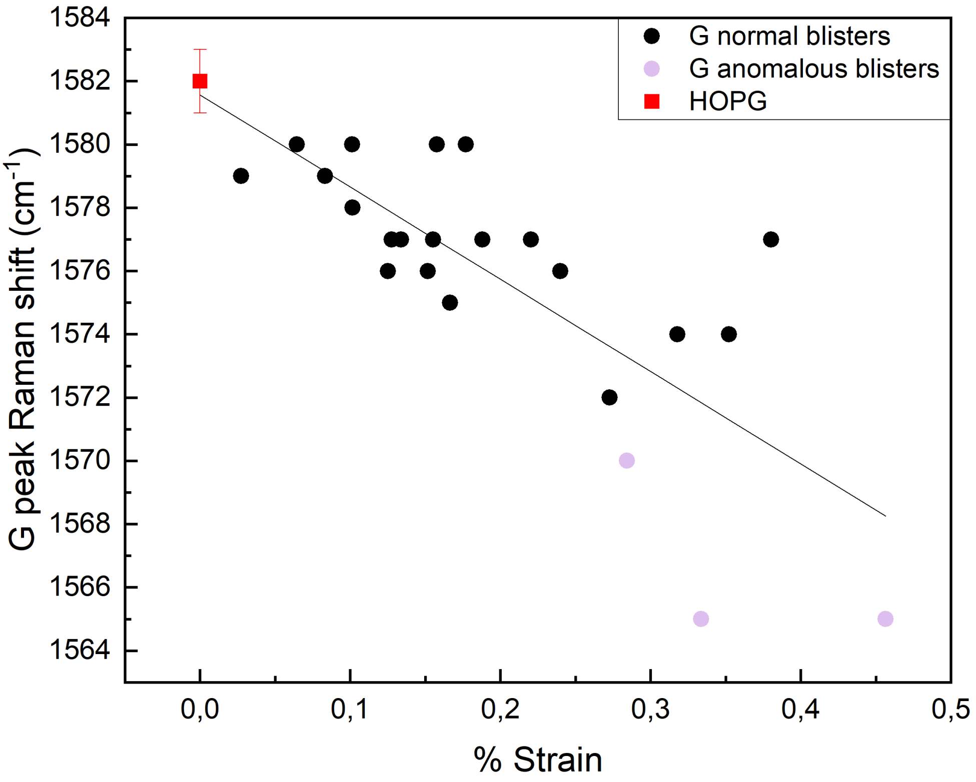

Figure 5.6: G peak Raman shift on individual blisters as a function of the % strain. Double G peak blister are highlighted in violet. Tendency line slope $= -29cm^{-1}/\%$; $R^2 = 0,60$.

.

There is indeed a tendency for the more strained blisters to present bigger shifts of the G peak, and the double G blisters are as expected among the ones with higher strain. The linear regression gives a slope of $-29cm^{-1}/\%$ ($R^2 = 0,60$).

Figure 5.7 shows instead the position of the 2D peak components as functions of the calculated strain. The position of the 2D band components follows a similar correlation with the % strain, with $\sim$ double slope of the G downshift for both $2D_1$ and $2D_2$ components. The linear regression gives a slope of $= -48cm^{-1}/\%$; $R^2 = 0,51$ for $2D_1$ and of $-51cm^{-1}/\%$; $R^2 = 0,56$ for $2D_2$.

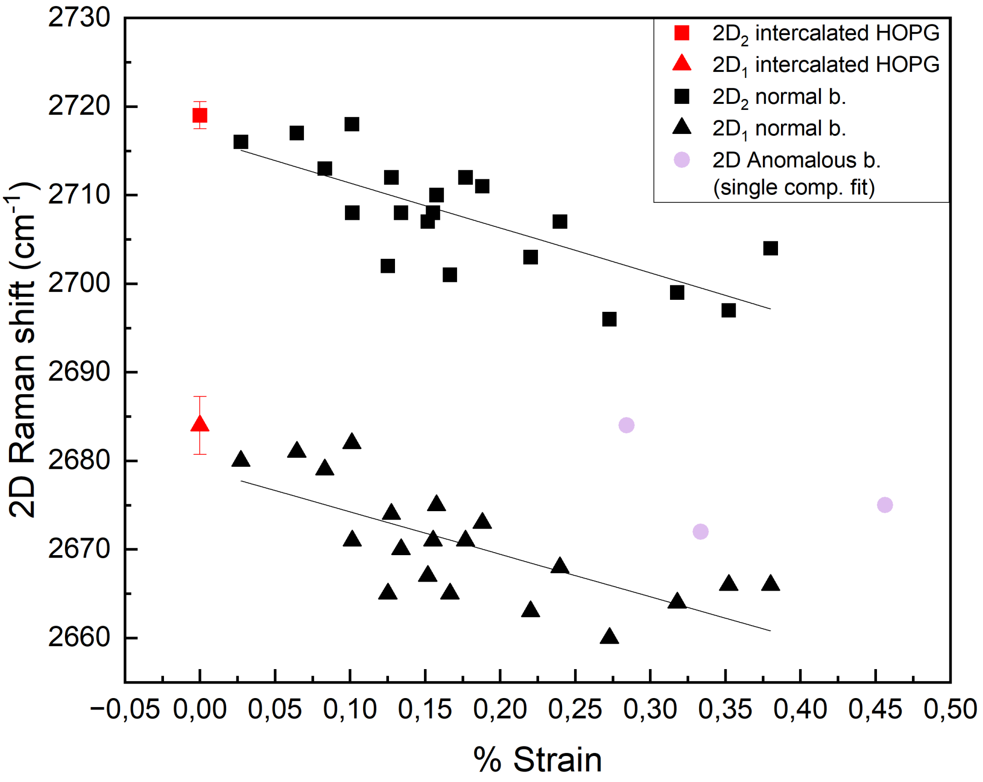

Figure 5.7: 2D components Raman shift on individual blisters as a function of the % strain. Tendency line slope $= -48cm^{-1}/\%$; $R^2 = 0,51$ for $2D_1$ and $-51cm^{-1}/\%$; $R^2 = 0,56$ for $2D_2$. Double G blisters are excluded from the regression since they where fitted with a single component.

These results are consistent with the literature on model systems: Moihuddin et al., for example, reported very similar downshift values for the G^- and 2D components with % strain in uniaxially strained monolayer graphene [27] (see subsection 2.2.4). In biaxial strain experiments on graphene bubbles, G and 2D peak downshifts as function of the % strain are not reported in literature. Experiments focus on the downshift as a function of the internal pressure [30–32]. In principle this data could however be easily calculated and confronted with the values found in blisters. This analysis demonstrates that AFM and Raman parameters are correlated, and that the strain is the dominant factor in the change of the blister peaks position compared to intercalated HOPG.

5.4.2. Blister section and individual points shift

The downshift of the peaks is not uniform on the blister, and extends also in the first $\sim 1\mu m$ of the HOPG basal plane around the swelled region. To further investigate strain effects along different blisters regions (i.e. centre and borders), I performed an analysis of the G and 2D peak position by considering a section of a Raman shift map along the profile of a blister, as shown in **Figure 5.8**. The section is highlighted by the red rectangle in the G peak Raman shift map of Figure 5.8 b). I extracted all the spectra and performed individual fits of the G and 2D peaks as in Section 5.2. In this way I calculated the Raman shift values for every point. This procedure results in a more precise analysis than the intuitive visualization obtained through Raman maps (which simply take the position of the maximum value in the selected spectral range, regardless of the peak lineshape).

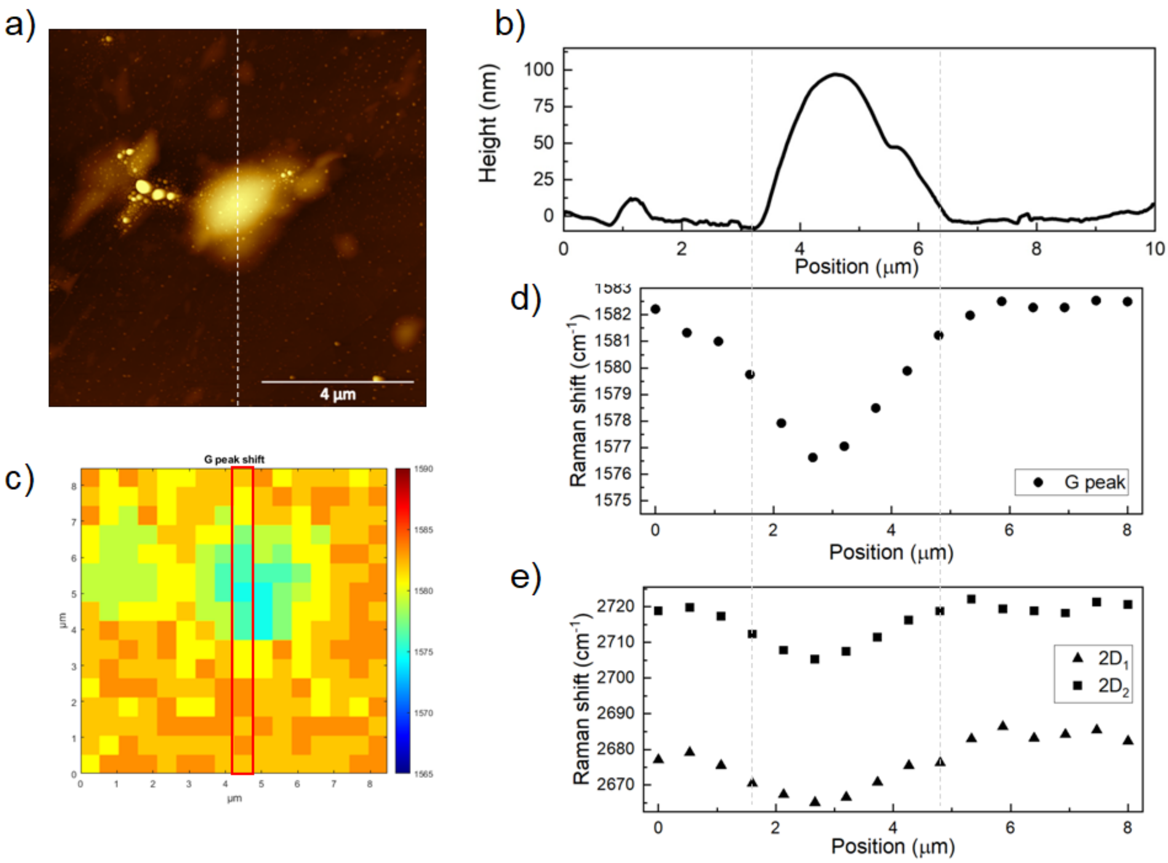

Figure 5.8: a) AFM image and b) section of a blister c) G position map and selected points for the fitting d) G position along the section and e) $2D_1$ and $2D_2$ components position for the same section.

As shown in Figure 5.8, downshift is maximum at the centre of the blister for both G and 2D peak, with $G = 1575cm^{-1}$ ($7cm^{-1}$ downshift from HOPG G peak position) and 2D components at $2D_1 = 2668cm^{-1}$ and $2D_2 = 2707cm^{-1}$ ($15cm^{-1}$ and $13cm^{-1}$ downshifts from the mean intercalated HOPG components positions respectively).

The downshift extends slightly in the neighbouring HOPG regions. This is consistent with the literature on biaxially strained graphene bubbles, that show a very similar behaviour [30]. The non-uniformity of the downshift results in broadening of the spectral features when the blister is considered as an average of many spectral points, like in the previous analysis. TERS (Tip Enhanced Raman Spectroscopy) could bring an even more detailed picture of this system by going below the laser diffraction limit and obtain nanometrically resolved spectral features of a blister section.

5.4.3. Subctration of the HOPG spectrum in anomalous blisters

Anomalous blisters spectra were at first puzzling results, as it was not clear what caused the splitting. The morphological analysis showed that these blisters are heavily strained, and the 2D peak appears to be a sum of different contributions. The hypotesis discussed in this work is that the double G peak in anomalous blister is due to the contribution of the HOPG basal plane under the swelling, which gives the 1582 cm^{-1} feature. Only in these highly strained examples this contribution is resolved from the blister skin component, which, because of strain, is downshifted at $\sim$ 1565-1570 cm^{-1}.

An alternative hypotesis to explain the double G peak could be degeneracy removal due to anisotropic strain, however the higher G component is not downshifted ($1580 - 1582cm^{-1}$ for all double G blisters), while even for completely uniaxial strain the component relative to the vibration mode perpendicular to strain (G^{+} in literature on uniaxial strain) is still shifted with a slope of around $-11cm^{-1}/\%$ strain [27]. Furthermore these blisters have a fairly circular morphology, therefore the strain should be in first approximation uniformly biaxial.

Possible convolution from the graphite around the blister was also considered as a possible cause. This would be a warning that all the spectra are in fact convoluted beyond the Rayleigh diffraction limit for instrumental reasons. The downshifted component is however visible only on points aligned with swelled AFM morphologies and does not appear in the HOPG around the blister. Convolution should instead work in both ways: a downshifted G peak contribution of the blister should also appear in the neighbouring HOPG basal plane regions. Since this effect is not observed in any measurement, I excluded the possibility of convolution as the cause of the G splitting.

Other evidence of the double G peak being caused by the HOPG basal plane under the swelling is the appearance of a $\sim 2720cm^{-1}$ shoulder in the 2D band of the double G blisters, which was ignored in the 2D fitting procedure. To validate this interpretation I performed a tentative subtraction of the HOPG b.p. not normalized spectrum with respect to an anomalous double G blister, as shown in **Figure 5.9**. The black line plots the subtracted spectrum, while the dotted gray line plots the original spectrum. The dotted red line represents the removed HOPG spectrum. The subtraction was performed in hypotesis that the intensity signal of the basal plane is not influenced much by the presence of the blister skin (total penetration). The subtraction results in the removal of the $2D_2$ shoulder leaving a broad single component 2D band.

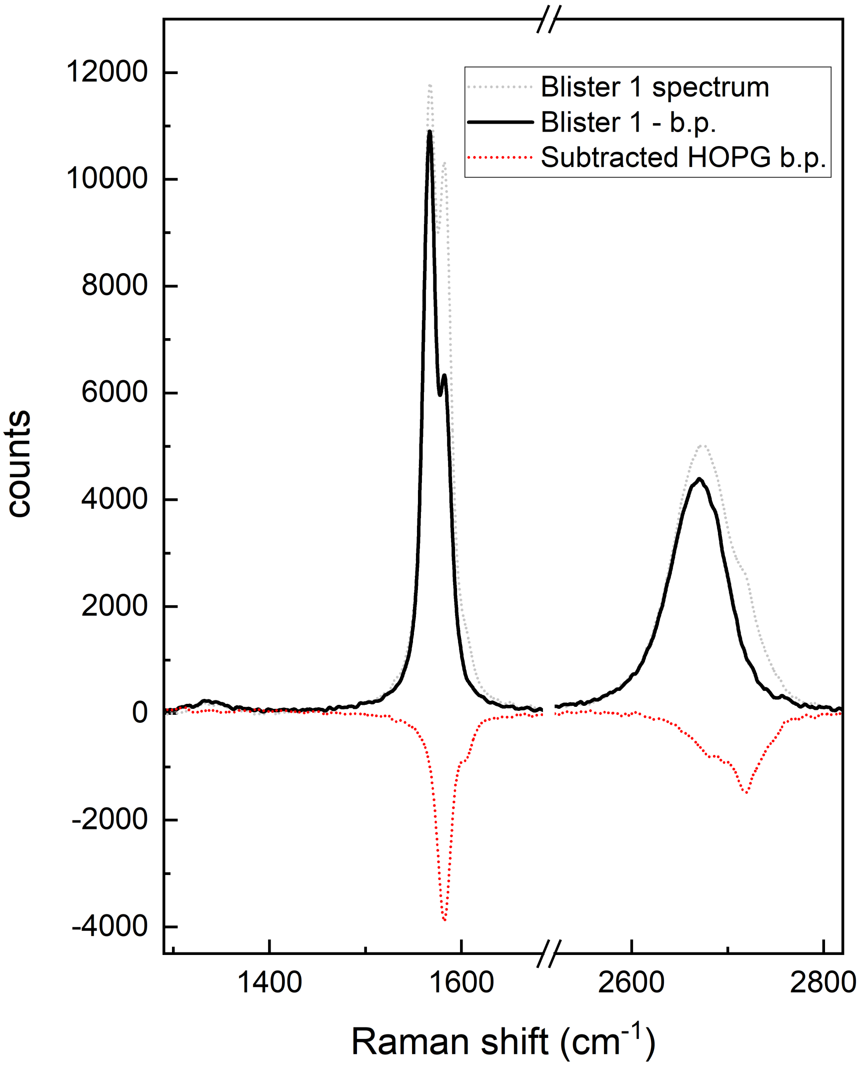

Figure 5.9: Blister 1 spectrum (black line) with HOPG basal plane subtraction (red dotted line). The dotted gray line is the original blister spectrum.

The G peak still shows a residual $1582 cm^{-1}$ component: the subctraction could be refined in further studies by multiplying the HOPG spectra to a suitable coefficient. The broad 2D peak lineshape may be caused by the fact that strain is not uniform on the whole blister, as shown in Section 5.4.2. This is confirmed by the G peak lineshape, which also shows broadening. Other evidence is the fact that also the most shifted normal single G blisters (e.g. b.21 and b.24, see Table 5.2) present bigger FWHM and therefore have broad 2D bands.

One consequence of this interpretation is that the HOPG component should be present in all blisters, and therefore this would complicate the analysis of the 2D band. Furthermore the underlying HOPG contribution could result in a broadening of the G and 2D peaks, which may influence the peaks position calculated through the fitting procedures. There is evidence of this effect in the fact that anomalous double G blisters, where instead the contributions are resolved, have G peak positions below the tendency line (see Figure 5.5).

5.5. Skin thickness analysis

The possibility to investigate the structure and estimate the thickness of the blister skin was the original goal of this thesis work. As I will further expose in this section, an interplay of different phenomena complicates the picture. Strain downshifts the position of the G and 2D peaks, while intercalation effects both the position and intensity of the 2D band components. The blister skin thickness, which in the hypotesis of the Murray model should be of few monoatomic layers, should influence the electronic bands of the system, and thus cause an effect on the 2D peak lineshape. In principle this effect should be comparable to what observed in few-layers graphene flakes by Ferrari et al. [20, 21] (see Section 2.2.1). The starting hypotesis of this section is therefore that the blister skin can be modelled as a multilayer graphene sheet.

Because of intercalation and strain, it is however difficult to decouple these "skin-thickness" effects and obtain a quantitative description. Moreover, if the hypotesis of Section 5.4.2 is true, the contribution of the underlying HOPG basal plane is present in all blisters. This further contribution should therefore also be considered. Some interesting qualitative conclusions can however be drawn from the statistical analysis. The main effects that can be used to draw conclusions on the blister skin thickness are the 2D band lineshape and the G peak enhancement. Another idea to estimate the skin thickness could be to evaluate the shift of the 2D components, which is influenced by the number of layers [21]. The effect of Strain however dominates the Raman shift of the peaks, as previously exposed. This analysis can't therefore be considered a sound procedure.

5.5.1. 2D band lineshape in blisters

The 2D peak is "graphitic" in most of the analyzed spectra (the $2D_1/2D_2$ intensity ratio is around 0.6-0.8 in the majority of blisters). This suggest that blisters of these sizes are often buried below a consistent number of layers (> 5). The precise identification of the number of layers through the 2D lineshape on these blisters is therefore rather difficult. As I exposed, The 2D lineshape is influenced by intercalation, which G_i maps show to be not correlated to the presence of the blister. It is also not clear if intercalation occurs inside the blister skin or in the basal plane under the swelled region. I performed a tentative subtraction of the HOPG basal plane, in the same total penetration hypotesis of Section 5.4.2, but no significant variation of the peak lineshape was observed (the intensity of the HOPG spectrum is low compared to blister spectra, and the two lineshapes are still quite similar).

Even if a quantitative description is difficult, the variation of the 2D lineshape and of the $2D_1/2D_2$ intensity ratio compared to the intercalated b.p. around the swelled regions should be mainly generated by "skin thickness" effects. The blister skin is therefore thin enough so that the electronic bands of the sheets of the skin are not the same as of bulk HOPG. Some b. present very different 2D lineshapes compared to the intercalated b.p. (e.g. b. 3, b. 15, see Appendix B). This is indication that these blister should be more "superficial" and have very thin skins, of just few graphenic layers. A reasonable estimation of the skin thicknesses is between ~ 3 and 30 layers. **Figure 5.10** shown examples of then 2D band of a) a "deep" (blister 13) and b) a more "superficial" one (blister 3), with the fitting parameters calculated in Section 5.2.

The 2D lineshape of the blister of Figure 5.10 a) is similar to intercalated HOPG apart from the strain downshift effect. The blister skin should therefore be relatively thick (> 10 layers). The blister spectra of Figure Figure 5.10 b) shows instead a different lineshape, which is interpreted as due to the change of the graphite electronic bands of the blister skin, as we approach a few-layers graphene system. The blister should therefore be superficial, with an estimated thickness (by comparison with Figure 2.5) of around 3-6 layers.

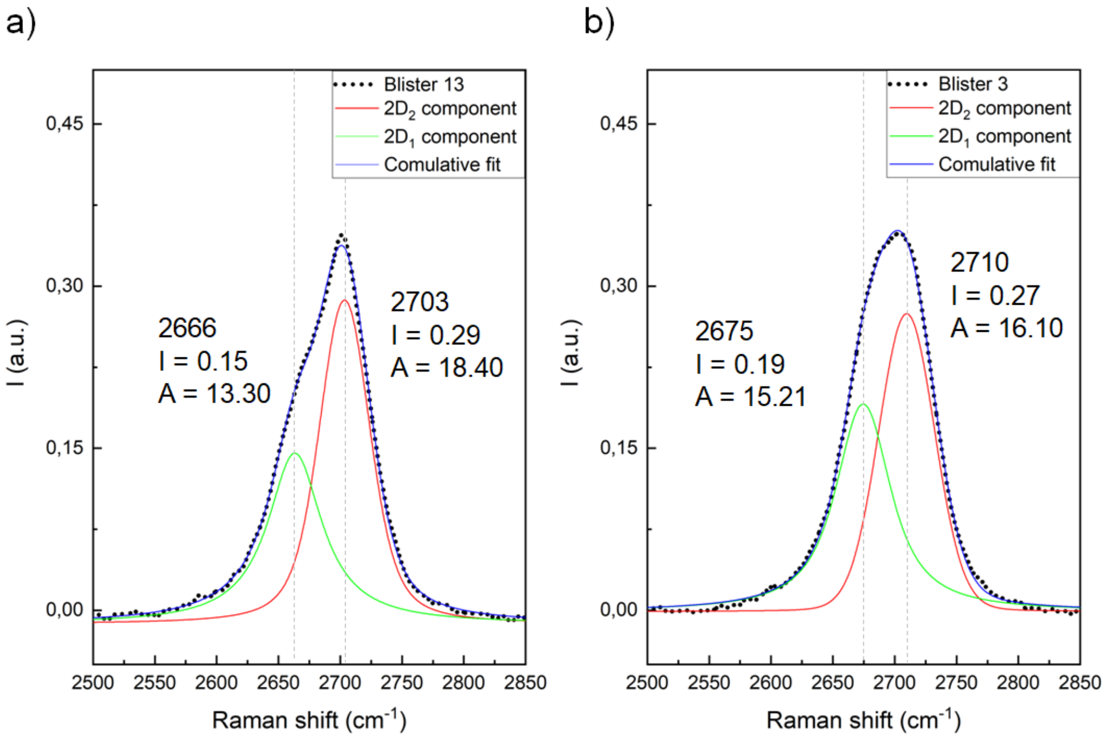

Figure 5.10: 2D fit for a) a "deep" and b) a more "superficial" blister, with fitting parameters.

5.5.2. G peak enhancement in blisters

The enhancement of the G peak intensity observed in graphene flakes deposited on SiO_2 is described in Section 2.2.2. This phenomenon is due to interference effects at the interface with SiO_2 and is highly dependent on the substrate material [23, 24]. No direct correlation can therefore be made between the intensity values of few-layers graphene-SiO_2 systems and blisters. I however hypotesize that similar interference effect at the interface between the blister skin and the pressurized gasses inside the skin are present. This should be the cause of the G peak absolute intensity enhancement in blisters compared to the HOPG basal plane, where there are no such interfaces. G peak enhancement in blister reaches $I_{G_B}/I_{g_{HOPG}}$ ratios of 5/1 (see Table 5.1). This suggest that some b. should have skins of around 10 layers, which is the depth of maximum enhancement observed in SiO_2 deposited flakes [23]. The mean enhancement in blisters is 3,5. Further studies of this phenomenon in other few-layered systems could help to clarify the effect.

One last speculation on the G enhancement effect, which further suggest that its mechanism relies on interference phenomena at the blister interface, can be drawn from the analysis of optical images of intercalated HOPG. During the measurements I found that at the optical 100x microscope view used to choose the AFM scan site, the HOPG surface appeared as a light gray surface with black spots (See Figure 3.12). I then found that these spots were often revealed at the AFM view as blisters, a surprising result since their nanometric height should not cause any optical contrast. I was not able to explain this correlation, but it however helped me in optimizing the blisters "hunt" with exploratory scans, since I could hypotesize the presence of big blisters even before the AFM measure, and this saved a lot of time.

In few-layered graphene flakes deposited on SiO_2, the indicative thickness of different flake areas is visible at the optical contrast, with thicker sheets that appear darker [58]. This result is related to optical absorption and has an effect on the Raman intensity signal. As exposed, the G peak intensity shows an enhancement with the number of layers and a maximum around ten layers, while monoayer graphene and graphite have similar G peak intensities. A possible interpretation is therefore that the appearance of blisters as dark spots at the optical view is correlated with interference effects at the interface with the gas, which results in higher light absorption. This effect would be consistent with the enhanced Raman signal discovered on blisters. Further studies should investigate and prove the alignment of optical and AFM features. If this correlation is confirmed, high resolution optical microscopy could start playing a new role in the study of blisters.

5.6. Internal pressure estimation

A precise calculation of the internal pressure of the system requires the knowledge of the blister skin thickness. Nevertheless, some indicative mean results can be drawn with a simplified model and the assumption of thicknesses suggested by the previous discussion (3-30 layers). For monolayer graphene bubbles the internal pressure ΔP was calculated in literature with the following equation [30]:

$$\Delta P = \frac{h^3}{R^4} k E_t \tag{5.5}$$

Where h and R are the morhological parameters, k is an adimensional constant $= 3.10$ and $E_t = 390$ N/m is the in-plane stiffness for monolayer graphene. The calculation is more complex for bi and few-layers sheets since the interplanar shear stress should also be considered. The interaction between atomic sheets results in an overall increased stiffness of the membrane compared to just consider non interacting monolayers sheets staked on top of each other. For this preliminary mean estimation, I however decided for simplicity to consider the effect of the number of layers just by multiplying equation 5.6 for n_{layers}:

$$\Delta P = \frac{h^3}{R^4} k E_t n_{layers} \tag{5.6}$$

This must be considered a lower bound estimation. For the analyzed blisters the mean morphology is $h_m \approx 80nm$, $R_m \approx 1.6\mu m$, which give a ΔP, for the 3-30 layers thickness range, between 0.3 and 3 MPa. This result is in the same order of magnitude of previous micromechanical studies (1-10 MPa) [15]. A more detailed model introducing interplanar shear stress and an accurate analysis of individual blister stratigraphy could improve this result and enable a non-destructive approach to blisters internal pressure calculation. A connection between the Raman results, the AFM morphology and the surface energy of the system, which could be modelled by the Laplace equation, goes beyond the scope of this thesis work. This approach could however be an interesting new path of study in the description of blisters.

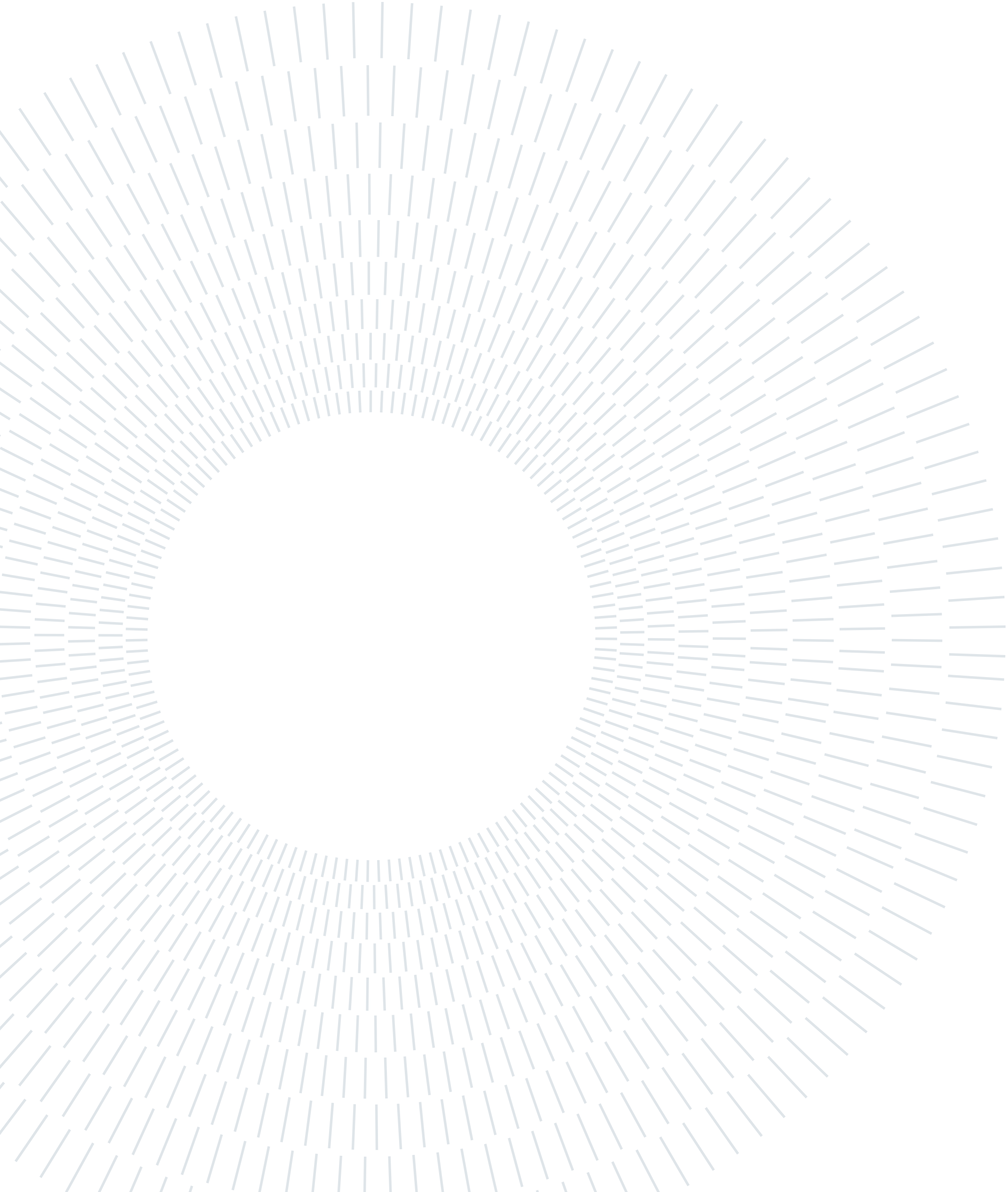

6 | Conclusions and perspectives

The combined AFM-Raman experimental setup employed in this thesis work permits to obtain a more detailed picture of HOPG blisters than ever before. The combination of these techniques allows to correlate the AFM morphology with Raman spectral features, which can be clearly attributed to be characteristic of the blister or of the intercalated HOPG basal plane. Individual blister spectra were already analyzed in previous researches on the topic. Combined in-situ AFM-Raman mapping measures on intercalated HOPG were also recently performed [13, 15]. However, a sistematic statistical analysis on blisters Raman spectral features correlated with their AFM morphology was never conducted before.

The analysis revealed a complex interplay of phenomena that influence the Raman spectra of blisters, which is remarkably different on swelled regions with respect to the intercalated HOPG basal plane. These results are of tricky interpretation since the interplay between the different structural modifications of the HOPG structure that influence the Raman spectra are difficult to decouple. An extensive analysis of literature results on model systems like biaxially strained mono and bi-layer bubbles, few-layers deposited graphene flakes, as well as average Raman studies on intercalated HOPG, was therefore necessary to try to shine a light on the system phenomenology.

The position of the G and 2D peaks on blisters, which show a downshift compared to the intercalated HOPG basal plane, is dominated by strain effects. According to the Murray model, Blisters are elastical swellings of the HOPG surface, with few-layers graphene skins lifted from the basal plane because of the presence of gasses formed in the graphitic structure during intercalation. The strain of the C-C bonds generates a softening of the phonon vibrational modes of the graphite layers of the skin, and this results in a downshift of the Raman peaks. Strain in blisters was quantified thanks to AFM measures and these values were correlated with the relative downshifts in the peaks position obtained by the Raman spectra. The downshift of the peaks compared to the % strain is consistent with the literature on strained mono-and bilayer graphene [27, 30, 31].

Other effects influence the blister spectra: their quantitative correlation with blisters morphology and stratigraphy is difficult, but some qualitative results were anyway obtained by the analysis. Blisters skins approach few-layers graphene thicknesses, enough to present different electronic bands from bulk HOPG. This effect results in an additional modification of the 2D peak lineshape compared to the HOPG basal plane, where instead intercalation is the main factor that influence the relative intensity of the two components, $2D_1$ and $2D_2$, of the 2D band. These effects are difficult to decouple. Furthermore, some measurements on "anomalous" blisters which presented a splitted G peak made of two components, suggested that also the HOPG basal plane under blister skins gives a contribution of the Raman spectrum. From this analysis it was anyway possible to estimate that blisters skins are thin enough to show an effect on the spectral features: thicknesses of between 3-30 layers were estimated.

This thickness estimation is supported also by the enhancement of the G peak intensity which was observed in blisters compared to the HOPG basal plane. This effect is due to interference phenomena which were studied on few layer graphene deposited on SiO_2 [23, 24]. The effect is highly dependent on the substrate, and shows a maximum around ten layers, while monolayer graphene and bulk HOPG have similar G peak intensities. Similar phenomena may also play a role in blisters, suggesting thicknesses of few up to tens of layers. This topic could be the subject of further studies.

The thicknesses results were again correlated with the AFM morphology to give a rough mean estimation of the internal pressure inside the blister skin. The calculations give values between 0.3 and 3 MPa, a result consistent with previous micromechanical studies [15], which again seem to confirm the "trapped gas" picture of the Murray model.

All these results could not be obtained without the combined experimental setup that was employed in this work. This thesis work is a promising example of AFM-Raman correlation: with combined measurements one can obtain more information than with the independent use of the two techniques. In situ-and in-operando combined analysis on blisters are the next steps in future applications of the technique.

A further development in the study of intercalated HOPG is the use of Tip Enhanced Raman Spectroscopy (TERS) on blister structures. TERS is an even more sophisticated combined AFM-Raman technique, based on a special metallic tip (generally made of gold or silver) which is employed to concentrate the incident light field at the apex. The tip acts as a nano-source of light and local field enhancer, greatly improving Raman sensitivity [59]. With this configuration it is possible to go beyond the diffraction limit and reduce the probed volume to a nanometric region below the tip apex. In this way it would be possible to obtain a way more detailed picture of the blister skin, with higher lateral resolution and without the contribution of the underlying HOPG basal plane. Section analysis on a blister profile could characterize the blister not with a mean spectrum, as done in this work, but with individual contributions of the different blister regions. This analysis would permit to evaluate differences between the spectral features of the blister center, its border, and the closest HOPG region around the swelling, as exemplified by the preliminary analysis conducted in Section 5.4.2.

The combined system employed in this thesis work, however, should not be considered as just a preliminary technique to TERS. The higher versatily and simplicity of the apparatus, which avoids some of the complications involved in TERS, make combined AFM-Raman an interesting technique by its own right. This thesis work highlights the potential of combined AFM-Raman analysis in the study of nanostructured surface systems, as well as it current limitations. The combined technique is a versatile setup that can be used for many applications in surface physics. This work should be considered as an important case study, exemplar for further developments of this innovative experimental techniques.

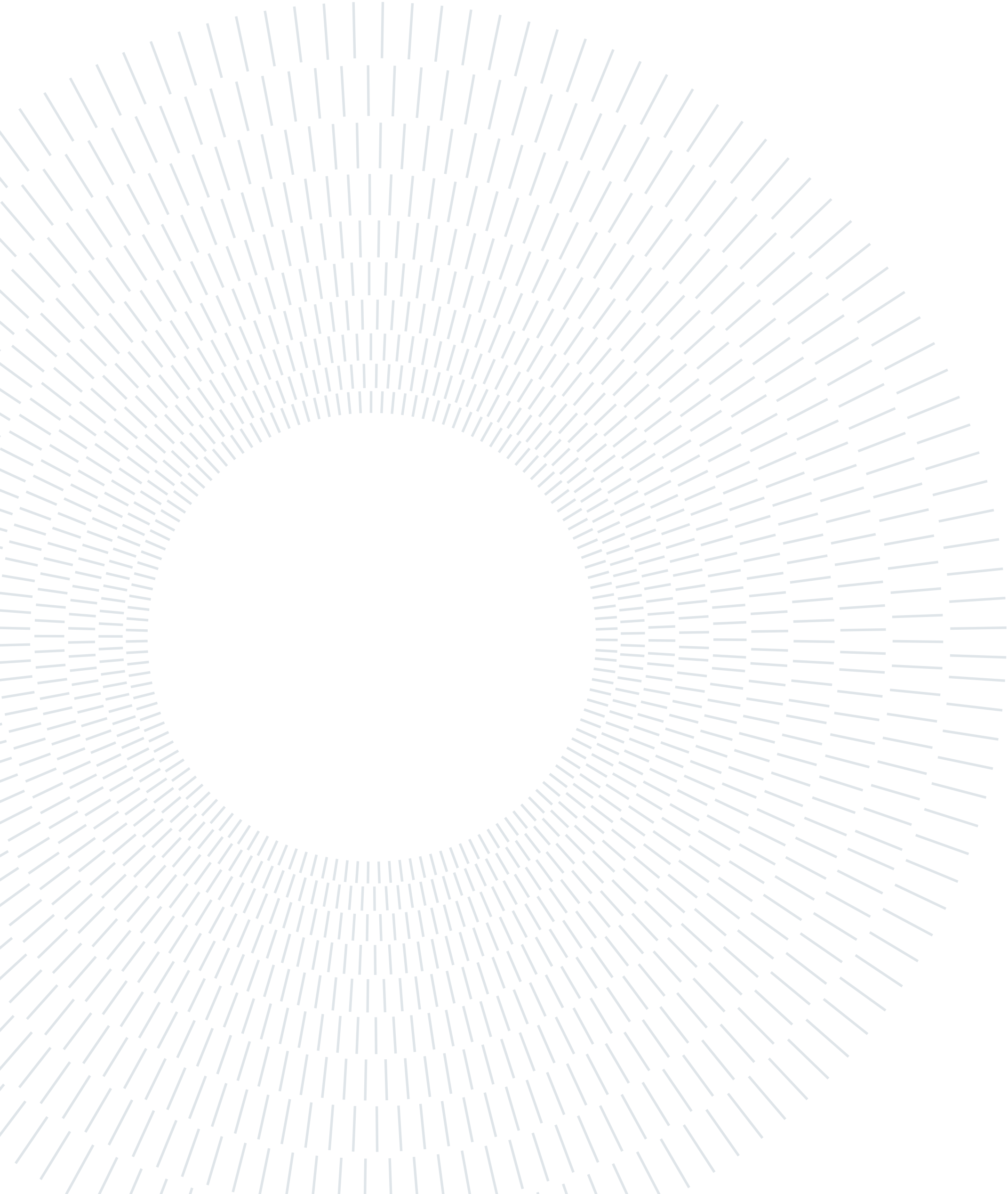

Bibliography

[1] Jürgen O. Besenhard and Heinz P. Fritz. The electrochemistry of black carbons. *Angewandte Chemie International Edition in English*, 22(12):950–975, 1983.

[2] Arava Leela Mohana Reddy, Anchal Srivastava, Sanketh R. Gowda, Hemtej Gullapalli, Madan Dubey, and Pulickel M. Ajayan. Synthesis of nitrogen-doped graphene films for lithium battery application. *ACS Nano*, 4:6337–6342, 11 2010.

[3] A. K. Geim and K. S. Novoselov. *The rise of graphene*, pages 11–19. 2007.

[4] Yivlialin Rossella. Anion intercalation in graphite: a combined electrochemical atomic force and scanning tunneling microscopy investigation, 2017.

[5] M. S. Dresselhaus and G. Dresselhaus. Intercalation compounds of graphite. *Advances in Physics*, 51:1–186, 1 2002.

[6] Rossella Yivlialin, Luigi Brambilla, Gianlorenzo Bussetti, Matteo Tommasini, Andrea Li Bassi, Carlo Spartaco Casari, Matteo Passoni, Franco Ciccacci, Lamberto Duò, and Chiara Castiglioni. Evolution of the graphite surface in phosphoric acid: An afm and raman study. *Beilstein Journal of Nanotechnology*, 7:1878–1884, 2016.

[7] R. Yivlialin, G. Bussetti, L. Brambilla, C. Castiglioni, M. Tommasini, L. Duò, M. Passoni, M. Ghidelli, C. S. Casari, and A. Li Bassi. Microscopic analysis of the different perchlorate anions intercalation stages of graphite. *Journal of Physical Chemistry C*, 121:14246–14253, 7 2017.

[8] Rossella Yivlialin, Luigi Brambilla, Alessandra Accogli, Eugenio Gibertini, Matteo Tommasini, Claudio Goletti, Marco Leone, Lamberto Duò, Luca Magagnin, Chiara Castiglioni, and Gianlorenzo Bussetti. Evidence of graphite blister evolution during the anion de-intercalation process in the cathodic regime. *Applied Surface Science*, 504, 2 2020.

[9] Francois Beguin, E. Raymundo-Piñero, and Elzbieta Frackowiak. Carbons for electrochemical energy storage and conversion systems. *Chapter 8 Electrical Double-Layer Capacitors and Pseudocapacitors*, pages 329–375, 01 2009.

[10] Ryan Newson. Dynamics of carriers and photoinjected currents in carbon nanotubes and graphene. 01 2010.

[11] B. Partoens and F. M. Peeters. From graphene to graphite: Electronic structure around the K point. , 74(7):075404, August 2006.

[12] M. S. Dresselhaus and G. Dresselhaus. Intercalation compounds of graphite. 1980.

[13] Gianlorenzo Bussetti, Marco Menegazzo, Sergei Mitko, Chiara Castiglioni, Matteo Tommasini, Andrea Lucotti, Luca Magagnin, Valeria Russo, Andrea Li Bassi, Martina Siena, Alberto Guadagnini, Samuele Grillo, Davide Del Curto, and Lamberto Duò. A combined raman spectroscopy and atomic force microscopy system for in situ and real-time measures in electrochemical cells. *Materials*, 16, 3 2023.

[14] Kevin W Hathcock, Jay C Brumfield, Charles A Goss, Eugene A Irene, and Royce W Murray. Incipient electrochemical oxidation of highly oriented pyrolytic graphite: correlation between surface blistering and electrolyte anion intercalation. *Analytical Chemistry*, 67(13):2201–2206, 1995.

[15] Marco Menegazzo, Lorenzo Marfori, Rossella Yivlialin, Alessandro Podestà, Franco Ciccacci, Lamberto Duò, Valeria Russo, Marcello Campione, and Gianlorenzo Bussetti. Stiffness and mechanical manipulation of blisters grown on electrochemically intercalated graphite. *Electrochimica Acta*, 488, 6 2024.

[16] A. Smekal. Zur quantentheorie der dispersion. *Naturwissenschaften*, 1923.

[17] C. V. Raman and K. S. Krishnan. A New Type of Secondary Radiation. , 121(3048):501–502, March 1928.

[18] Paul Rostron, Safa Gaber, and Dina Gaber. Raman spectroscopy, a review. 2016.

[19] P. J. Larkin. Introduction: Infrared and raman spectroscopy. 2011.

[20] A. C. Ferrari, J. C. Meyer, V. Scardaci, C. Casiraghi, M. Lazzeri, F. Mauri, S. Piscanec, D. Jiang, K. S. Novoselov, S. Roth, and A. K. Geim. Raman spectrum of graphene and graphene layers. *Physical Review Letters*, 97, 2006.

[21] Andrea C. Ferrari. Raman spectroscopy of graphene and graphite: Disorder, electron-phonon coupling, doping and nonadiabatic effects. *Solid State Communications*, 143:47–57, 7 2007.

[22] L. M. Malard, M. A. Pimenta, G. Dresselhaus, and M. S. Dresselhaus. Raman spectroscopy in graphene, 4 2009.

[23] Y. Y. Wang, Z. H. Ni, Z. X. Shen, H. M. Wang, and Y. H. Wu. Interference enhancement of Raman signal of graphene. *Applied Physics Letters*, 92(4):043121, 01 2008.

[24] Duhee Yoon, Hyerim Moon, Hyeonsik Cheong, Jin Sik Choi, Jung Ae Choi, and Bae Ho Park. 12991303 pacs numbers: 73.22.-f, 78.30.-j, 78, 2009.

[25] Claudia Filoni, Bahram Shirzadi, Marco Menegazzo, Eugenio Martinelli, Corrado Di Natale, Andrea Li Bassi, Luca Magagnin, Lamberto Duò, and Gianlorenzo Bussetti. Compared ec-afm analysis of laser-induced graphene and graphite electrodes in sulfuric acid electrolyte. *Molecules*, 26, 12 2021.

[26] Rossella Yivlialin, Luigi Brambilla, Gianlorenzo Bussetti, Matteo Tommasini, Andrea Bassi, Carlo Casari, Matteo Passoni, Franco Ciccacci, Lamberto Duò, and Chiara Castiglioni. Evolution of the graphite surface in phosphoric acid: An afm and raman study. *Beilstein Journal of Nanotechnology*, 7:1878–1884, 11 2016.

[27] T. M.G. Mohiuddin, A. Lombardo, R. R. Nair, A. Bonetti, G. Savini, R. Jalil, N. Bonini, D. M. Basko, C. Galiotis, N. Marzari, K. S. Novoselov, A. K. Geim, and A. C. Ferrari. Uniaxial strain in graphene by raman spectroscopy: G peak splitting, grüneisen parameters, and sample orientation. *Physical Review B - Condensed Matter and Materials Physics*, 79, 5 2009.

[28] Zhen Hua Ni, Ting Yu, Yun Hao Lu, Ying Ying Wang, Yuan Ping Feng, and Ze Xiang Shen. Uniaxial strain on graphene: Raman spectroscopy study and band-gap opening. *ACS Nano*, 2(11):2301–2305, 2008. PMID: 19206396.

[29] Ioannis Polyzos, Massimiliano Bianchi, Laura Rizzi, Emmanuel N. Koukaras, John Parthenios, Konstantinos Papagelis, Roman Sordan, and Costas Galiotis. Suspended monolayer graphene under true uniaxial deformation. *Nanoscale*, 7:13033–13042, 2015.

[30] Guorui Wang, Zhaohe Dai, Yanlei Wang, Pingheng Tan, Luqi Liu, Zhiping Xu, Yueguang Wei, Rui Huang, and Zhong Zhang. Measuring interlayer shear stress in bilayer graphene. *Physical Review Letters*, 119, 7 2017.

[31] Jakob Zabel, Rahul R. Nair, Anna Ott, Thanasis Georgiou, Andre K. Geim, Kostya S. Novoselov, and Cinzia Casiraghi. Raman spectroscopy of graphene and bilayer under biaxial strain: Bubbles and balloons. *Nano Letters*, 12:617–621, 2 2012.

[32] Zhiwei Peng, Xiaolin Chen, Yulong Fan, David J. Srolovitz, and Dangyuan Lei. Strain

engineering of 2d semiconductors and graphene: from strain fields to band-structure tuning and photonic applications, 12 2020.

[33] G Binnig, C F Quate' ', Edward L Gi, and Ch Gerber. Atomic force microscope, 1986.

[34] Gerhard Meyer and Nabil M. Amer. Novel optical approach to atomic force microscopy. *Applied Physics Letters*, 53(12):1045–1047, 09 1988.

[35] J B Pethica and W C Oliver. Tip surface interactions in stm and afm. *Physica Scripta*, 1987(T19A):61, jan 1987.

[36] Takashi Kouzeki, Shinya Tatezono, and Hisao Yanagi. Electrochromism of orientation-controlled naphthalocyanine thin films. *The Journal of Physical Chemistry*, 100(51):20097–20102, 1996.

[37] Bruno Torre, Claudio Canale, Davide Ricci, and Pier Carlo Braga. *Measurement Methods in Atomic Force Microscopy*, pages 19–29. Humana Press, Totowa, NJ, 2011.

[38] M. Saint Jean, S. Hudlet, C. Guthmann, and J. Berger. Van der Waals and capacitive forces in atomic force microscopies. *Journal of Applied Physics*, 86(9):5245–5248, 11 1999.

[39] Yurii S Barash and Vitalii L Ginzburg. Electromagnetic fluctuations in matter and molecular (van-der-waals) forces between them. *Soviet Physics Uspekhi*, 18(5):305, may 1975.

[40] Victor L Mironov. *Fundamentalsof Scanning Probe Microscopy.* Russian academy of sciences institute for physics of microstructures, 2004.

[41] B.V Derjaguin, V.M Muller, and Yu.P Toporov. Effect of contact deformations on the adhesion of particles. *Journal of Colloid and Interface Science*, 53(2):314–326, 1975.

[42] K.L. Johnson, Kevin Kendall, and A.D. Roberts. Surface energy and contact of elastic solids. *Proceedings of The Royal Society A: Mathematical, Physical and Engineering Sciences*, 324:301–313, 09 1971.

[43] Ricardo Garcõ Âa, Rube Ân, and Pe Ârez. Dynamic atomic force microscopy methods, 2002.

[44] Javier Tamayo and Ricardo García. Effects of elastic and inelastic interactions on

phase contrast images in tapping-mode scanning force microscopy. *Applied Physics Letters*, 71:2394–2396, 10 1997.

[45] Allen J Bard, Larry R Faulkner, et al. Fundamentals and applications. *Electrochemical methods*, 2(482):580–632, 2001.

[46] Vladimir S Bagotsky. *Fundamentals of electrochemistry.* John Wiley & Sons, 2005.

[47] Su-Il Pyun, Heon-Cheol Shin, Jong-Won Lee, Joo-Young Go, Su-Il Pyun, Heon-Cheol Shin, Jong-Won Lee, and Joo-Young Go. Electrochemical methods. *Electrochemistry of Insertion Materials for Hydrogen and Lithium*, pages 11–32, 2012.

[48] Christopher Brett. Fundamentals of electrochemistry. In *Piezoelectric transducers and applications*, pages 223–239. Springer, 2004.

[49] Howard Reiss and Adam Heller. The absolute potential of the standard hydrogen electrode: a new estimate. *The Journal of Physical Chemistry*, 89(20):4207–4213, 1985.

[50] György Inzelt. Electrode potentials. In *Handbook of reference electrodes*, pages 1–24. Springer, 2013.

[51] Dale AC Brownson, Craig E Banks, et al. *The handbook of graphene electrochemistry*, volume 201. Springer, 2014.

[52] Adolph Fick. V. on liquid diffusion. *The London, Edinburgh, and Dublin Philosophical Magazine and Journal of Science*, 10(63):30–39, 1855.

[53] Hao Wang, Sayed Youssef Sayed, Erik J. Luber, Brian C. Olsen, Shubham M. Shirurkar, Sankaranarayanan Venkatakrishnan, Ushula M. Tefashe, Anna K. Farquhar, Eugene S. Smotkin, Richard L. McCreery, and Jillian M. Buriak. Redox flow batteries: How to determine electrochemical kinetic parameters. *ACS Nano*, 14(3):2575–2584, 2020. PMID: 32180396.

[54] F Beck, H Junge, and H Krohn. Graphite intercalation compounds as positive electrodes in galvanic cells. *Electrochimica Acta*, 26(7):799–809, 1981.

[55] T. Wilson. Resolution and optical sectioning in the confocal microscope. *Journal of Microscopy*, 244(2):113–121, 2011.

[56] Rossella Yivlialin, Luca Magagnin, Lamberto Duò, and Gianlorenzo Bussetti. Blister evolution time invariance at very low electrolyte ph: H2so4/graphite system investigated by electrochemical atomic force microscopy. *Electrochimica Acta*, 276:352–361, 6 2018.

[57] Ho-Kin Tang, E Laksono, J. Rodrigues, Pinaki Sengupta, Fakher Assaad, and S Adam. Interaction-driven metal-insulator transition in strained graphene. *Physical Review Letters*, 115, 05 2015.

[58] benjamin mbaluka John, Paul Ngumbi, Ngei Katumo, Simon Mugo, Nelson Timonah, James Ngaruiya, and P Student. Determination of graphene layers by optical imaging contrast analysis. 3297, 11 2015.

[59] Prompong Pienpinijtham, Yasutaka Kitahama, and Yukihiro Ozaki. Progress of tip-enhanced raman scattering for the last two decades and its challenges in very recent years. *Nanoscale*, 14:5265–5288, 2022.

[60] Andrii Nikolenko, V Gubanov, M Biliy, and Leonid Bulavin. Dispersion of electron-phonon resonances in one-layer graphene and its demonstration in micro-raman scattering. *Journal of nanoscience and nanotechnology*, 12:8671–5, 11 2012.

A | Appendix: preliminary studies on HOPG

I conducted preliminary studies on pristine and intercalated HOPG using the SoLINano NT-MDT Raman spectrometer (633, 532 and 473 nm sources) as well as the Nanolab Renishaw spectrometer, which has excitations at 514 and 457 nm. The main scope of this analysis was to identify the optimal number of CVs, the maximum laser power usable, the best excitation to choose, and to investigate the possibility to wash the sample with ultra-pure H_2O.

A.1. Raman spectroscopy of pristine HOPG

The measurements on pristine HOPG verified the 2D peak shift with the excitation, an effect due to double resonance, as shown in **Figure A.1**. The peak presents a rigid shift of $93,2cm^{-1}/eV$, consistent with literature data [20, 21, 60] (see Section 2.2).

The 457 nm excitation pristine HOPG spectrum presented an anomalous upshift of the G peak position at around 1586 cm^{-1}. I verified the calibiration on Si and still observed the upshift on a diamond sample (the signature diamond peak Raman shift is $1332cm^{-1}$, but it was experimentally observed at $1337cm^{-1}$). The spectrometer is optimized for the green excitation, I therefore conclude that there is some instrumental problem that alters the linearity of the apparatus for the blue laser. I therefore calibrated the spectrometer on diamond instead of Si for the 457 nm excitation to mitigate this effect.

The relative intensity of the 2D peak is also dependent on the laser wavelength: higher energy photons cause an enhancement of double resonance (DR) processes and consequently a higher 2D peak relative intensity (0.32, 0.41, 0.49, 0.53 and 0.72 for 633, 532, 514, 473 and 457 nm excitations respectively).

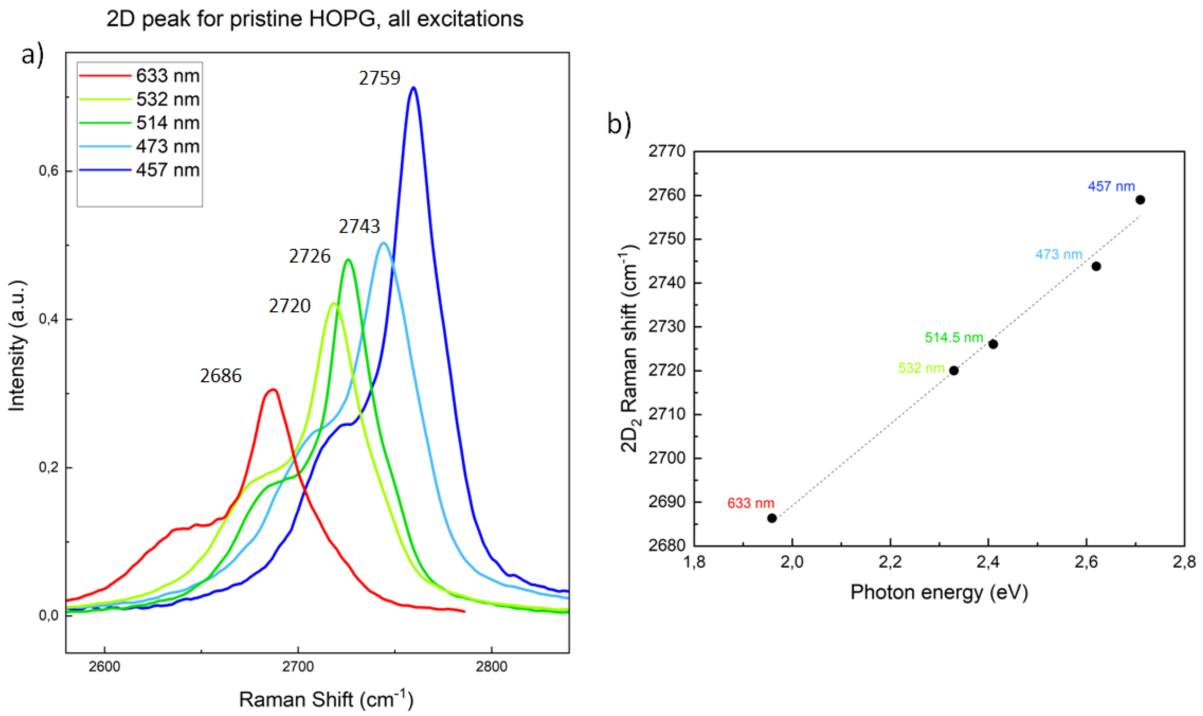

Figure A.1: a) 2D band for pristine HOPG at different excitations b) $2D_2$ component position as a function of the excitation energy: tendecy line slope $= 93,2cm^{-1}/eV$, $R^2 = 0,99$.

A.2. Intercalated HOPG

The comparative analysis on 1,2 and 4 CV intercalated samples showed an increase of the G_i peak with the number of cycles, as well as a modification of the 2D peak with increased $2D_1/2D_2$ intensity ratio. This analysis was preceded by AFM (using a Keysight apparatus) measures which revealed, as expected, an increased blister density with the number of CVs. 2 CV samples were chosen as the best for the AFM-Raman combined measures. This samples present a higher density of large blisters compared to 1 CV ones, without resulting in a diffuse swelling of the HOPG basal plane and a complex "blister over blister" morphology, as observed on the 4 CV samples.

Sample washing with ultra pure H_2O was investigated. No significant variation of the overall spectrum was observed. It was therefore decided to wash the samples and leave them drying for one day before the combined measures, in order to remove the surface from precipitates and obtain cleaner blister morphology. The sample cleaning is clearly visible also at the optical microscope as shown in **Figure A.2**:

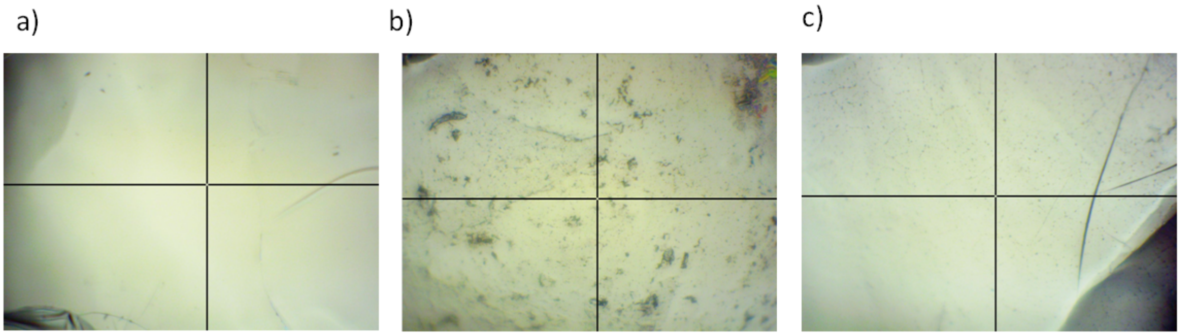

Figure A.2: Optical microscope (20x magnitude) images of a) pristine HOPG, b) 2 CV intercalated HOPG c) 2CV intercalated and washed HOPG. Washing removes the majority of precipitates.

A.3. Laser power and wavelength

Above a critical power the intercalated HOPG sample is altered by the laser beam in a permanent way. This is observed as a local decrease of the G_i peak intensity, as shown in **Figure A.3**. This degradation is not restored going back to lower powers. Preliminary tests investigated the maximum powers to avoid this effect for each excitation. The alteration seems dependent on the photon energy: for the blue laser the maximum power usable is way less than the red one, for which no degradation of the G_i peak is observed even at maximum power (7.9 mW). The maximum power usable and the used power for the preliminar analysis are reported in **Table A.1**[1].

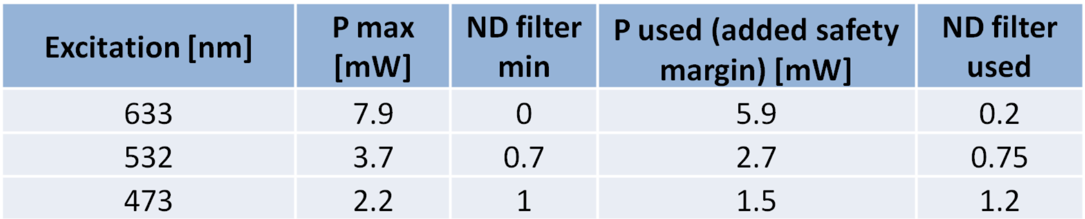

Excitation [nm]	P max [mW]	ND filter min	P used (added safety margin) [mW]	ND filter used
633	7.9	0	5.9	0.2
532	3.7	0.7	2.7	0.75
473	2.2	1	1.5	1.2

Table A.1: Maximum and used powers for the different excitations (SoLINano spectrometer).

---

[1] These values refer to the optical stage Raman preliminary measures, for the combined analysis at the AFM stage 532 nm laser with 2.5 mW power was employed (ND filter = 0.6, smaller because there are optical losses between optical and AFM stage).

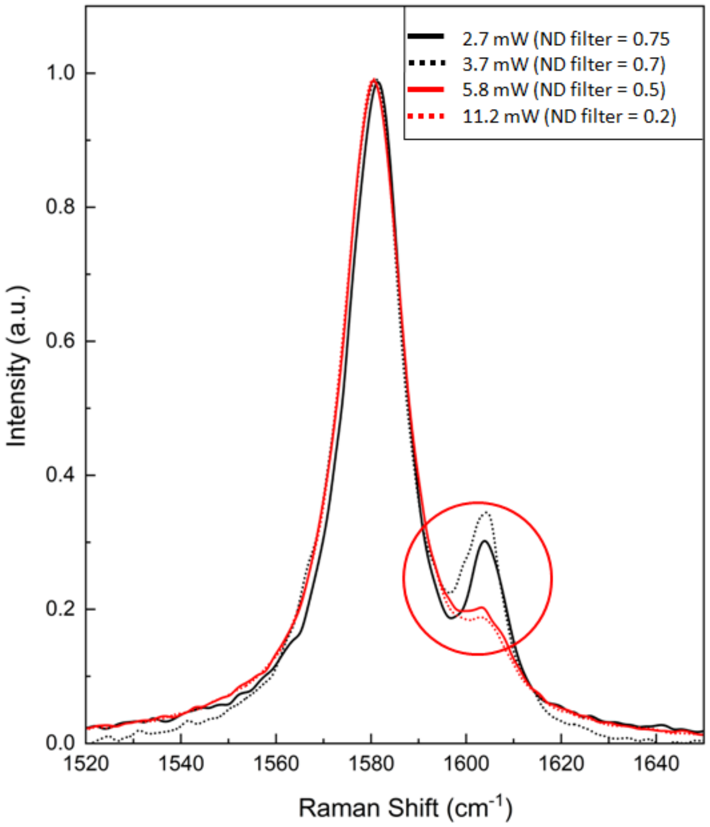

Figure A.3: Intercalated HOPG (2CVs) at different laser powers, for 532 nm laser.

Preliminary analysis were also conducted to choose the best laser excitation to use. The 633 nm laser was excluded because it is not possible to use this wavelength for combined measures in liquid, since the AFM laser is also red and this would result in interferences that perturb the AFM scan. All the statistical measures were acquired in air, but it will be useful to have comparable parameters for further studies. The blue 473 nm excitation offers an enhanced 2D peak intensity because of DR mechanisms. It can however operate at lower powers before altering the intercalated HOPG surface, thus resulting in a less intense and more noisy map at parity of acquisition time. Furthermore at 600/600 grating, 473 nm laser offers more spectral range but less spectral resolution compared to 532 nm. The green 532 nm excitation was therefore chosen as the fittest for the statistical analysis, combining better spectral resolution with the possibility of in-situ measurements.

B | Appendix: summary of all acquired spectra

In this appendix all the spectra (normalized and not normalized) of the analyzed blisters and HOPG basal plane are plotted. Raman maps of G peak intensity and position are also shown. The G peak enhancement and downshift is observed in all maps. Anomalous double G blister are highlited in violet as in previous analysis.

Blister 1

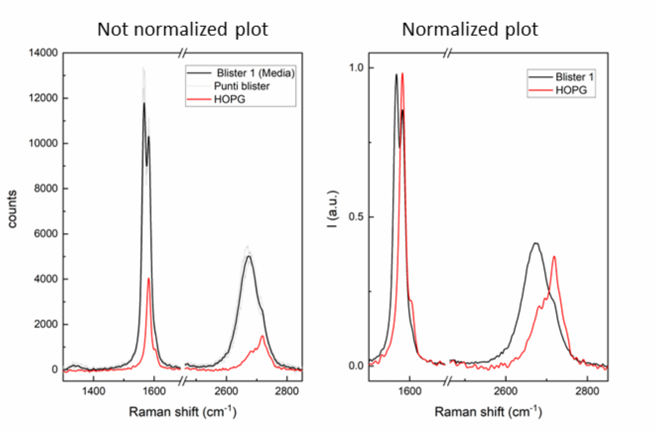

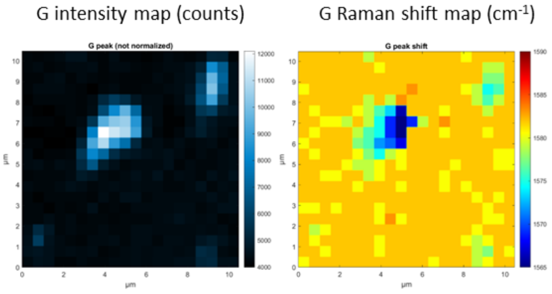

Blister 2

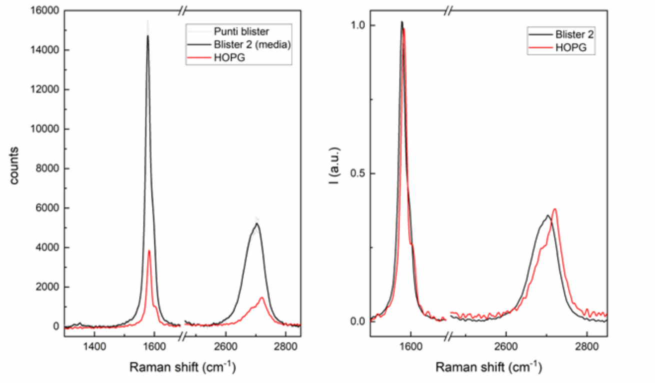

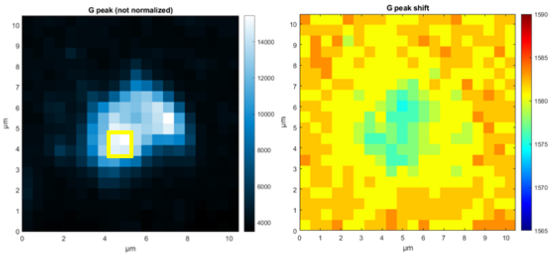

Blister 3

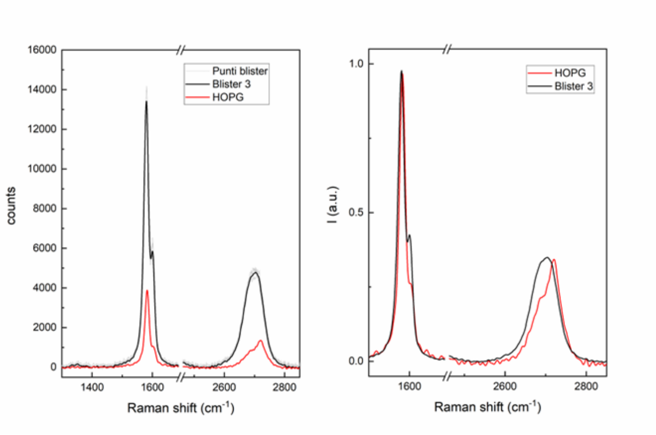

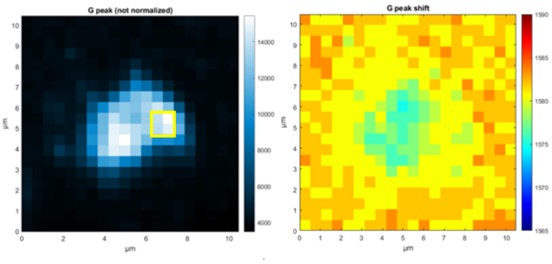

Blister 4

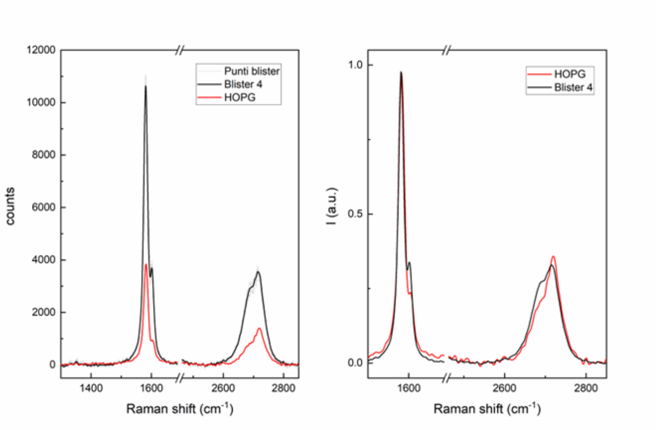

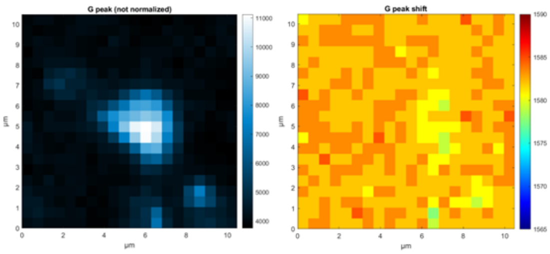

Blister 5

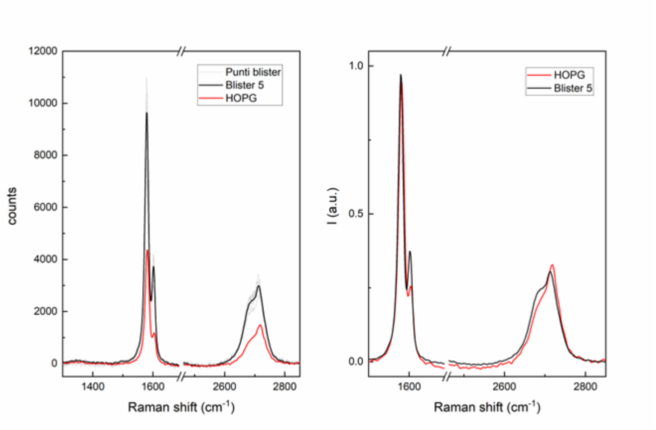

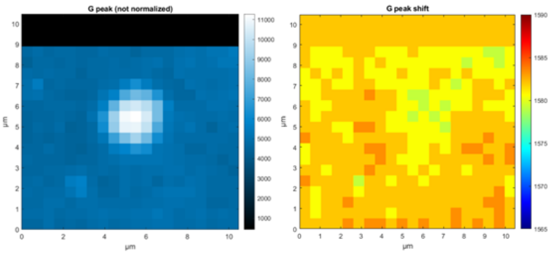

Blister 6

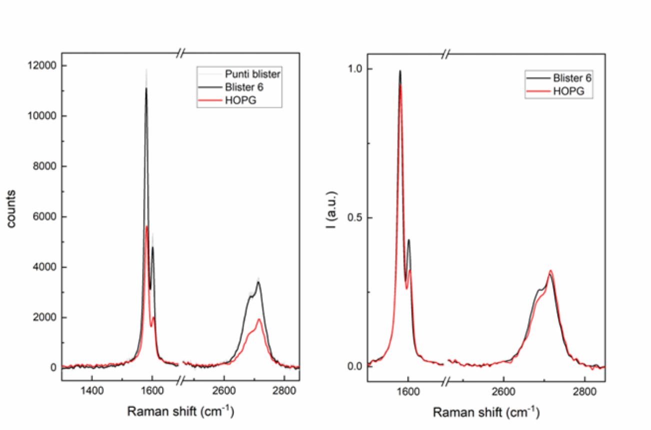

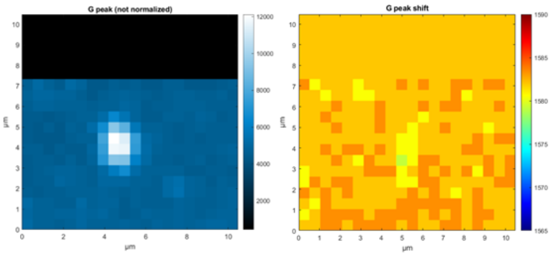

Blister 7

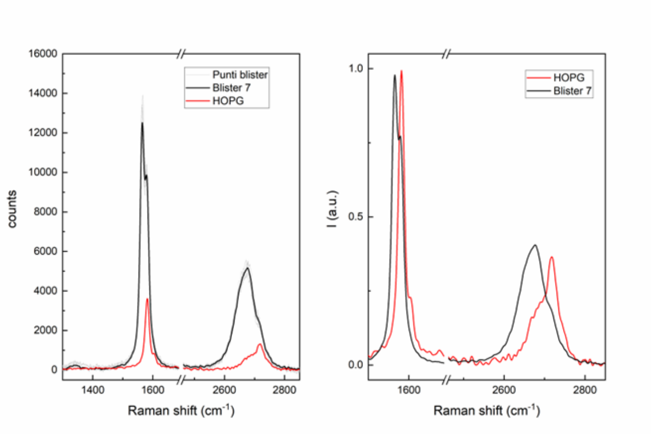

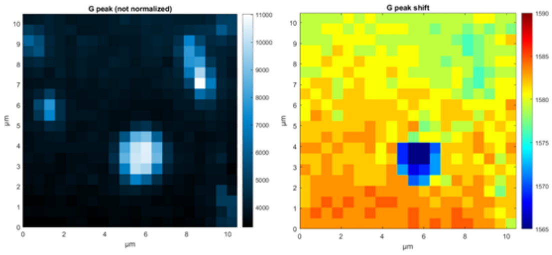

Blister 8

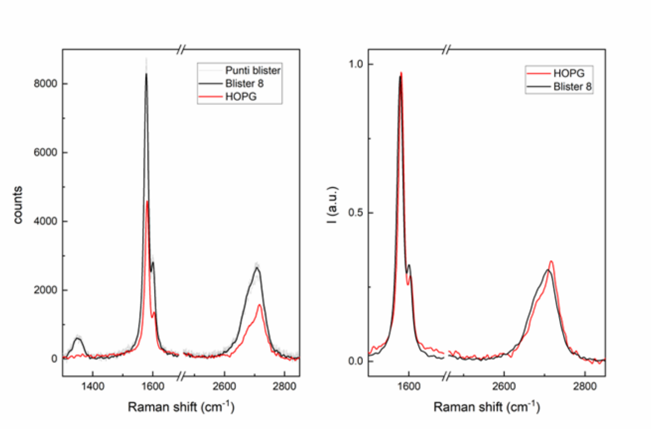

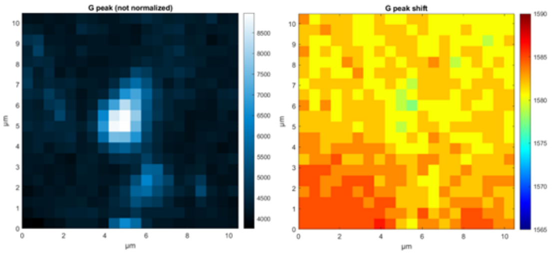

Blister 9

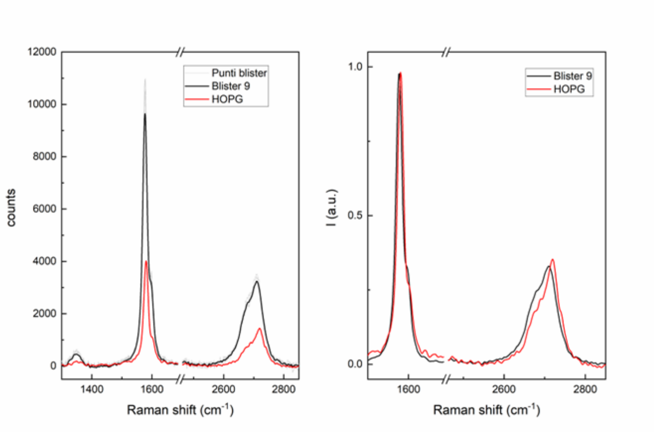

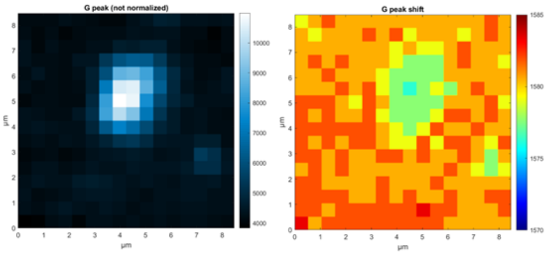

Blister 10

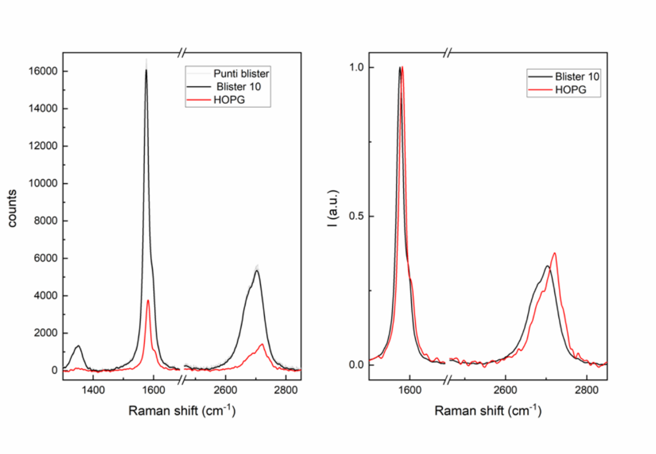

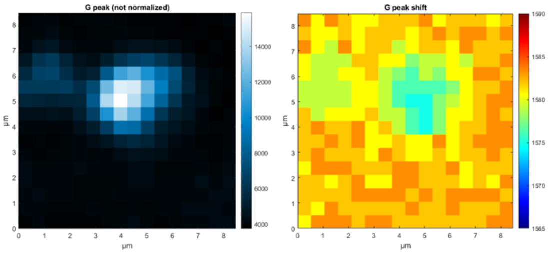

Blister 12

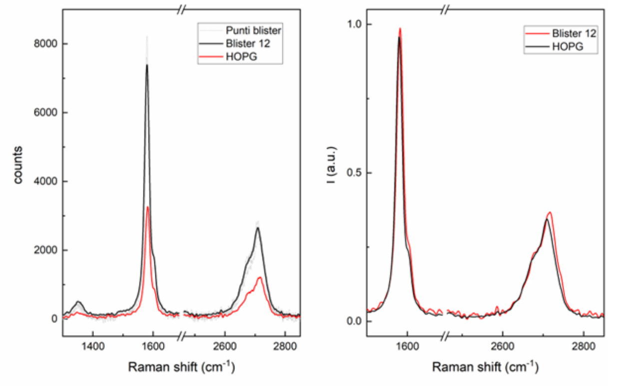

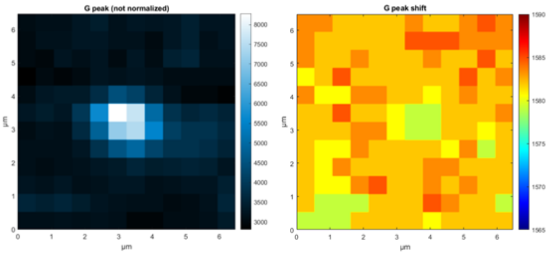

Blister 13

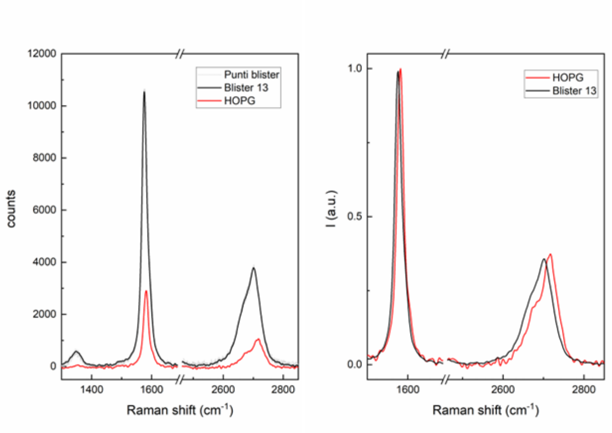

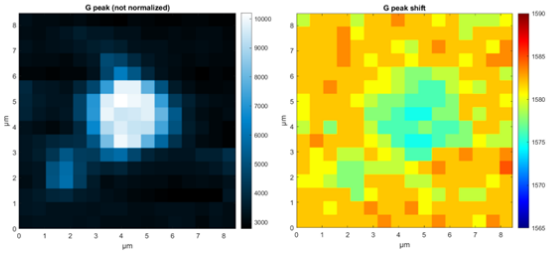

Blister 14

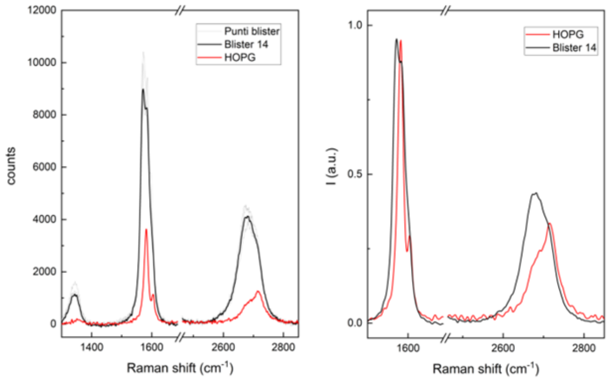

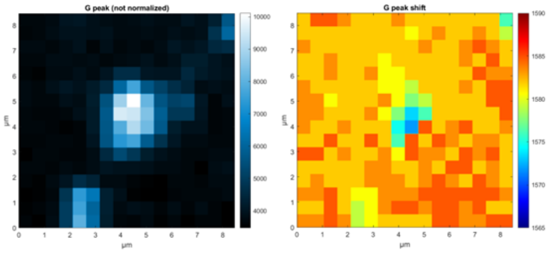

Blister 15

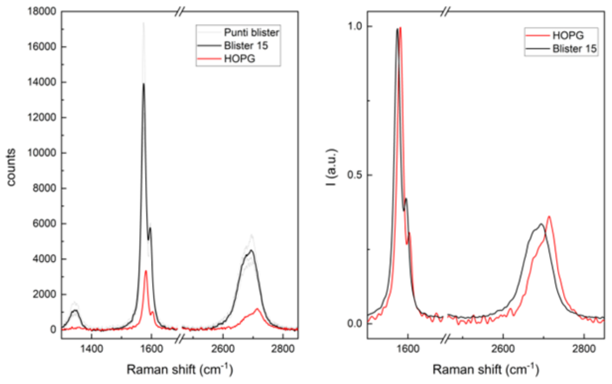

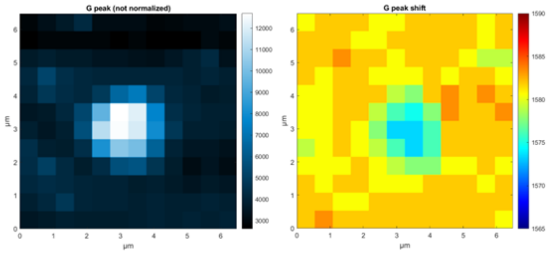

Blister 16

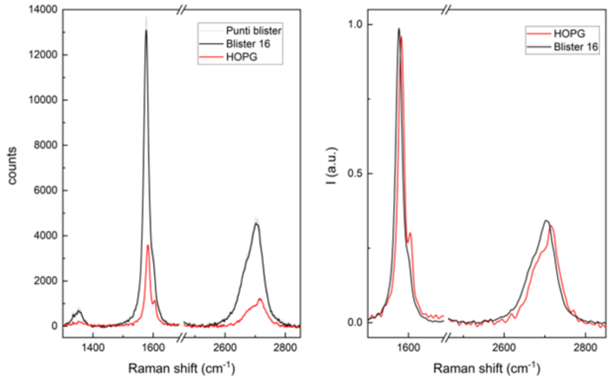

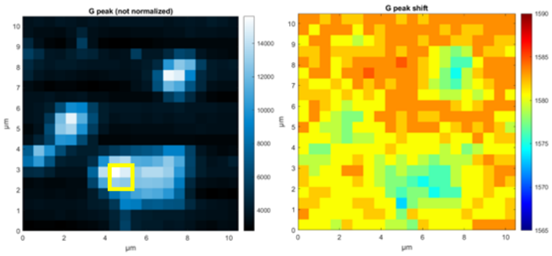

Blister 17

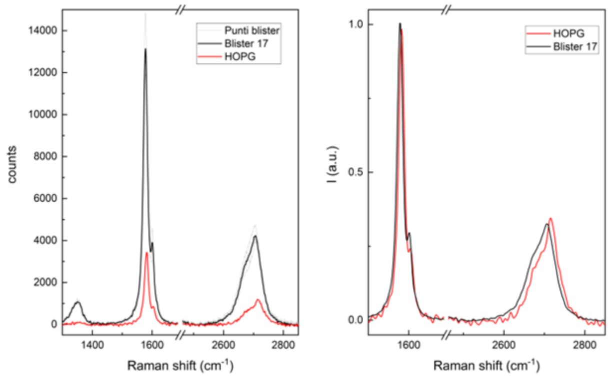

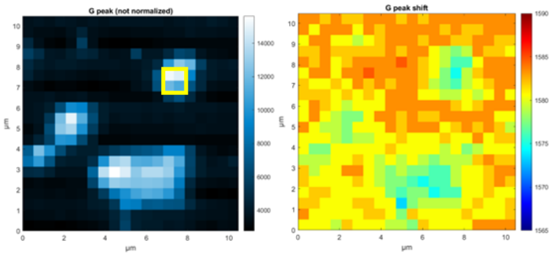

Blister 18

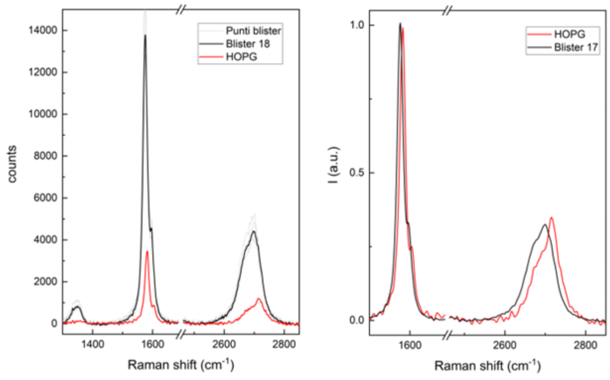

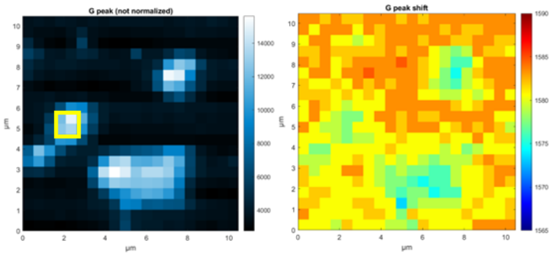

Blister 19

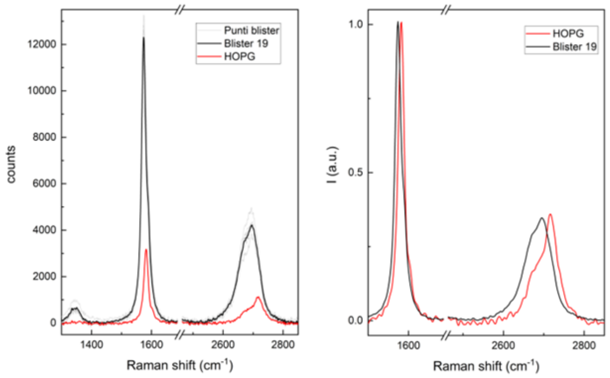

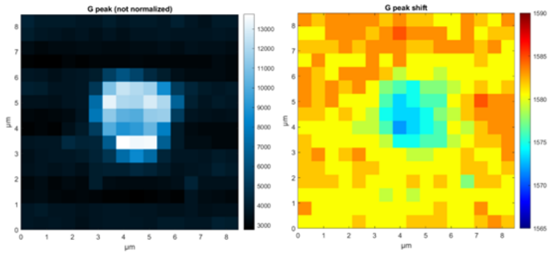

Blister 20

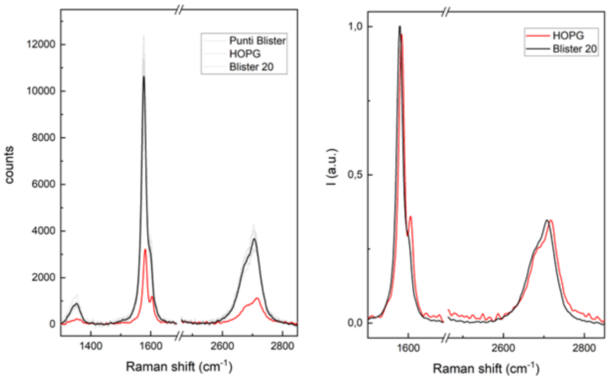

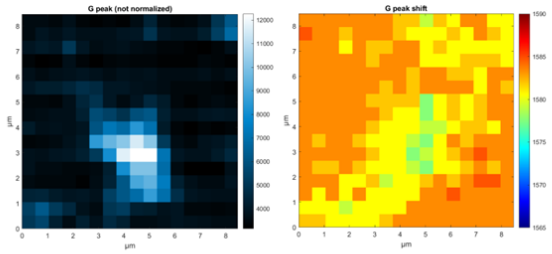

Blister 21

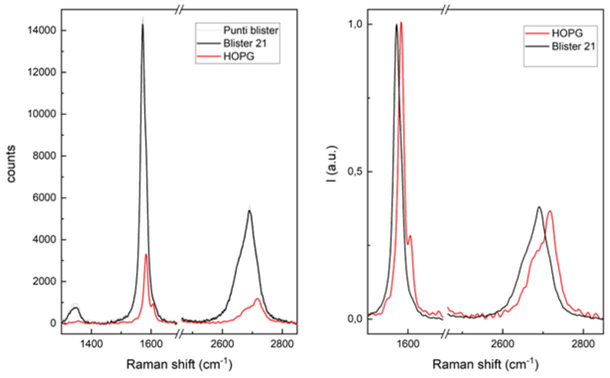

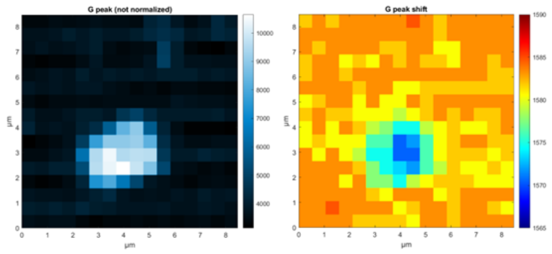

Blister 22

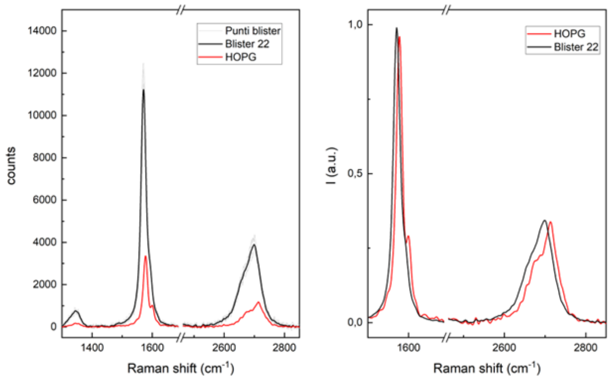

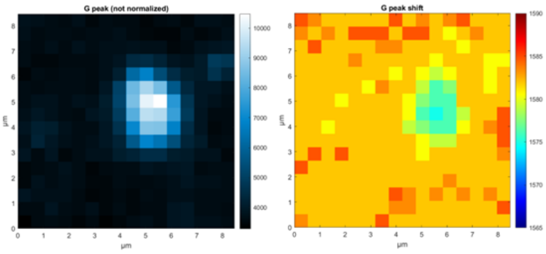

Blister 24

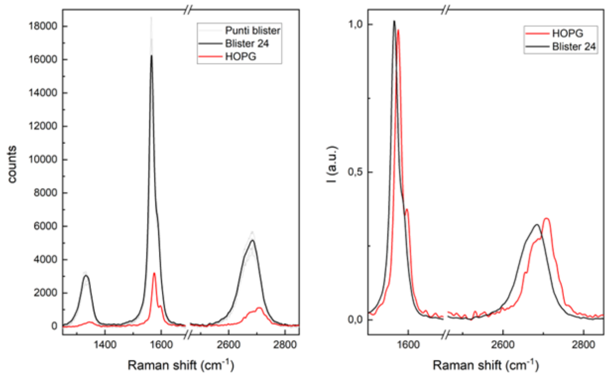

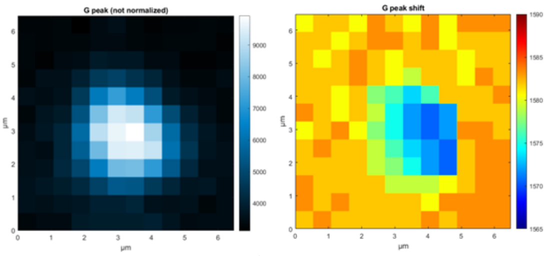

Blister 25

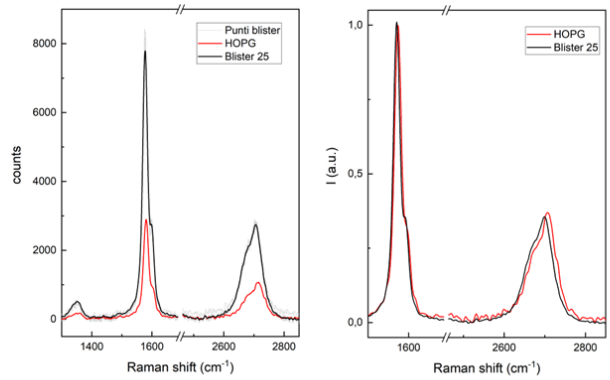

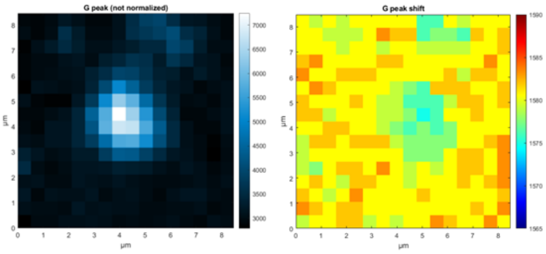

Ringraziamenti